UNIVERSITY OF CALIFORNIA
RIVERSIDE

Understanding Bursty Star Formation in Dwarf Galaxies, Its Effect on Galactic Dynamics, and Implications for Reionization

A Dissertation submitted in partial satisfaction
of the requirements for the degree of

Doctor of Philosophy

in

Physics

by

Najmeh Emami

September 2019

Dissertation Committee:

Dr. Brian Siana, Chairperson
Dr. Bahram Mobasher
Dr. Laura Sales

The Dissertation of Najmeh Emami is approved:

Committee Chairperson

University of California, Riverside

Acknowledgments

I am grateful to my advisor, Brian Siana without whose help and support, I would not have been here. He taught me how to become a better thinker, writer, and speaker and was an inspiration to me to succeed in my PhD degree.

I would like to thank my committee members Bahram Mobasher and Laura Sales and other faculties in Astronomy departments who taught me Astronomy and made the department a welcoming environment for the time I was there.

I would like to further thank individuals and friends who helped me obtain the technical skills necessary for my research and for all the inspirational discussions which helped shape me into the person I am now. In particular I am gratefully indebted to Joobin Gharibshah, Anahita Alavi, Amanda Pagul and Ali Ahmad Khostovan.

I would also like to thank my co-authors Daniel Weisz, Benjamin Johnson, Andreas Faisst, Kareem El-Badry, Xiangcheng Ma, David Cook, Daniel Stark, Johan Richard, and many others who made the research presented here possible.

I would like to thank my fellow group-mates, Anahita Alavi, William Freeman, Kaveh Vasei, Timothy Gburek and Christopher Snap Kolas for the constructive discussions we had during our group meetings and for the tireless teamwork during the observing nights and for all fun we had during the last five years.

Last but not the least, I would like to thank my family and friends who helped me become the person I am now. In particular I would like to thank my parents Shahla Aliyari and Nematollah Emami who have always been supportive and encouraging to me and are the reason to pursue my career. I am also grateful for having Mahdi and Narges Emami as my

brother and sister who are the best friends and emotional supporters that I could have ever imagined. I was also very fortunate to meet so many incredible friends during my PhD life in UCR who made it easier for me being away from my family and country and made me think of UCR as my second home.

This material is based upon work supported by the National Science Foundation under Grant No. 1617013. The work presented in chapter 2 of this dissertation is published in the Astrophysical Journal[1] and was Supported by program number 13905 provided by NASA through a grant from the Space Telescope Science Institute, which is operated by the Association of Universities for Research in Astronomy, Inc., under NASA contract NAS5-26555. This research has made use of the NASA/IPAC Extragalactic Database (NED), which is operated by the Jet Propulsion Laboratory, California Institute of Technology, under contract with the National Aeronautics and Space Administration. This research has made extensive use of LVL (Local Volume Legacy) survey which has made most of its dataset publicly available to the community. I would also like to recognize and acknowledge the very significant cultural role and reverence that the summit of Mauna kea has always had within the indigenous 18 Hawaiian community. We are most fortunate to have the opportunity to conduct observations from this mountain.

[1] https://iopscience.iop.org/article/10.3847/1538-4357/ab211a

To my parents Shahla and Nematollah for their continuous love and support.

ABSTRACT OF THE DISSERTATION

Understanding Bursty Star Formation in Dwarf Galaxies, Its Effect on Galactic Dynamics, and Implications for Reionization

by

Najmeh Emami

Doctor of Philosophy, Graduate Program in Physics
University of California, Riverside, September 2019
Dr. Brian Siana, Chairperson

Dwarf galaxies – galaxies with stellar masses below $10^9 M_\odot$ – are the most abundant galaxies in the universe. Due to their shallow gravitational potential well and small gas reservoirs, dwarfs are easily disrupted by supernovae feedback and can lose a fraction of their cold gas to the intergalactic medium in the form of outflows. Implementation of feedback into hydrodynamical simulations suggests that this phenomenon leads to a stochastic star formation history in these low-mass systems called *bursty star formation*. Burstiness can cause large variations of many physical quantities such as metallicity, morphology, radial velocity, dark matter density profile, etc. and can reconcile the discrepancies between the predictions from cold dark matter and observations in near-field cosmology. In order to characterize burstiness, we use two different star formation rate indicators that are sensitive to the recent and current star formation changes (Hα and UV_{1500} luminosities). We apply exponentially rising/falling burst models to determine the timescales and amplitudes of the bursts for each mass bin and compare the results to the simulations. We find that in lower mass galaxies, burstiness becomes stronger and shorter. Furthermore, we discuss the impor-

tance of dwarf galaxies to the reionization of the universe and describe our measurement of ξ_{ion} as one of the key components in determining the ionizing emissivity of dwarf galaxies. For that, we use a sample of lensed dwarf galaxies at a redshift of $1 < z < 3$, pushing the limits to higher redshifts and lower luminosities than others have studied before. We do not find any strong dependence between $\log(\xi_{ion})$ and M_{UV} or UV spectral slope (β) and report a value of $\log(\xi_{ion})$= 25.5-25.6 for $21 < M_{UV} < 18$. Lastly, we discuss the effect of burstiness on the dynamics and morphology of stars and gas inside dwarf galaxies. Our findings show that there is evidence of both size fluctuation and gas velocity variations being correlated with the UV_{1500}-inferred star formation indicators especially at masses below $10^{8.5} M_{\odot}$.

Contents

List of Figures

List of Tables

Chapter 1

Introduction

Dwarf galaxies, typically defined as having stellar masses less than $10^9 M_\odot$, are the most abundant galaxies in the universe. Unlike their massive counterparts that have established positive correlations between their physical quantities (such as gas vs. star formation rate (SFR) (Kennicutt-Schmitt relation), gas velocity dispersion vs. stellar mass (Tully-Fisher relation), stellar mass vs. metallicity (MZR)), dwarfs of similar masses exhibit a large scatter in the low-mass range of these relations. This suggests that perhaps there is a stochasticity in the nature of these dwarfs that can be seen as broad variations in their physical properties (metallicity, SFR, morphology, gas surface density, etc.).

Due to their shallow gravitational potential well and small gas reservoirs, dwarf galaxies are easily disrupted by supernovae (SN) feedback and can lose a fraction of their cold gas and metals to the intergalactic medium (IGM) in the form of outflows, leading to a decline in their star formation rates (SFR). Once the outflows stop, the gravitational potential starts to reaccrete gas to the center and resumes the star formation. Implementa-

tion of feedback into hydrodynamical simulations suggests that this phenomenon leads to a stochastic star formation history in low-mass systems called *burstiness*

There have been ongoing attempts in characterizing the burstiness in dwarf galaxies by employing different SFR indicators that are sensitive to different timescales such as Hα and far-UV luminosities. This helps constrain the burst parameters such as the amplitude, period and duration of the bursts. More importantly, this constrains something more profound about the timescale of the rising and declining SFR, i.e. the timescale within which the SNe feedback and gravity take control of the star formation processes in galaxies.

Burstiness can have impacts on the gas and stellar kinematics as well as dark matter structure of galaxies. For instance, feedback-driven outflows can transfer energy to the dark matter and cause the dark matter density profile to change from cusp to core. Burstiness can also explain the variety seen in the morphology of dwarf galaxies from rotationally-supported disks to dispersion-supported irregulars. Baryonic matter can also be impacted by burstiness such that outflows can displace stars from the center to the outer regions and cause a galaxy *size fluctuation* during episodes of star formation. Furthermore, outflowing winds can kick gas particles out of the center resulting in a Doppler broadening in the shape of the gas emission line profiles. Such strong outflow-driven winds can also locally facilitate the escape of metals and ionizing photons from the galaxy by creating hot *chimneys* and venting energy out of it. This makes dwarfs to release much of their ionizing photons to the IGM and be considered as an important candidate for the reionization of the universe at high redshifts (Paardekooper et al., 2013; Wise et al., 2014; Erb, 2015; Anderson et al., 2017; Henry et al., 2015; Karman et al., 2017).

Other than having high escape fractions of ionizing photons, there is other supporting evidence that makes dwarf galaxies likely responsible for the reionization: due to their large number density, they are thought to contribute largely to the total ionizing UV light budget necessary to keep the universe ionized. This has been inferred from the steep faint end slope of 1500 $\mathring{A}$ UV luminosity function observed in high redshift galaxies (Reddy and Steidel, 2009; Bouwens et al., 2012; Alavi et al., 2014; Atek et al., 2015; Livermore et al., 2017).

Despite their importance, due to their low brightness, dwarf galaxies have been inaccessible to the high redshift UV searches with our current instruments. Yet the detection of dwarf galaxies, especially those with low-surface brightness, remains as a long-standing challenge to modern Astronomy.

1.1 Summary of Thesis

In this thesis we study *burstiness* in dwarf galaxies. Throughout this research we have made use of both local and high-redshift lensed samples of dwarf galaxies in order to quantify the burstiness phenomenon and investigate its impact on the dynamics of galaxies as well as its impact on the reionization of the universe. Below we summarize the structure of the manuscript.

Chapter 2: We investigate burstiness in a sample of local dwarf galaxies using the distribution of $\log(L_{H\alpha}/L_{UV})$ as an indicator of the recent star formation activity relative to the past. We also include additional indicator to the existing $L_{H\alpha}/L_{UV}$ which is the excess in the $L_{H\alpha}$ relative to the average ($\Delta\log(L_{H\alpha})$). We examine the 2-dimensional distribution

of these two indicators to constrain the SFHs. We use exponentially rising/falling bursts to determine timescales (e-folding time, τ) and amplitudes (A) of the bursts. By comparing to the observed sample, we find the best-fit τ and A for each mass bin. We also compare to the FIRE-2 hydrodynamical simulations and discuss the consistencies and differences between simulation and observation.

Chapter 3: We measure the ionizing photon production efficiency (ξ_{ion}) as one of the key components in determining the ionizing emissivity of dwarf galaxies and ultimately their role in the cosmic reionization. We make use of a sample of faint low-mass galaxies at an intermediate redshift of $1 < z < 3$ that are lensed by foreground lensing clusters. We are first to observe such faint low-mass galaxies at such high redshifts. We present a new method of stacking fluxes for the ξ_{ion} measurements. We argue that this method properly deals with the large scatter seen in the distribution of ξ_{ion} due to the stochastic nature of SFHs in dwarfs. We also investigate the relationships between ξ_{ion} and other physical properties of galaxies and compare our findings to other works at other redshifts and stellar masses.

Chapter 4: We investigate the effect of burstiness on the dynamics of stars and gas inside galaxies. In particular we determine how outflows driven by stellar feedback drive stars from the center to the outer regions and cause a galaxy size fluctuation throughout episodes of star formation. For that we measure the R-band effective radius for the same local sample as we used in Chapter 2 and look at its relationship with the star formation indicators ($L_{H\alpha}$ and L_{UV}). In addition, we determine the effect of outflows on the gas radial velocities by studying the shape of the HI 21 cm velocity profile and investigate its

connection with $L_{H\alpha}$ and L_{UV}. These two tests will allow us to better understand the effect of burstiness on the morphology and dynamics of baryonic matter in dwarf galaxies and constrain the mass range at which these two effects become most important.

Chapter 2

A Closer look at Bursty Star Formation with $L_{H\alpha}$ and L_{UV} Distributions

2.1 Abstract

We investigate the bursty star formation histories (SFHs) of dwarf galaxies using the distribution of $\log(L_{H\alpha}/L_{UV})$ of 185 local galaxies. We expand on the work of Weisz et al. (2012b) to consider a wider range of SFHs and stellar metallicities, and show that there are large degeneracies in a periodic, top-hat burst model. We argue that all galaxies of a given mass have similar SFHs and we can therefore include the $L_{H\alpha}$ distributions (subtracting the median trend with stellar mass, referred to as $\Delta\log(L_{H\alpha})$) in our analyses. $\Delta\log(L_{H\alpha})$ traces the amplitude of the bursts, and $\log(L_{H\alpha}/L_{UV})$ is a function of

timescale, amplitude, and shape of the bursts. We examine the 2-dimensional distribution of these two indicators to constrain the SFHs. We use exponentially rising/falling bursts to determine timescales (e-folding time, τ). We find that galaxies below $10^{7.5}$ $M_\odot$ undergo large (maximum amplitudes of ~ 100) and rapid ($\tau < 30$ Myr) bursts, while galaxies above $10^{8.5}$ $M_\odot$ experience smaller (maximum amplitudes ~ 10), slower (τ300 Myr) bursts. We compare to the FIRE-2 hydrodynamical simulations and find that the burst amplitudes agree with observations, but they are too rapid in intermediate-mass galaxies ($M_* > 10^8$ $M_\odot$). Finally, we confirm that stochastic sampling of the stellar mass function can not reproduce the observed distributions unless the standard assumptions of cluster and stellar mass functions are changed. With the next generation of telescopes, measurements of L_{UV} and $L_{H\alpha}$ will become available for dwarf galaxies at high-redshift, enabling similar analyses of galaxies in the early universe.

2.2 Introduction

An active area of research in galaxy evolution is understanding "feedback" – energy and/or momentum deposition into the interstellar medium – from stars and accreting black holes. It is generally believed that star formation is suppressed in high mass galaxies by feedback from the central, supermassive black holes and in dwarf galaxies by feedback from massive stars (photoionization heating, stellar winds, radiation pressure, and supernovae) (Hopkins et al., 2014; Kereš et al., 2009; Springel et al., 2005; Governato et al., 2010; Somerville and Primack, 1999).

However, there are still significant uncertainties in how the various forms of feed-

back couple with the gas and the efficiency with which it heats or expels gas. When different sub-grid prescriptions for stellar feedback are implemented in hydrodynamical simulations, it can result in markedly different predictions of the characteristics of galaxies. One generic feature of hydrodynamical simulations of dwarf galaxies that include strong stellar feedback, is large variations in the star formation rates (SFRs), often referred to as "bursty" star formation. Simulations with different feedback prescriptions produce bursts of star formation with very different characteristics (e.g. amplitude and duration). Because it is in principle possible to observe large variations in SFR, observers can test these feedback prescriptions to better understand the physical mechanisms that regulate star formation in dwarf galaxies.

The primary method by which one can measure the burstiness is to use indicators (observables) of star formation that trace different time scales. The two most common indicators are the luminosity of the (non-scattering) Hydrogen recombination lines (such as Hα and Hβ), and the far-ultraviolet (far-UV) continuum (1300 Å $< \lambda <$ 2000 Å) luminosity density (L_{UV}). Hereafter we refer to the logarithm of the ratio of these two observables, $\log(L_{H\alpha}/L_{UV})$. $L_{H\alpha}$ is a byproduct of the ionizing radiation from short-lived O-stars. Therefore, during an episode of constant star formation, $L_{H\alpha}$ equilibrates rapidly, as the rate of O-star supernovae equals the rate of O-star formation. L_{UV}, on the other hand, is produced by O-stars as well as longer-lived B and A stars. Therefore, L_{UV} takes much longer to reach equilibrium after an episode of constant star formation. Using the stellar population synthesis models of Bruzual and Charlot (2003) for constant star formation, we find equilibrium time scales (reaching 90% of the equilibrium value, Kennicutt and Evans,

2012) of 5 and 100 Myr for $L_{H\alpha}$ and L_{UV}, respectively. Because of this, both $L_{H\alpha}$ and L_{UV} accurately trace the SFR of any galaxy whose SFR changes on time scales much larger than 100 Myr. Thus, the ratio, $\log(L_{H\alpha}/L_{UV})$, remains approximately constant. However, if the SFR changes on shorter time scales than 100 Myr, L_{UV} will no longer follow the SFR and the ratio, $\log(L_{H\alpha}/L_{UV})$, will vary. Therefore, the distribution of the $\log(L_{H\alpha}/L_{UV})$ can inform whether or not the SFR of galaxies changes on time scales less than 100 Myr.

We note that these observables ($L_{H\alpha}$, L_{UV}) are often used to determine physical properties of galaxies like SFR and the ionizing photon production efficiency (ξ_{ion}) (Bouwens et al., 2015a; Duncan and Conselice, 2015b; Robertson et al., 2013) under the assumption that star formation varies slowly with time. Therefore, understanding bursty star formation is critical for interpreting these observables (Domínguez et al., 2015).

There have been several analyses of the distributions of $L_{H\alpha}/L_{UV}$ attempting to extract information about the typical amplitudes, durations, and periods of the bursts (Glazebrook et al., 1999; Iglesias-Páramo et al., 2004; Lee et al., 2011; Weisz et al., 2012a; Kauffmann, 2014; Domínguez et al., 2015). Several factors other than SFH can affect the $L_{H\alpha}/L_{UV}$, as discussed by Iglesias-Páramo et al. (2004); Lee et al. (2009); Meurer et al. (2009); Boselli et al. (2009), and Guo et al. (2016a). Here, we list all of these factors other than the star formation history (which is the subject of this paper) and briefly explain how they affect $L_{H\alpha}/L_{UV}$.

- Dust extinction: Because dust extinction is often a strong function of wavelength, and the nebular and stellar UV continuum emission can arise from stars with different spatial distributions relative to dust, the effect of dust on the observed $L_{H\alpha}/L_{UV}$ can

be considerable (Kewley et al., 2002; Lee et al., 2009).

- Escape of ionizing photons: If ionizing photons are escaping from the galaxy (Steidel et al., 2001; Shapley et al., 2006; Siana et al., 2007), the photoionization rate (and therefore, $L_{H\alpha}$) will be lower than expected under the assumption that all ionizing photons are absorbed in HII regions.

- Initial stellar mass function (ISMF): The $L_{H\alpha}/L_{UV}$ is influenced by the relative number of stars at each mass, so variations in the ISMF will affect the ratio. This can include "effective ISMFs", where the star-forming clouds are not sufficiently massive to fully sample the high-mass end of the ISMF (Hoversten and Glazebrook, 2008; Pflamm-Altenburg et al., 2007; Pflamm-Altenburg et al., 2009). The initial cluster mass function (ICMF) can also affect these "effective ISMFs" because it determines the relative number of clusters that do and do not fully sample the high mass end of the ISMF.

- Stellar metallicity: Stars with lower metal abundances will be hotter at the same mass, resulting in a higher $L_{H\alpha}/L_{UV}$ (Bicker and Fritze-v. Alvensleben, 2005; Boselli et al., 2009).

- Stellar models: Inclusion of binaries (Eldridge, 2012) and rotating stars (Choi et al., 2017) in the stellar evolution modelling will increase $L_{H\alpha}/L_{UV}$.

There are several papers discussing these effects on the $L_{H\alpha}/L_{UV}$ distribution, but many have concluded that the most important effects are bursty star formation and (or) variations in the IMF (Meurer et al., 2009; Guo et al., 2016a; Mehta et al., 2017).

The main focus of this paper is to use observable distributions to better understand bursty star formation. Specifically, we aim to: (1) more fully explore the parameter space of bursty star formation models. (2) Break degeneracies and minimize uncertainties in these models. (3) Determine typical timescales for the rise/fall of star formation as a function of galaxy stellar mass. (4) Better understand whether burstiness or IMF variations explain the observed $L_{H\alpha}/L_{UV}$ distributions.

First we describe the observational data which will be used throughout this paper in section 3.3. In Section 2.4, we review previous efforts to determine the burstiness parameters (amplitude, period, duration) using the $L_{H\alpha}/L_{UV}$ distribution. We also introduce our improved method to more completely explore the parameter space and compare with previous results. In Section 2.5.1, we propose combining the $L_{H\alpha}$ distribution with the $L_{H\alpha}/L_{UV}$ distribution to better constrain bursty star formation models. In Section 2.5.2, we introduce a new exponential burst model to better constrain the timescales for the rise and fall of SFRs in dwarf galaxies. In Section 2.6, we compare to predictions from hydrodynamical simulations and discuss the physical implications. We also examine the effect of stochastic IMF sampling on our analysis and discuss the results in this section as well as the effects of escape fraction and dust attenuation on the observed distribution.

2.3 Observational Data

In this work, we use the same far-ultraviolet (FUV) and $H\alpha$ photometry as W12 from the 11 Mpc $H\alpha$ and UV Galaxy Survey (11HUGS, Kennicutt et al., 2008; Lee et al., 2009). The primary sample is complete in including all nearby galaxies within 11 Mpc and

consists of spirals and irregulars that avoid the Galactic plane($|b| > 20°$) and are brighter than $B = 15$ mag. Stellar masses were determined using optical photometry from the Sloan Digital Sky Survey and *Spitzer* mid-IR (IRAC) photometry from the Local Volume Legacy (LVL) Survey. Thus the W12 sample is a subsample of 11Hugs galaxies for which their optical and IR measurements are available. The data are corrected for both Galactic foreground dust extinction and extinction within the target galaxy. See W12 and Lee et al. (2009) for further details and sample completeness. We decided to remove five galaxies with either $\log(L_{H\alpha}/L_{UV}) < -3.4$ or $\log(L_{H\alpha}/L_{UV}) > -1.8$ from the sample. Two of the outliers (UGCA281, MRK475) are Wolf-Rayet galaxies. The other three outliers have extremely high or low $\log(L_{H\alpha}/L_{UV})$ such that the stellar synthesis models are not able to reproduce them (UGCA438, KDG61, UGC7408).

2.4 Review of the Methods

Below, we discuss the methods used in previous studies and argue the strengths and shortcomings of those methods.

Iglesias-Páramo et al. (2004) and Boselli et al. (2009) considered instantaneous bursts of SF superimposed on a baseline with a few different time intervals between bursts. Meurer et al. (2009) used a SF model of Gaussian bursts added (or "gasps" subtracted) from a constant SFR, in which the FWHM of the Gaussians represents the duration, and also affects timescale for fractional changes in SFR. All three studies assumed discrete model parameters and did not fully and systematically explore the parameter space. It is noteworthy that Boselli et al. (2009) was the first to introduce different model parameters

for galaxies of different stellar masses, pointing out that low mass galaxies show a larger spread in the $\log(L_{H\alpha}/L_{UV})$ distribution. They conclude that this larger spread in the $\log(L_{H\alpha}/L_{UV})$ distribution is due to sporadic bursts of SF (with periods of 10 Myr) whereas the small spread in the $\log(L_{H\alpha}/L_{UV})$ distribution of massive galaxies suggests a roughly constant SFR.

Weisz et al. (2012a) (hereafter W12) made a notable step forward and divided their observed sample into five stellar mass bins from 10^6 to $10^{11} M_{\odot}$ and assumed that all galaxies of similar stellar masses have star formation histories with the same parameters and could be considered random samples in time of each SFH. They defined their SF models as top-hat, periodic bursts superimposed on a constant baseline. They then determined the $\log(L_{H\alpha}/L_{UV})$ distribution from models with different burst periods (P, the time interval between two consecutive bursts), durations (D, the time length when the star formation is in burst), and amplitudes (A, the SFR at burst relative to the baseline SFR) and used a Kolmogorov-Smirnov test to identify the parameters that best reproduce the observed $\log(L_{H\alpha}/L_{UV})$ distribution in each mass bin. The other improvement in W12 was the finer sampling of parameter space. The main conclusion of W12 is that galaxies with the lowest stellar masses have higher amplitude bursts (A $\sim 30\times$ the baseline rate), relatively long durations (D $\sim 30 - 40$ Myr), and long periods (P = 250 Myr). The highest mass bins are characterized by almost constant SFRs with an occasional modest burst favoring SF models with short duration (D ~ 6 Myr) and modest amplitudes (A ~ 10).

In the Appendix, we describe an analysis similar to that of W12, but with three significant improvements to better determine the best parameters of bursty SF. First, we

use appropriate (lower) stellar metallicities for the lower mass galaxies, as W12 used solar metallicities for all galaxies. This should change the predicted $\log(L_{H\alpha}/L_{UV})$ distributions as stars of the same mass at lower metallicity will be hotter and have a larger $\log(L_{H\alpha}/L_{UV})$ ratio. Second, we expand the parameter space, as some of the best-fit parameters in W12 were at the edge of the explored parameter space. Finally, we adopt a probabilistic approach to determine the best SF history parameters. This allows us to fully explore the parameter space, determine the relative merit (the likelihood) of each set of parameters, and search for any significant degeneracies between the parameters.

The results of our method are presented in Figure 2.1, which shows the marginalized likelihood of the duration, period and amplitude for the six stellar mass ranges defined in Table 2.2. On the right, the observed $\log(L_{H\alpha}/L_{UV})$ distributions for each mass bin are plotted as unfilled histograms along with the distribution of the best-fit models as filled histograms.

Galaxies with $M \geq 10^8 M_\odot$ have best-fit amplitudes < 3, signifying relatively stable star formation histories. However, such low amplitudes are very sensitive to the assumed errors in the observed luminosities and dust extinction corrections. On the other hand, all of the stellar mass bins at $M < 10^8 M_\odot$ have best-fit amplitudes > 15, suggesting dramatic bursts of star formation are necessary to explain the large spread of $\log(L_{H\alpha}/L_{UV})$ seen in these galaxies.

Our new analysis demonstrates that W12 did not probe the parameter space with the highest likelihood, as the posteriors peak at period of 500-900 Myr, Figure 2.1 second column (where W12 analyzed P$<$ 250 Myr). This is important for the duration parameter

as well, as it is highly correlated with the period (see below). Thus, the new duration estimates are considerably larger (D$\sim 40-250$ Myr) compared to D$\sim$ 20 Myr in W12. The amplitude estimates are uncertain, but broadly agree with the values in W12.

To better understand the degeneracies between the model parameters, we plot the 2D contours of the three lowest mass bins in Figure 2.2. In the Duration-Period contour plots, there is a linear degeneracy between period and duration, such that increasing the duration of the burst requires a similar increase in the period.

These degeneracies result in large uncertainties in the marginalized posteriors for both duration and period. Specifically, the burst durations of the low mass galaxies can be 50 or 250 Myr (or larger). Furthermore, we know that this periodic top-hat model is not accurate in that the star formation does not instantly change and is not truly periodic. Therefore, it is difficult to know whether or not these best-fit parameters reflect the true values of typical duration and period in these galaxies.

2.5 A New Approach to Characterizing Bursty Star Formation

So far we reviewed the previous studies and more carefully explored the top-hat periodic SF model of W12 to determine parameters of SFHs based only on the $\log(L_{H\alpha}/L_{UV})$ distribution.

However, two concerns ultimately arise from our new analysis. First, our new probabilistic approach allows us to see that significant degeneracies exist between the model

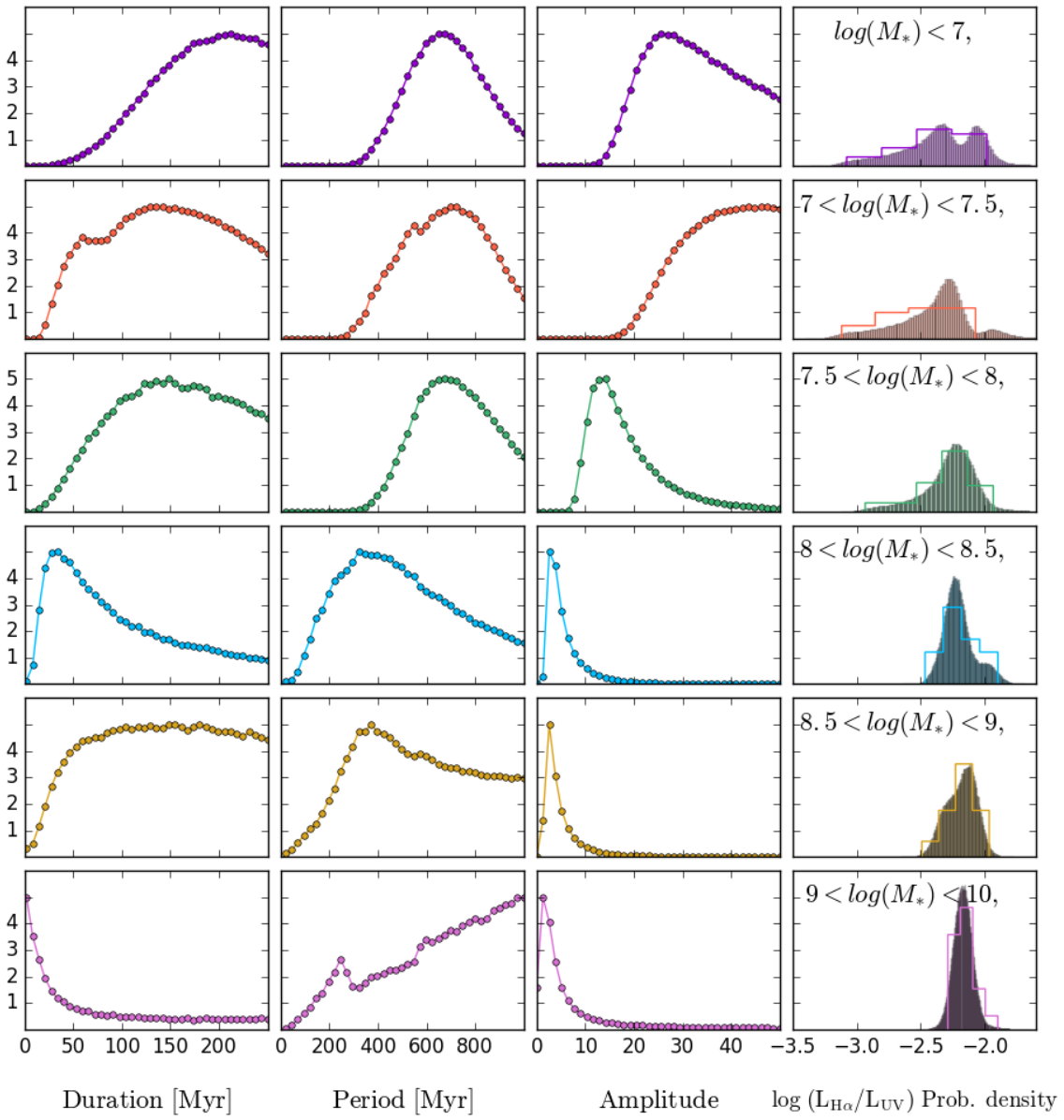

Figure 2.1: Likelihood function of duration, period and amplitude (relative to the baseline), as well as the $\log(L_{H\alpha}/L_{UV})$ distribution of the best fit models to the observed $\log(L_{H\alpha}/L_{UV})$ distribution for each mass bin, assuming metallicities from Andrews and Martini (2013). The open histograms show the observed sample and the filled histograms show the distribution of the best-fit model.

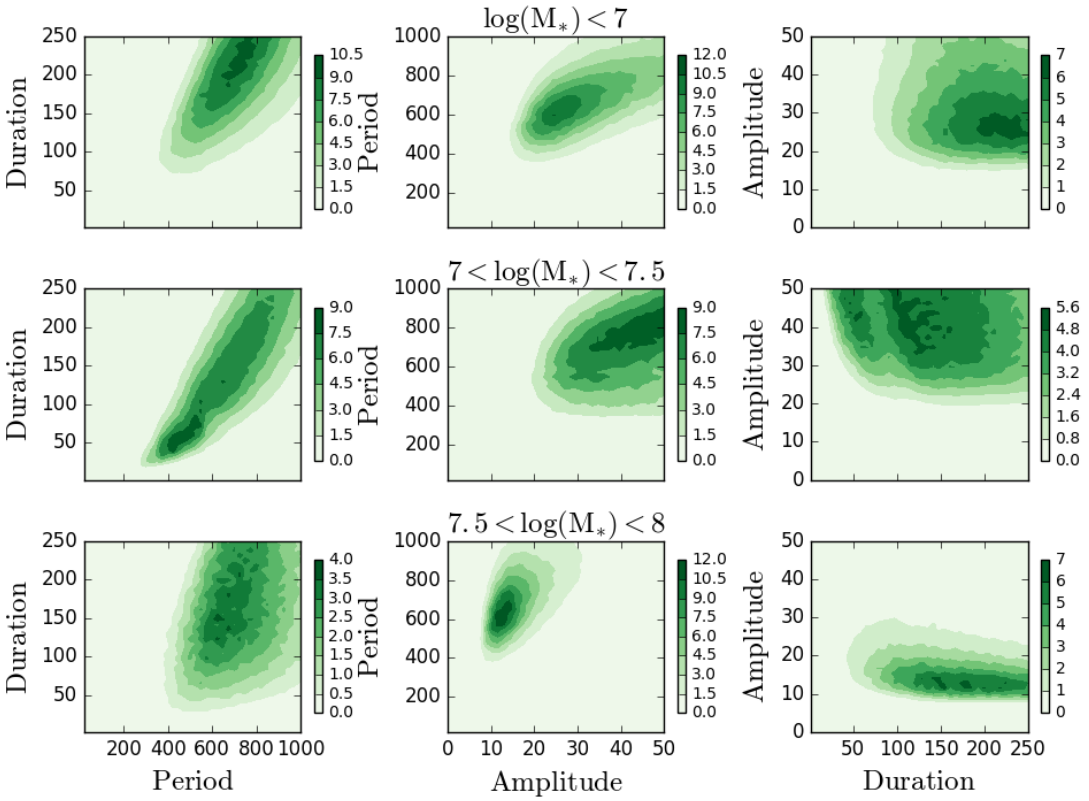

Figure 2.2: 2D contour plots of (D,P), (P,A) and (A, D). Each row corresponds to a different mass range of $M \leq 10^7\ M_\odot$, $10^7 < M \leq 10^7.5\ M_\odot$ and $10^7.5 < M \leq 10^8\ M_\odot$ from top to bottom. The probability densities are denoted as colorbars on the right of each panel. The strong degeneracy in duration and period can be seen for all mass ranges shown here.

parameters (see Figure 2.2). This is perhaps not surprising, as there are three parameters fit to a single $\log(L_{H\alpha}/L_{UV})$ distribution. Ultimately, it is necessary to use additional observables to fit complicated star formation histories.

Second, we know that the periodic, top-hat burst model is unphysical, as it requires instantaneous changes in SFR. Indeed, the best-fit model predicts *other* observable distributions that do not look like those observed. For example, the model predicts a bimodal $\Delta\log(L_{H\alpha})$ distribution at each mass, rather than the observed distribution, where galaxies are more evenly distributed in $\Delta\log(L_{H\alpha})$, suggesting that the typical galaxy spends a significant fraction of its lifetime near the average SFR, rather than in low and high states.

In this section, we seek to add additional observables to constrain the star formation histories, and we choose a somewhat simpler parametrization in order to focus on the timescales of the transitions from burst to quiescence and back.

2.5.1 The $L_{H\alpha}$ Distribution

$L_{H\alpha}$ is strongly correlated with stellar mass, M_*, with the scatter around the mean increasing at lower stellar mass (Figure 2.3). Thus, this distribution contains additional information about the SFH and we should be incorporating the $L_{H\alpha}$ distribution into our analyses of the SFH. Of course, the average of the distribution depends strongly on the stellar mass of the galaxy, and does not give any information about the relative changes in the SFR. We therefore choose to subtract the trend of $\log(L_{H\alpha})$, defining this as $\Delta\log(L_{H\alpha})$, plotted in Figure 2.3. The value of $\Delta\log(L_{H\alpha})$ tells us a galaxy's (nearly instantaneous) star formation rate, relative to the average, and the width of the distribution

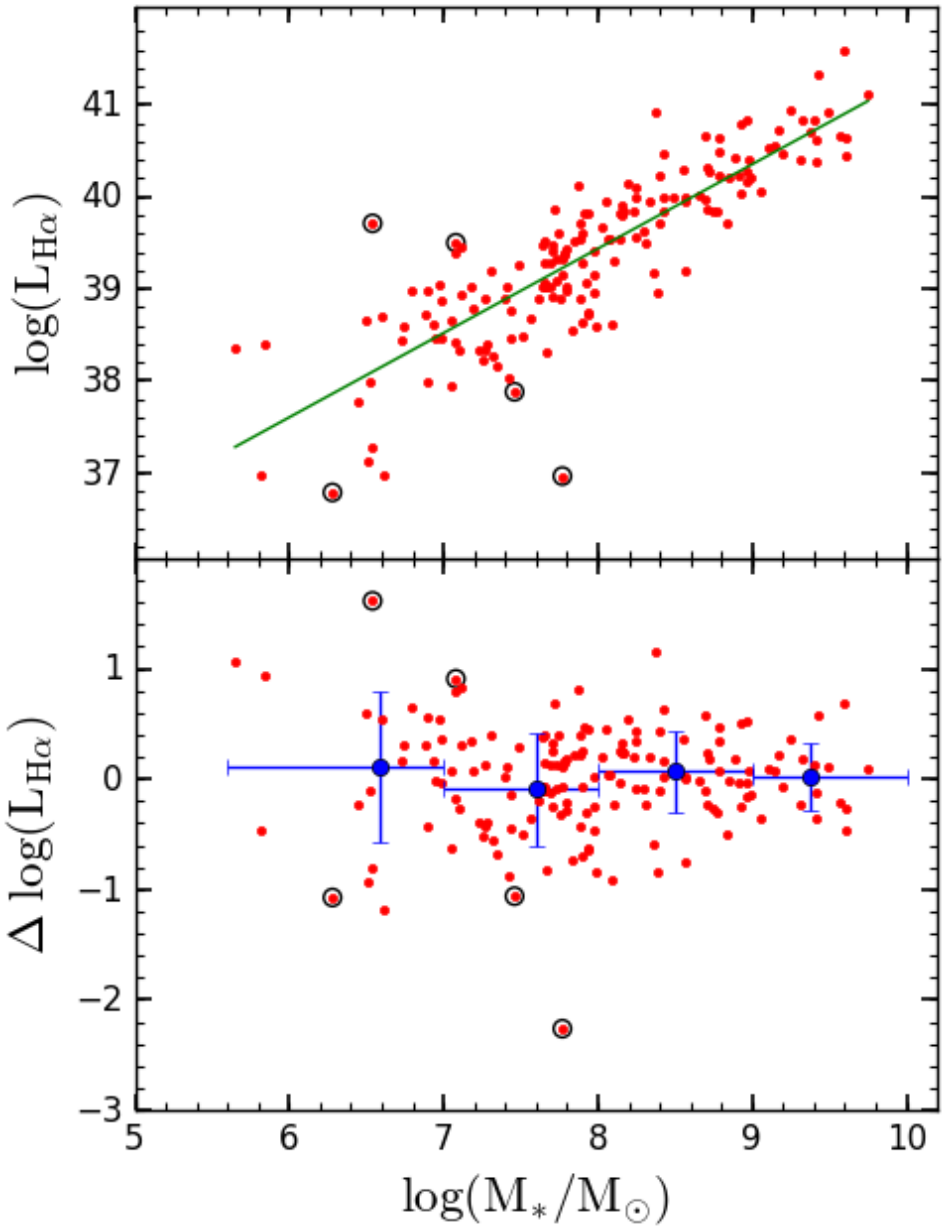

Figure 2.3: Top: $log(L_{H\alpha})$ vs. $log(M_*)$ relation for the W12 sample (red dots). The correlation between these two observables is known as the star-forming "main sequence." The black circles show outliers in $\log(L_{H\alpha}/L_{UV})$ (either > -1.8 or < -3.4) that are removed from the sample for the subsequent analysis. Bottom: The deviation of the $\log(L_{H\alpha})$, $\Delta\log(L_{H\alpha})$, from the linear relation green line in the top panel. The blue circles are the median in each stellar mass bin. The horizontal error bars denote the stellar mass range of each bin and the vertical error bars are the standard deviation in each bin. The scatter around the mean trend (green line) increases toward lower stellar masses, from 0.3 dex at $log(M_*) \sim 9.4$ to 0.7 dex at $log(M_*) \sim 6.6$.

translates to a maximum burst amplitude, relative to the average. But it is particularly useful when examined *in conjunction* with the $\log(L_{H\alpha}/L_{UV})$, as $\log(L_{H\alpha}/L_{UV})$ gives us time information, indicating how quickly (or how recently) a given galaxy has increased or decreased its SFR.

In Figure 2.4, we show the location of the W12 galaxies in the $\Delta\log(L_{H\alpha})$- $\log(L_{H\alpha}/L_{UV})$ plane in bins of stellar mass. The grey and black points correspond to the observed and dust corrected values, respectively. Note that the dust corrections are very small and do not change the shape of the correlations seen in Figure 2.4. The representative errors of 10-20% corresponding to $L_{H\alpha}$ and L_{UV} are shown in the bottom-right of each subplot in magenta. These errors are derived from the typical dispersion in dust attenuation as a function of absolute B-band magnitude, as reported in Lee et al. (2009). Specifically, galaxies in our sample span $-18.4 < M_B < -13$, for which the $L_{H\alpha}$ is uncertain by 10% for stellar masses below $10^8 M_\odot$ and 20% otherwise, and the L_{UV} is uncertain by 20% in the entire sample. As indicated before, the lower mass galaxies span a larger range in $\Delta\log(L_{H\alpha})$ *and* $\log(L_{H\alpha}/L_{UV})$. But what is most informative is that the two measurements are highly correlated in galaxies with $\log(M_*) < 8$. That is, we are not just fitting to the $\Delta\log(L_{H\alpha})$ and $\log(L_{H\alpha}/L_{UV})$ 1-D distributions, but also considering the correlations between the two.

We emphasize that we would like to use these distributions to infer SFHs of all of the galaxies in each mass bin. In order to do that, it is important to be sure that all galaxies in the bin are behaving in a similar manner, and that these measurements represent random samples of the same SFHs. One particular point of concern is the possibility that subsets of galaxies permanently reside above the SF main sequence ($\Delta\log(L_{H\alpha})> 0$) and

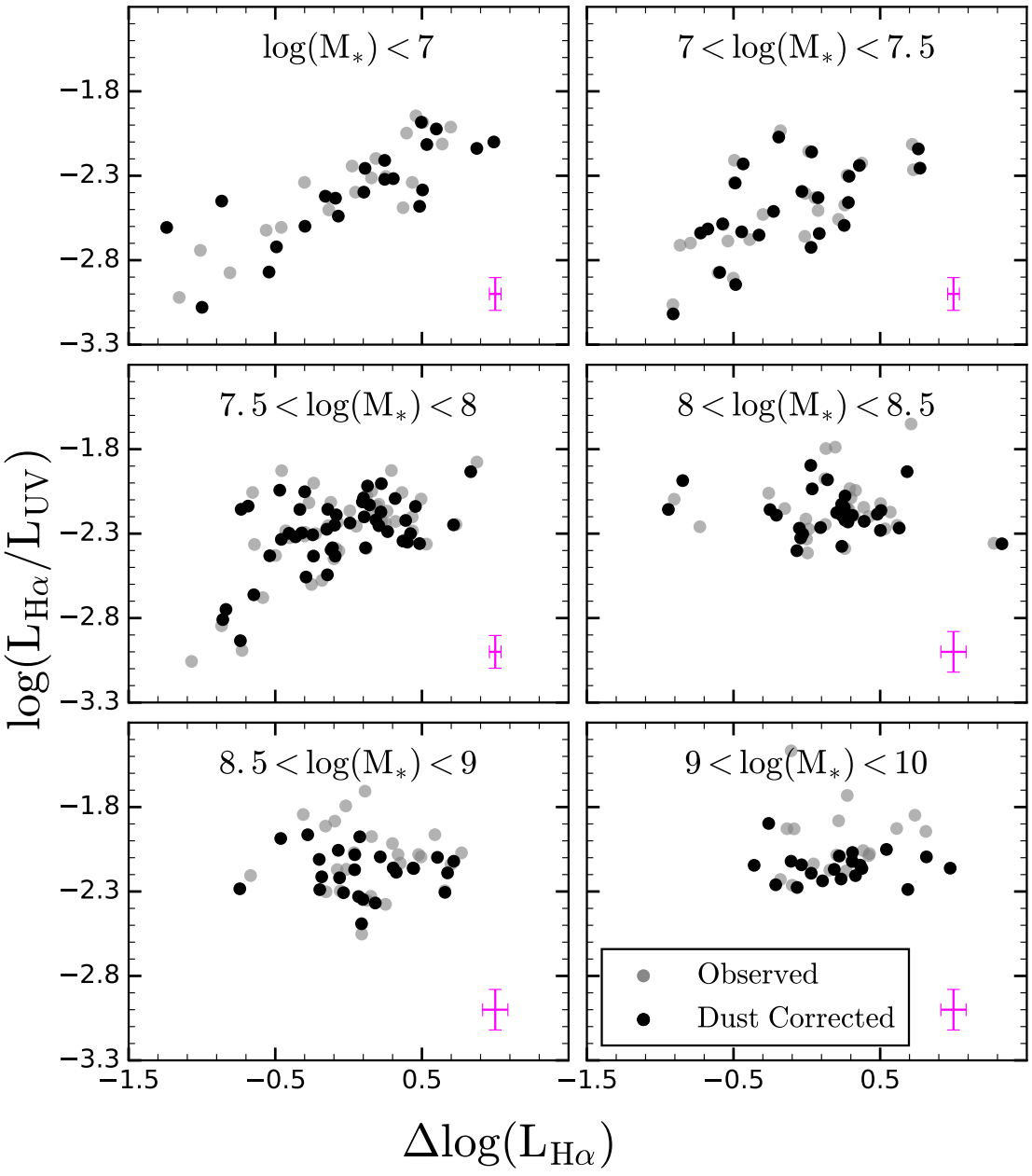

Figure 2.4: $\log(L_{H\alpha}/L_{UV})$ vs. $\Delta\log(L_{H\alpha})$ for the W12 sample in six different mass ranges. The grey and black points are the observed and dust corrected values respectively. Representative error bars of 10-20% in $L_{H\alpha}$ and L_{UV} derived from Lee et al. (2009) is shown in the bottom-right of each subplot in magenta. At high stellar mass, the galaxies span a narrow range in $\log(L_{H\alpha}/L_{UV})$. At low mass, the galaxies span a large range in $\log(L_{H\alpha}/L_{UV})$, and $\log(L_{H\alpha}/L_{UV})$ is positively correlated with $\Delta\log(L_{H\alpha})$. This correlations shows that, not only should these two observables be used to determine the properties of bursty star formation, but their 2-dimensional distribution should be considered.

others reside below the main sequence ($\Delta\log(L_{H\alpha})< 0$), for example because of different average gas infall rates in different environments. If that were the case, there would be no difference in the $\log(L_{H\alpha}/L_{UV})$ ratio of galaxies above and below the main sequence. However, Figure 2.4 shows a strong correlation between $\log(L_{H\alpha}/L_{UV})$ and $\Delta\log(L_{H\alpha})$ in low mass galaxies ($\log(M_*) < 8$). Specifically, galaxies that have higher than average SFRs have $\log(L_{H\alpha}/L_{UV}) \sim -2.2$, indicative of constant or rising SFRs, and galaxies that have lower than average SFRs have $\log(L_{H\alpha}/L_{UV}) < -2.5$, indicative of declining SFRs. This indicates that all of the galaxies in a given stellar mass bin have similar star formation histories.

2.5.2 The Exponential Burst Model

The SF histories of galaxies are not periodic, top-hat bursts, and are instead stochastic in nature. Because such simple models do not represent the actual SFHs, it is difficult to ascertain whether the best-fit parameters of the model are physically meaningful. Therefore, we are not particularly interested in confining ourselves to a highly parameterized, unphysical star formation history. As discussed above, the amplitude of the bursts can be determined from the width of the $L_{H\alpha}$ distribution. What remains unknown are the timescales for the burst and quench phases.

We have chosen to parameterize the rise and decline of a burst as an exponential in time such that

$$SFR(t) = \begin{cases} e^{t/\tau}, & \text{if } 0 \leq t < D \\ e^{-(t-2D)/\tau}, & \text{if } D < t \leq 2 \times D \end{cases} \tag{2.1}$$

where τ is the e-folding time, representing the typical timescale for significant change in the SFR. Part of our motivation for choosing an exponential burst model comes from the SFHs in some hydrodynamical simulations. For example star formation histories from the FIRE-2 simulations (Hopkins et al., 2018) indicate individual bursts with exponential rises and declines (see Figure 2.7). For the sake of simplicity, we assume that the galaxies' SFR rise and decline are both described with the same e-folding time, τ. With such a parametrization, we can target the timescale, independent of the absolute amplitude of the burst. Also, the SFHs are assumed to be periodic in repeating forms of Equation 2.1.

In the top left panel of Figure 2.5, we plot model star formation histories with $\tau = 10, 30, 100, 300$ Myr and an amplitude of $A = e^5 = 148$ (or equivalently a duration of 5τ). In the top right panel, we plot the associated $\log(L_{H\alpha}/L_{UV})$ vs. $\Delta\log(L_{H\alpha})$. Here $\Delta\log(L_{H\alpha})$ is calculated as the $log(L_{H\alpha})$ from Bruzual and Charlot (2003) synthetic stellar population (BC03) model subtracted from the value of $log(L_{H\alpha})$ for a constant SFR that is equal to the *average* SFR of the exponential model.

The $\tau = 100$ Myr model is highlighted in purple to demonstrate the motion of a bursty galaxy in this observable space. We note that the observable ratios are dependent on previous star formation. Thus, the plotted ratios are for a burst preceded by identical bursts. Obviously, as the galaxy SFR rises (burst phase), $\Delta\log(L_{H\alpha})$ increases and the galaxy moves to the right in the plot. As the galaxy SFR declines (quench phase), $\Delta\log(L_{H\alpha})$

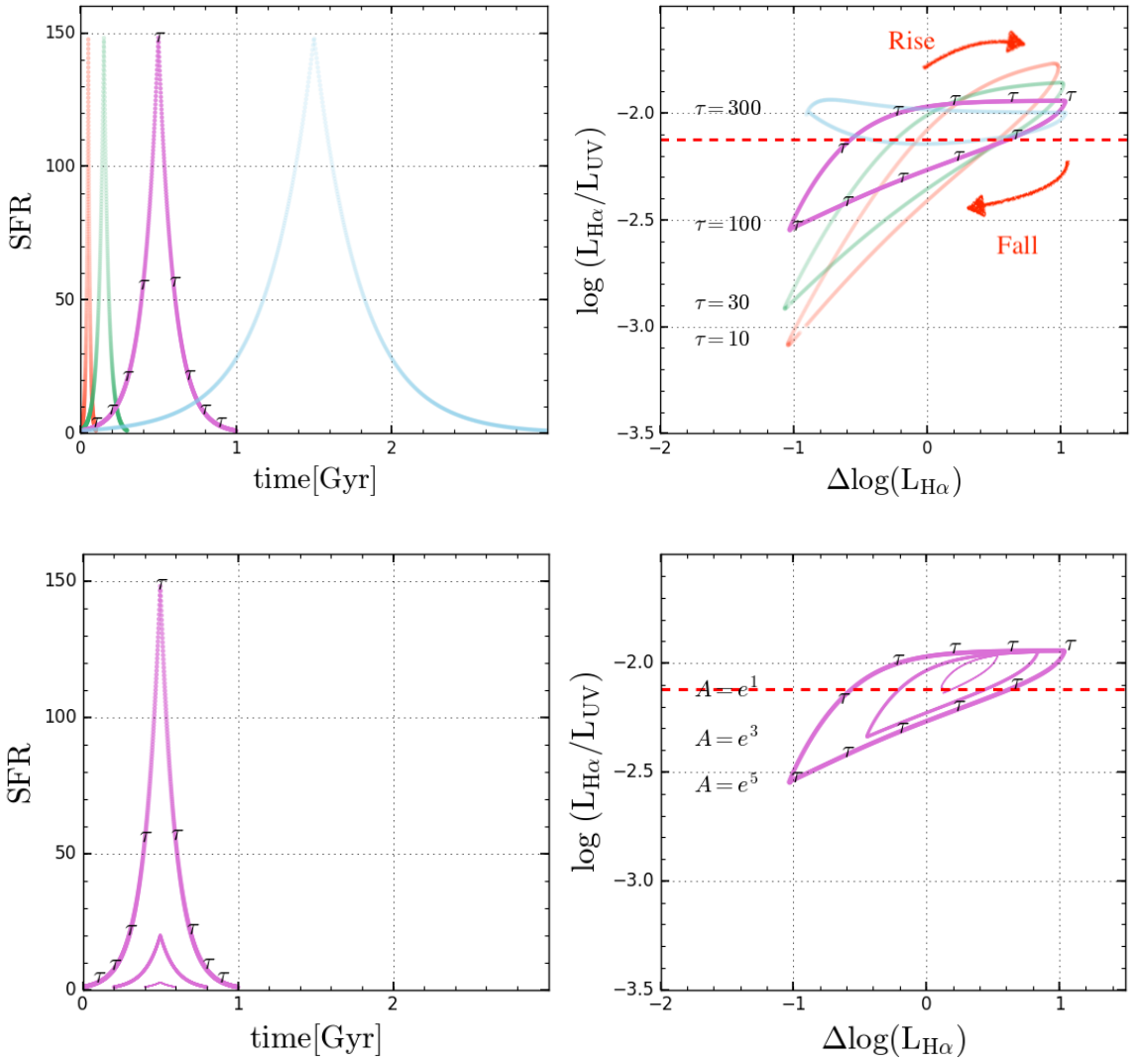

Figure 2.5: Top Left: SF history of four exponentially rising and declining burst with varying $\tau = 10, 30, 100, 300$ Myr and a fixed amplitude of $A = e^5 = 148$ (or equivalently a duration of 5τ). Top Right: The associated $\log(L_{H\alpha}/L_{UV})$ - $\Delta\log(L_{H\alpha})$ for the SFHs in left panel. We highlight the $\tau = 100$ Myr model, and place 'τ' symbols in intervals of $\Delta t = \tau$. The equilibrium value (assuming a constant SFR) of $\log(L_{H\alpha}/L_{UV})$=-2.12 is marked with red dashed line. As τ decreases, the $\log(L_{H\alpha}/L_{UV})$ - $\Delta\log(L_{H\alpha})$ slope gets steeper. Bottom : Same as top panels except for models with fixed $\tau = 100$ Myr and varying amplitudes of $A = e^1, e^3$ and e^5. The $\log(L_{H\alpha}/L_{UV})$ - $\Delta\log(L_{H\alpha})$ slope is unchanged but the points span over smaller $\Delta\log(L_{H\alpha})$ ranges.

Note that in an exponential model, the galaxies spend equal amounts of time in equal intervals of $\Delta\log(L_{H\alpha})$.

decreases and the galaxy moves to the left in the plot. The motion in $\log(L_{H\alpha}/L_{UV})$ is more complicated, depending on the timescale of change in SFR, τ. For long timescales, $\tau > 300$ Myr, both of the luminosities in the $\log(L_{H\alpha}/L_{UV})$ ratio have time to react and accurately trace the SFR. Therefore, $\log(L_{H\alpha}/L_{UV})$ does not significantly change as the SFR declines. However, if $\tau < 300$ Myr, L_{UV} lags $L_{H\alpha}$ in tracing the decline in SFR, and $\log(L_{H\alpha}/L_{UV})$ will decrease as $\Delta\log(L_{H\alpha})$ decreases. As τ decreases, the slope of the curves increase. However, the slope saturates at ~ 0.6 for $\tau < 30$ Myr. Therefore, examination of galaxies in this observable space is only useful for identifying changes in SFR on timescales of $30 < \tau < 300$ Myr. The bottom panels of Figure 2.5 indicate the SFHs and associated $\log(L_{H\alpha}/L_{UV})$ - $\Delta\log(L_{H\alpha})$ relation of three exponential burst models for the case where the e-folding time (τ) is fixed to 100 Myr and the amplitudes are allowed to vary from $A = e^1, e^3$ and e^5. The model with larger amplitude (e^5) spans a larger $\Delta\log(L_{H\alpha})$ axis, while the slope remains unchanged in all three models.

We note that in the exponential model, the galaxies are evenly spread in $\Delta\log(L_{H\alpha})$ during the transition from quench to burst and vice versa. In contrast, the periodic top-hat burst model results in most galaxies having two $\Delta\log(L_{H\alpha})$ values, with few points in between. The observed ratios are roughly evenly distributed in $\Delta\log(L_{H\alpha})$, similar to the exponential model.

2.5.3 Results

In Figure 2.6, we again plot the W12 data in this $\log(L_{H\alpha}/L_{UV})$ - $\Delta\log(L_{H\alpha})$ plane. As mentioned above, the data clearly show that even though the SFR of the high mass galaxies changes significantly, the $\log(L_{H\alpha}/L_{UV})$ ratio does not. In the context of our

exponential burst model, this indicates that the changes in SFR are slow, with τ300 Myr. At low mass, however, the $\log(L_{H\alpha}/L_{UV})$ is highly correlated with $\Delta\log(L_{H\alpha})$, suggesting that the SFRs change rapidly, with τ100 Myr.

In Figure 2.6, we also plot the tracks (cyan) for values of τ and A that best match the data in each mass range. The summary of these values are also reported in Table 2.1 for a better comparison. We note that we do not perform any probabilistic analysis to determine the best fit exponential models of each mass bin. Due to systematic uncertainties (e.g. extinction correction, metallicity, stellar models, escape fraction), the models may not precisely reproduce the data. We therefore determine (by eye) approximate model parameters that reproduce the slope and breadth of the data the observed $\log(L_{H\alpha}/L_{UV})$ vs. $\Delta\log(L_{H\alpha})$ plane. A 10-20 % observational uncertainty is added to the model (in both $L_{H\alpha}$ and L_{UV}) to mimic the true uncertainty in the data, as discussed in Section 2.5.1. The approximate values of τ and A are written in the bottom right of each subplot. Two trends are clear with mass. First, the amplitudes – the ratio of maximum to minimum SFR (or $L_{H\alpha}$) in galaxies of the same mass – increase toward lower mass ($A \sim 10$ for $\log(M_*) > 9$ to $A \sim 100$ for $\log(M_*) < 7.5$). Second, the timescales for changes in SFR (τ) decrease with decreasing stellar mass, with $\tau > 300$ Myr for $\log(M_*) > 8.5$ and $\tau < 30$ Myr for $\log(M_*) < 7.5$.

We note that, within the scatter, the slopes of the data in the $\log(L_{H\alpha}/L_{UV})$ - $\Delta\log(L_{H\alpha})$ plane are roughly the same for all galaxies with $\log(M_*) > 8.5$ (slope ~ 0) and for all galaxies with $\log(M_*) < 7.5$ (slope ~ 0.6). As noted above, the $\log(L_{H\alpha}/L_{UV})$ ratio is most useful for identifying changes in SFR on timescales of $\tau \sim 100$ Myr. Thus, it appear

that the stellar mass of $\log(M_*) \sim 8$ (at $z = 0$) represents the critical mass at which the timescale for change in SFR is approximately $\tau \sim 100$ Myr. This is an observational result, and is true regardless of the physical mechanisms involved.

It is noteworthy that Meurer et al. (2009) looked at the burstiness in the $\log(L_{H\alpha}/L_{UV})$ - $\Sigma_{H\alpha}$ plane, which is very similar to the observables we analyze (replacing $\Delta\log(L_{H\alpha})$ with $H\alpha$ surface brightness). In addition, they used Gaussian bursts and gasps, which are exponential in the beginning and end, similar to our model bursts. Indeed, their models show a similar behavior in $\log(L_{H\alpha}/L_{UV})$-$\Sigma_{H\alpha}$ as our exponential models, especially in the gasp phase. However, their models have a very significant difference from ours - they assume a low-level, constant SFR when not in a burst or gasp. This assumption requires that the galaxies have a high $\log(L_{H\alpha}/L_{UV})$ before a new burst/gasp starts. Ultimately, this assumption makes it impossible to reproduce the observed $\log(L_{H\alpha}/L_{UV})$ - Σ_R (optical surface brightness) distribution of the galaxies, because it can not produce galaxies with both low $\log(L_{H\alpha}/L_{UV})$ (which can be produced only with a quick downturn in star formation) and low Σ_R (which can not be produced with a quick downturn in star formation, if one assume that galaxies start with a high Σ_R). Meurer et al. (2009) therefore concluded that the star formation history can not fully explain the low $\log(L_{H\alpha}/L_{UV})$ ratio in low surface brightness galaxies.

Within the framework of our model, however, these low surface brightness galaxies with low $\log(L_{H\alpha}/L_{UV})$ are naturally explained by low mass galaxies (which typically have low optical surface brightness, de Jong and Lacey, 2000) with rapidly declining SFR. Ultimately, we believe that our splitting of the sample into different mass bins (which, on

average, have different optical surface brightness and different timescales), and our assumption that no baseline, constant SFR is required in our models, allows us to naturally explain the $L_{H\alpha}$ and L_{UV} distributions with SFHs alone.

There have also been investigations of the properties of burty galaxies at moderate-redshift ($0.4 < z < 1$) in CANDELS GOODS-N by looking at the $L_{H\beta}/L_{UV}$ (Guo et al., 2016a). In this paper, they observed a decreasing trend of $L_{H\beta}/L_{UV}$ towards low masses similar to the local sample of W12. They found a correlation between the $L_{H\beta}/L_{UV}$ and the $L_{H\beta}$-derived specific SFR (sSFR) of their sample, as evidence for bursty star formation. They conculde that the galaxies in their sample are also bursty. But the bursty SF occurs below a high mass threshold than at lower redshift ($M_* < 10^9$ $M_\odot$ compared to $M_* < 10^8$ $M_\odot$ at low redshift).

(1) $log(M_*)$	(2) τ [Myr]	(3) A
≤ 7	< 30	100
$7 - 7.5$	< 30	100
$7.5 - 8$	30	30
$8 - 8.5$	100	10
$8.5 - 9$	300	10
$9 - 10$	> 300	10

Table 2.1: Best fit values of the exponential burst parameters: the e-folding time (τ) in column (2) and amplitude (A) in column (3) for six different mass bins from lowest to the highest stellar masses (column (1)).

2.6 Discussion

So far, we have constrained the parameters of bursty star formation by looking at the position of the observed galaxies in the $\log(L_{H\alpha}/L_{UV})$ - $\Delta\log(L_{H\alpha})$ plane. We used an

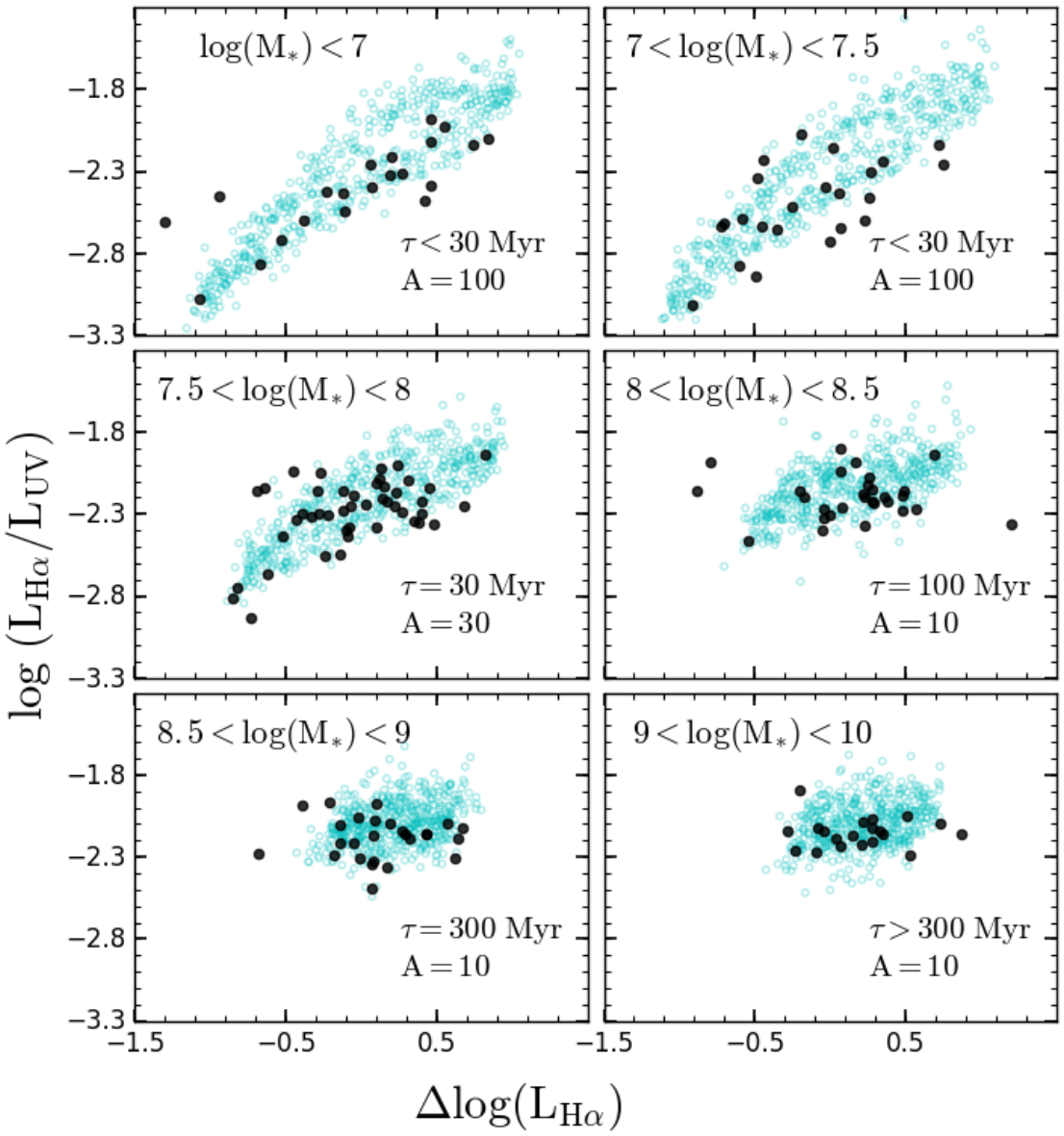

Figure 2.6: Location of modeled galaxies in the $\log(L_{H\alpha}/L_{UV})$ - $\Delta\log(L_{H\alpha})$ plane (cyan circles), undergoing periodic, exponential bursts of SF with different timescales, τ, and amplitude, A, sorted by mass. Note that the time scales in the two lowest mass bins read $\tau < 30$ Myr because the slope of the relation does not change below that time scale. We used $\tau = 10$ Myr for these two mass bins. A 10-20% systematic uncertainties corresponding to errors reported in Figure 2.4 is added to each luminosity to mimic the observational uncertainties. The black points are the W12 observed data. The best-fit values of τ and A are written in the bottom right of each subplot. The time scale for changes in SFR increase with increasing stellar mass.

exponential SF model to reproduce the $\log(L_{H\alpha}/L_{UV})$ - $\Delta\log(L_{H\alpha})$ distribution and found the best fit time scales and amplitudes of bursts as a function of stellar mass.

In this section, we compare our predictions with hydrodynamical simulations. We also consider the effect of stochastic IMF sampling within our $\log(L_{H\alpha}/L_{UV})$ - $\Delta\log(L_{H\alpha})$ framework. Finally, we discuss the effect of the ionizing photon escape fraction and dust correction uncertainties.

2.6.1 Comparison To Hydrodynamical Simulations

Many high resolution hydrodynamical simulations of dwarf galaxies implement stellar feedback and supernovae, resulting in bursty SF Governato et al. (2010); Domínguez et al. (2015). The effects of bursty SFHs on sample selection and interpretation of observables has been extensively investigated by Domínguez et al. (2015) using the SFHs from hydro-dynamical simulations. The FIRE-1 and FIRE-2 (Feedback In Realistic Environments) simulations (Hopkins et al., 2014, 2018), implement prescriptions for a variety of stellar and supernovae feedback that are not tuned to reproduce observed scaling laws. Galaxies of different stellar masses are simulated, from dwarfs to Milky Way-like systems, reproducing the empirical relations between galactic observables such as the stellar mass-halo mass relation, the mass-metallicity relation, etc. Due to its high resolution and focus on stellar/supernovae feedback, the FIRE-2 simulations are well-suited for our goal of studying burstiness in dwarf galaxies.

Sparre et al. (2017) studied $L_{H\alpha}$ and L_{UV} as proxies of the SFR averaged over 10 and 200 Myr and found that the FIRE-1 simulations (Hopkins et al., 2014) are more bursty than observed galaxies. Specifically, the FIRE-1 galaxies display a larger range in

$L_{H\alpha}/L_{UV}$ than the observed galaxies of W12 between $8 < \log(\mathrm{M}_*[\mathrm{M}_\odot]) < 9.5$. The FIRE-2 simulations (Hopkins et al., 2018) used improved numerical accuracy, resulting in more accurate treatments of cooling and recombination rates, gravitational force softening and numerical feedback coupling. However, the core physics is the same as FIRE-1. These enhancements lead FIRE-2 to produce more realistic bursts of SF. FIRE-2 also contains a larger sample of galaxies than the previous version, allowing a better understanding of variations in galaxy properties. The detailed properties of the individual simulations can be found in Hopkins et al. (2018); El-Badry et al. (2018a).

We use the star formation histories of the FIRE-2 galaxies, which span a similar range in stellar mass over their last 2 Gyrs (corresponding to $z = 0.15 - 0$) to the W12 mass range, to determine their location and evolution in the $\log(L_{H\alpha}/L_{UV})$ vs. $\Delta\log(L_{H\alpha})$ plane, and compare them with the observed W12 sample.

Figure 2.7 shows three examples of star formation histories of FIRE-2 simulated galaxies, whose name and stellar mass at $z = 0$ are written on the top-left of each panel. We specifically chose galaxies with a different range of stellar masses. The galaxies have bursts of SF with a short amount of time in the peak. We see that galaxies rise and decline quickly in a roughly exponential form. For illustration purposes, we marked some of these exponential bursts in Figure 2.7 in magenta and fit equation 2.1 to individual bursts (using a curve fit Scipy package from Python) in order to find an estimate of rising and falling timescales for these galaxies. Based on this simple fitting, all three of these galaxies indicate time scales of $\tau < 15$ Myr.

The L_{UV} and $L_{H\alpha}$ fluxes are derived by convolving the simulated star formation

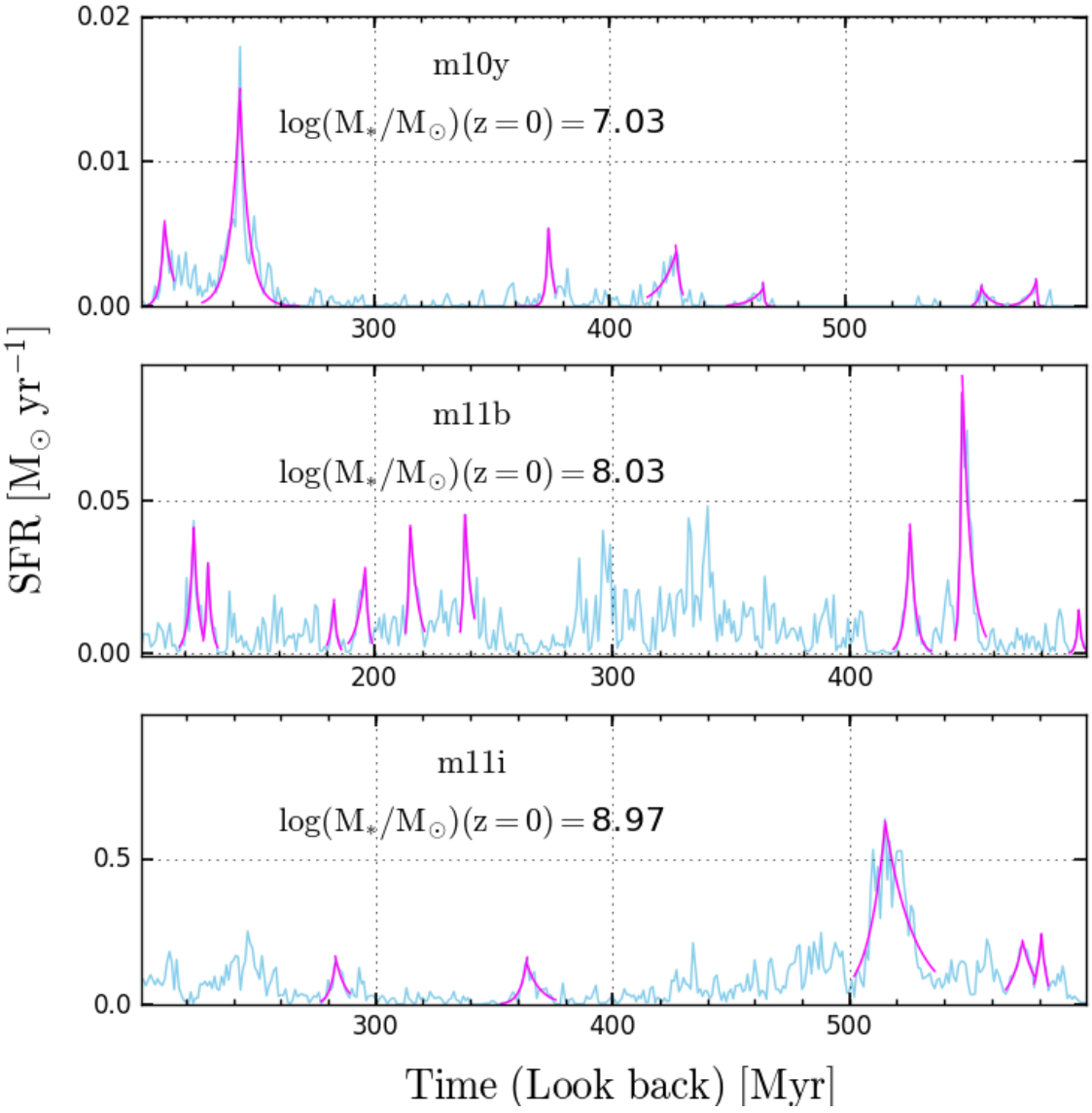

Figure 2.7: Star formation histories of three galaxies in the FIRE-2 simulations (Hopkins et al., 2018) (cyan). The name and stellar mass of the galaxies at $z = 0$ are labeled in the top-left of each panel. The magenta lines are the best fit exponential functions to the individual bursts. The marked bursts all have e-folding time scale of τ below 15 Myr.

histories over the last 2 Gyrs with the Hα and UV luminosity evolution from single stellar population models (Bruzual and Charlot, 2003) with stellar metallicity of $0.2Z_{\odot}$. This is the same method as described for our parametrized bursty star formation in the Appendix. We note that in the low mass galaxies in which we are most interested, the vast majority of stars are formed in-situ and not acquired in mergers (Fitts et al., 2018). Furthermore, most of the mergers happened at $z > 3$, so the accreted stars are old and will not affect the $L_{H\alpha}$ or L_{UV} (Fitts et al., 2018) calculations at late times.

In figure 2.8 we make the $\log(L_{H\alpha}/L_{UV})$ vs. $\Delta\log(L_{H\alpha})$ plot for FIRE2-simulated galaxies, where the color indicates the density of points at any location on the plot. Overlaid is the W12 observed sample in black circles. We calculate the median $L_{H\alpha}$ from the linear fit to the $L_{H\alpha}$ vs. mass relation for FIRE-2 galaxies and subtract this to determine $\Delta\log(L_{H\alpha})$. The names of the plotted FIRE-2 galaxies are labeled in red. One common feature that can be seen in both the observations and simulation is that the low mass galaxies exhibit a larger spread in the $\log(L_{H\alpha}/L_{UV})$ vs. $\Delta\log(L_{H\alpha})$ space while the spread becomes smaller at higher masses. Nonetheless, there are some discrepancies between them.

As mentioned before, the observations show no relation between $L_{H\alpha}/L_{UV}$ and $\Delta\log(L_{H\alpha})$ above 10^8 $M_{\odot}$, but show a strong correlation below 10^8 $M_{\odot}$. This is seen in the slope of the best-fit lines to the data in Figure 2.8. However, the simulated galaxies show a strong correlation, with a similar slope, at all stellar masses (red dashed line in Figure 2.8. Comparison with our exponential burst models (Section 2.5.2) on the FIRE-2 galaxies, indicates that the bursts/quenches have e-folding times of τ below 30 Myr in the simulated galaxies at all masses. However, the W12 data suggest that the e-folding

time increases toward higher stellar masses. In particular, at stellar masses above 10^8, the FIRE-2 simulations have far faster bursts ($\tau < 30$ Myr) than the timescales implied by the observation of real galaxies (τ300 Myr). We therefore suggest that the rapid bursts in the FIRE-2 simulations of more massive galaxies should be examined to determine possible shortcomings in the existing feedback prescriptions.

We note here that although the $\log(L_{H\alpha}/L_{UV})$ and $\Delta\log(L_{H\alpha})$ distributions are similar to the observed galaxies, it is the examination of the $\log(L_{H\alpha}/L_{UV})$ - $\Delta\log(L_{H\alpha})$ 2-dimensional space that allows us to recognize that the time scales for the bursts in more massive galaxies may not be correct.

One other difference between the simulation and observation that becomes more significant at masses below $10^{7.5}M_{\odot}$ is that the simulation produces larger $\log(L_{H\alpha}/L_{UV})$ than what is observed in real galaxies. We address this offset in section 2.6.3.

We choose galaxy "m11b," with stellar mass of $10^8 M_{\odot}$ at $z = 0$, as an example to demonstrate the effect of star formation rate change on the $\log(L_{H\alpha}/L_{UV})$ - $\Delta\log(L_{H\alpha})$ relation. In Figure 2.9, we plot a 50 Myr segment of the recent SFH of this galaxy and marked each Myr in a color gradient as the time advances from dark blue to dark red as is shown on the left plot. The SFH at each point is averaged over its last three Myrs as it takes about three Myrs for the $L_{H\alpha}$ to react to the change in star formation rate. On the right panel, we plot the $\log(L_{H\alpha}/L_{UV})$ - $\Delta\log(L_{H\alpha})$ associated with the original (un-smoothed) SFH for which the colors represent the corresponding time on the left panel of the same color. When the SFR begins to rise, the galaxy moves in the $\log(L_{H\alpha}/L_{UV})$ - $\Delta\log(L_{H\alpha})$ plane from bottom-left to the top-right (3 to 13, 21 to 23, 30 to 36 Myrs). When the SFR

declines quickly, the galaxy moves back toward the bottom left (13 to 21, 23 to 30, 36 to 41 Myr). Moreover, the larger amplitude changes in SFR give rise to larger changes in the $\log(L_{H\alpha}/L_{UV})$ - $\Delta\log(L_{H\alpha})$ plane (compare the large amplitude decline from 36 to 41 Myr to the smaller amplitude decline from 23 to 30 Myr). This behavior is consistent with the predictions from our model.

2.6.2 Stochastic IMF Sampling

So far we have discussed the luminosity distributions from the perspective of bursty star formation, assuming that the IMF is well-sampled in all galaxies at all SFRs. However, it may be the case that stars form in a stochastic manner such that low mass galaxies with a limited amount of gas form massive stars less frequently. Thus, it may not be appropriate to assume a fully sampled mass function in low mass galaxies with low SFRs. This will result in a deficit of very high mass stars, and can significantly change the $\log(L_{H\alpha}/L_{UV})$ and $\Delta\log(L_{H\alpha})$distributions, even in a galaxy with a constant SFR. If this effect is large, it can incorrectly cause us to assume that a galaxy is undergoing bursty star formation.

Stars are born in star clusters and the distribution of clusters is called the initial cluster mass function (ICMF). The ICMF is typically modeled as a power-law, and observations suggest a slope of 2 (Zhang and Fall, 1999; Fall et al., 2009; Lada and Lada, 2003). Clusters of different masses are formed according to the probability given by the ICMF. Then, stars in each cluster are formed according to the probability given by the initial stellar mass function (ISMF).

Because some studies have indicated that IMF sampling can explain some of the

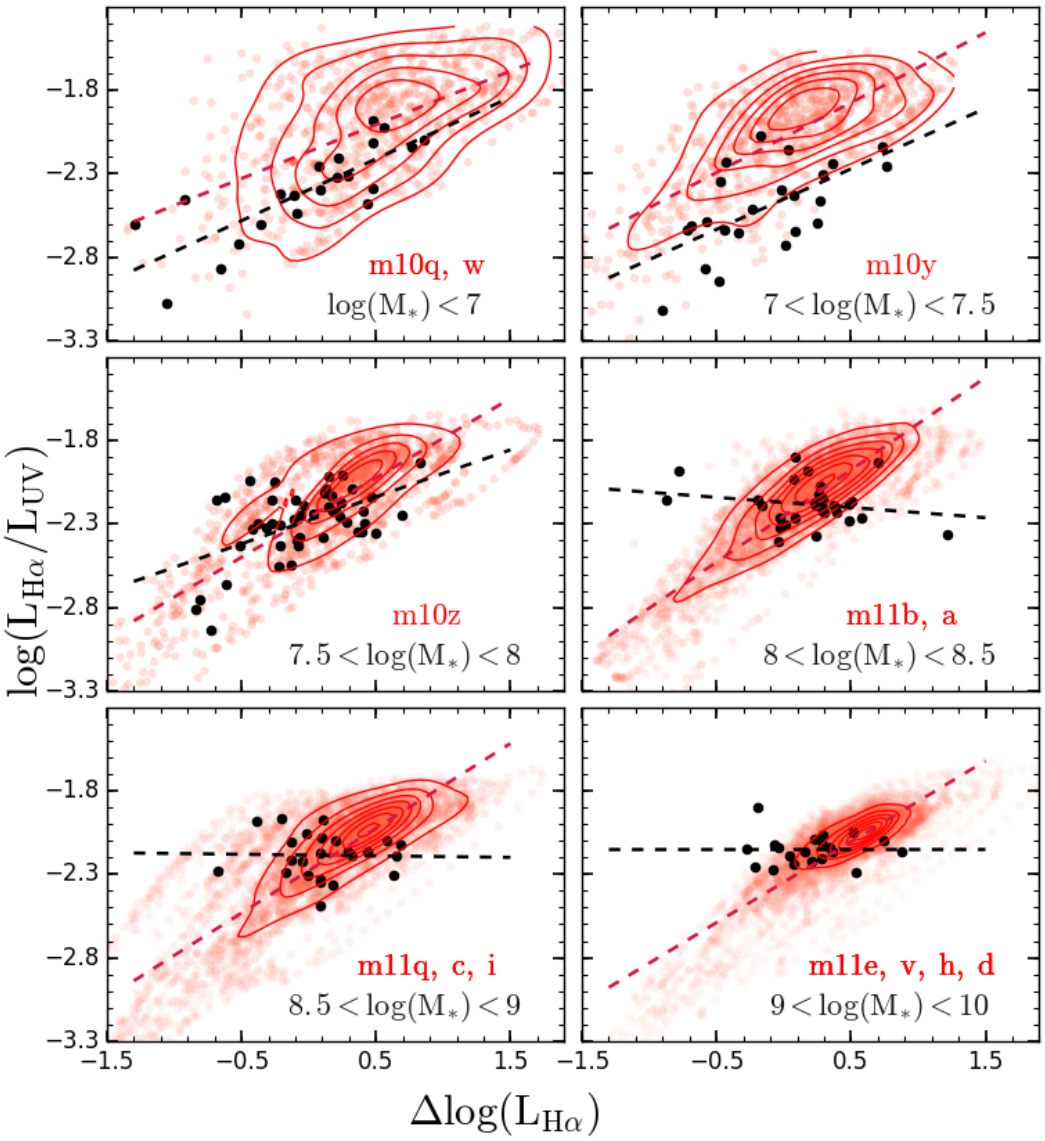

Figure 2.8: The $\log(L_{H\alpha}/L_{UV})$ vs. $\Delta\log(L_{H\alpha})$ relation for FIRE2-simulated galaxies (red circles and contours) and W12 data for local galaxies (black circles). The FIRE-2 galaxies are selected to be within the specified mass range at z=0. The names of the FIRE-2 galaxies are labeled in red. Red and black dashed lines are the best-fit line to the simulated and observed galaxies, respectively. We note that in the lowest mass galaxies ($\log(M_*) < 7$), a significant fraction of galaxies exhibit no star formation for long periods of time and would lie off of the bottom left of the plot. The simulated galaxies all span a similar range in $\Delta\log(L_{H\alpha})$ as the observed galaxies, suggesting similar burst amplitudes. However, the simulated galaxies at higher mass show a positive correlation between $\log(L_{H\alpha}/L_{UV})$ and $\Delta\log(L_{H\alpha})$that is not seen in the observed galaxies, suggesting that the timescales for change in SFR is too short in simulated galaxies.This is also evident from the slope of the red dashed lines in these mass bins.

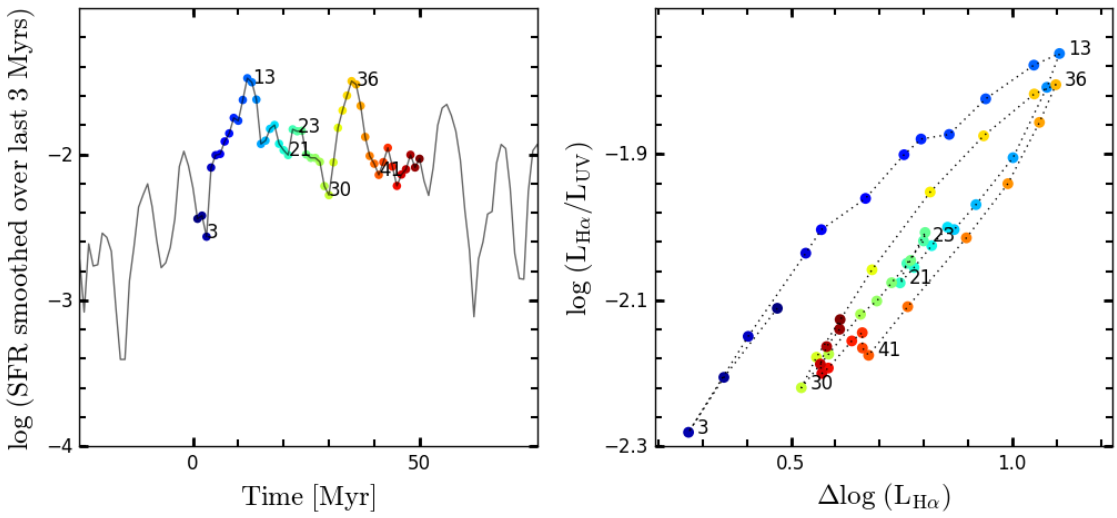

Figure 2.9: Left: The SFH smoothed over the last three Myrs for a 50 Myr segment of the recent SFH in galaxy "m11b" with $10^8 M_\odot$ stellar mass at present ($z = 0$). Right: The $\log(L_{H\alpha}/L_{UV})$ vs. $\Delta\log(L_{H\alpha})$ associated with the original (un-smoothed) SFH on the left panel. Colors and numbers represent the same star formation time on both panels. This is clear that the $\log(L_{H\alpha}/L_{UV})$ - $\Delta\log(L_{H\alpha})$ traces the SFR change when SFR is smoothed over the last three Myrs. As star formation rises and declines, it moves diagonally from bottom-left to top-right and back in $\log(L_{H\alpha}/L_{UV})$ - $\Delta\log(L_{H\alpha})$ plane respectively.

observed $\log(L_{H\alpha}/L_{UV})$ distributions, we attempt here to model stochastic IMF sampling in the W12 galaxies. SLUG (Stochastically Lighting Up Galaxies da Silva et al., 2012, 2014) is a code that considers stochastic sampling of both the ICMF and, then, the ISMF to determine the spectrum of star-forming galaxies. We use SLUG to determine the effects of ICMF and ISMF stochastic sampling to determine if poor sampling of the high mass ends is responsible for the large scatter in $\log(L_{H\alpha}/L_{UV})$ that we observe in low mass galaxies. We use stellar metallicities from Table 2.2, assume a power-law ICMF with slope of $\beta = 2$, and Padova stellar tracks with thermally pulsing AGB stars and a Chabrier ISMF. In each mass bin, we use the median $L_{H\alpha}$ of all galaxies to determine a typical SFR in that mass bin, assuming the Kennicutt (1998) conversion. The SLUG code takes the input (constant) SFR, and stochastically produces stars, outputting spectral energy distributions every 5 Myr. We assume that all ionizing photons result in a photoionization, and calculate the resulting $L_{H\alpha}$ based on case-B recombination. We determine the $\Delta\log(L_{H\alpha})$ distribution by subtracting the median from the $L_{H\alpha}$ distribution.

In Figure 2.10, red circles are the output SLUG data and black circles are the W12 observed data. In this figure, we show the evolution of galaxies with constant SFR in the $\log(L_{H\alpha}/L_{UV})$ vs. $\Delta\log(L_{H\alpha})$ plane due to stochastic formation of massive stars. When high mass stars are abundant, the galaxy is high in both $\log(L_{H\alpha}/L_{UV})$ and $\Delta\log(L_{H\alpha})$. When high mass stars are not abundant, the galaxy is low in both $\log(L_{H\alpha}/L_{UV})$ and $\Delta\log(L_{H\alpha})$. Thus, there is a tight correlation between $\log(L_{H\alpha}/L_{UV})$ and $\Delta\log(L_{H\alpha})$, with a slope of ~ 1 in all mass bins. We note that a slope of ~ 1 suggests that $L_{H\alpha}$ is changing significantly, while the L_{UV} is roughly constant.

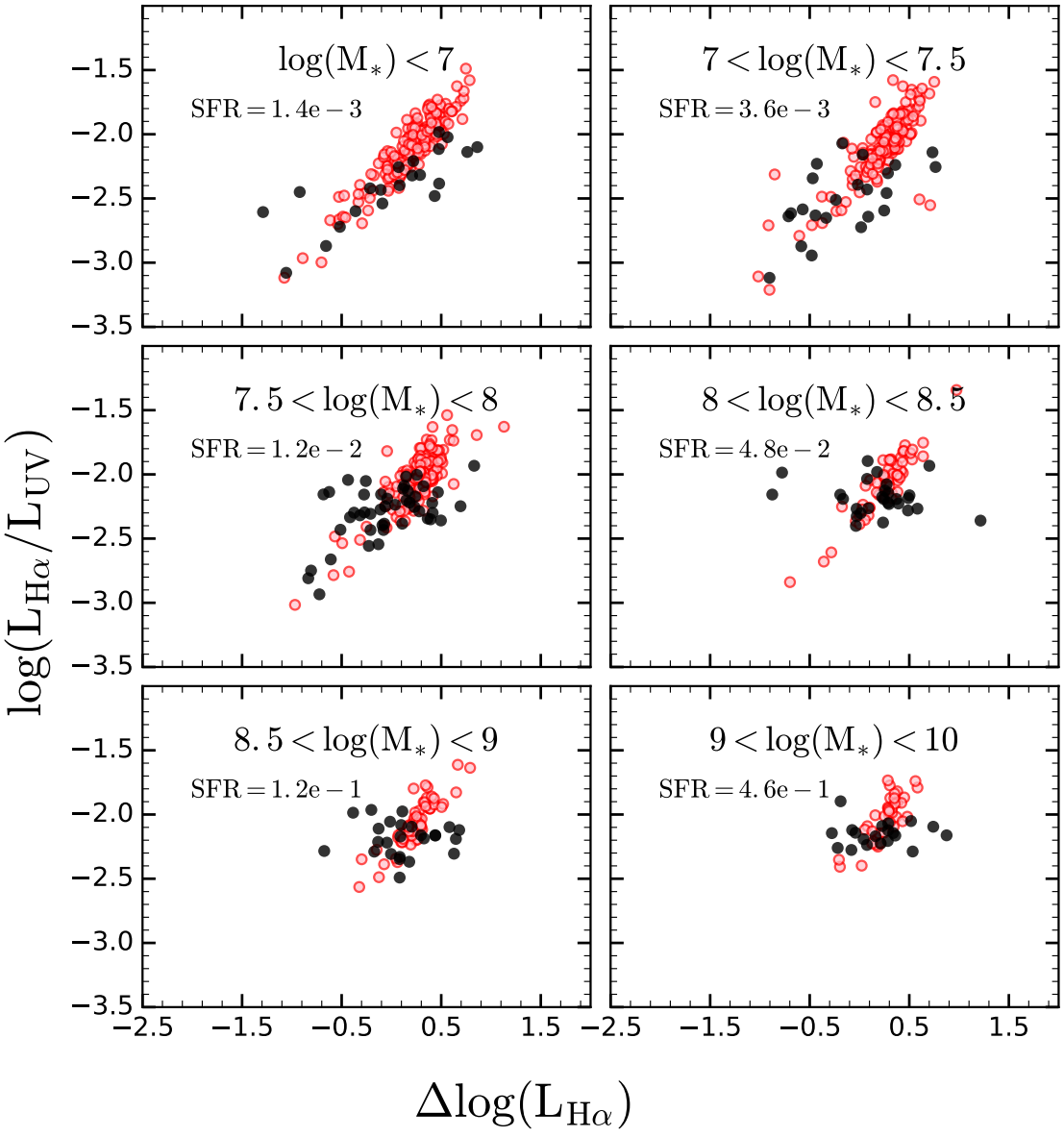

Figure 2.10: The $\log(L_{H\alpha}/L_{UV})$ vs. $\Delta\log(L_{H\alpha})$ relation due to stochastic sampling of the ICMF and ISMF. Red points are SLUG-synthesized galaxies and black points are the W12 observed galaxies. The input (constant) SFR is derived from the average $L_{H\alpha}$ of the W12 sample for each mass bin. Though the SFR is constant, the luminosities change considerably as high mass stars are stochastically created. When high mass stars are abundant, the galaxy is high in both $\log(L_{H\alpha}/L_{UV})$ and $\Delta\log(L_{H\alpha})$. When high mass stars are not abundant, the galaxy is low in both $\log(L_{H\alpha}/L_{UV})$ and $\Delta\log(L_{H\alpha})$. Thus, there is a tight correlation between $\log(L_{H\alpha}/L_{UV})$ and $\Delta\log(L_{H\alpha})$, with a slope of ~ 1 in all mass bins.

The SLUG points roughly produce the width of the observed $\Delta\log(L_{H\alpha})$ distribution. However, SLUG significantly overpredicts the observed slope of the $\log(L_{H\alpha}/L_{UV})$ vs. $\Delta\log(L_{H\alpha})$trend (slope of 1 vs. ~ 0.5). Therefore, it appears that bursty star formation is responsible for most of the observed spread in the $\log(L_{H\alpha}/L_{UV})$ and $\Delta\log(L_{H\alpha})$ distributions. This is somewhat surprising, as the very low SFRs in our low mass bins should suggest incomplete sampling of the high mass end of the ISMF. This may be reconciled if star-forming clusters in gas-rich, low mass galaxies are "top-heavy" relative to the assumed ICMF above.

Eldridge (2012) added the effect of binary stars to the stochastic IMF sampling and looked at the $\log(L_{H\alpha}/L_{UV})$ distribution of the W12 sample. Binary star mergers and mass transfer both produce more massive stars than were present in the initial population, which blurs some of the observational differences between different IMF sampling in their models. However, they conclude that the scatter in the $\log(L_{H\alpha}/L_{UV})$ distribution is not due to the IMF sampling method but it depends more on the bursty star formation history of each individual galaxy.

Furthermore, more constraints can be imposed on IMF sampling by limiting the ISMF and ICMF at the high mass end, such that the maximum stellar mass in star clusters is limited by the mass of the cluster and that the mass of the cluster itself is constrained by the SFR. This method is referred to as the integrated galactic IMF (IGIMF Kroupa and Weidner, 2003). Pflamm-Altenburg et al. (2007); Pflamm-Altenburg et al. (2009); Lee et al. (2009) argue that the IGIMF explains the observed $\log(L_{H\alpha}/L_{UV})$ distribution of their sample. However, Fumagalli et al. (2011) suggest that the imposed high mass limits

of both the ICMF and the ISMF in the IGIMF models lead to a dramatic reduction in the luminosity scatter at low SFRs, which is inconsistent with observations (Andrews et al., 2013, 2014).

2.6.3 Escape of Ionizing Photons

We note that our models consistently extend to higher $\log(L_{H\alpha}/L_{UV})$ values than are observed at all stellar masses (see Figure 2.6), but especially at $\log(M_*) < 8$. This ratio is affected by stellar metallicity, so part of this discrepancy could be alleviated if we assumed higher metallicity values. However, we are using metallicities that are consistent with measured mass-metallicity trends in low redshift galaxies (Andrews and Martini, 2013) and, in any case, the offset between the observed galaxies and models in the low-mass galaxies (~ 0.3 dex) is larger than can be explained by stellar metallicity alone (~ 0.1 dex difference between 0.2 $Z_\odot$ and $Z_\odot$, Bruzual and Charlot, 2003). One possible explanation is that a significant fraction of the ionizing photons (roughly half) is escaping from low-mass galaxies in the peak of their burst phase, resulting in lower observed $L_{H\alpha}$. Such a high escape fraction has only been observed in a handful of galaxies with extreme star formation surface densities and specific star formation rates (Izotov et al., 2018; Vanzella et al., 2016, 2018), unlike the more typical galaxies in our sample. However, we note that the escape fraction has not been probed in galaxies with such low star formation rates ($SFR < 0.1$ $M_\odot$ yr^{-1}), as the Lyman continuum flux would be difficult to detect with current instrumentation. There has been an indirect search for escaping ionizing photons (via a deep search for faint Hα recombination in the nearby circumgalactic medium of three nearby dwarf galaxies. But there was only 5% more $L_{H\alpha}$ emission identified (Lee et al.,

2016). This still leaves open the possibility that the ionizing photons may escape to a much larger radius (> 2 kpc). The possibility that typical low mass galaxies have high ionizing photon escape fractions is intriguing and has important implications for reionization and the subsequent evolution of the ionizing background.

Another possible explanation is that the high mass end of the IMF is not being fully sampled, creating a deficit of the most massive stars and suppressing $L_{H\alpha}$. However, in Figure 2.10, we can see that modeling of the stochastic sampling of the IMF still produces a large number of galaxies above the observed distribution of $\log(L_{H\alpha}/L_{UV})$ at all masses. Therefore, it appears that IMF sampling can not fully explain the discrepancy.

2.6.4 Dust Attenuation

We caution that the $\log(L_{H\alpha}/L_{UV})$ measurements contain potential systematic uncertainties arising from the application of a uniform dust attenuation curve. We know that even galaxies with similar masses and star formation histories show considerable scatter in their extinction curves (Meurer et al., 1999). This will increase the scatter in the $\log(L_{H\alpha}/L_{UV})$ vs. $\Delta\log(L_{H\alpha})$ plane, but does not significantly affect our interpretation, as it ultimately depends on the slope of the distribution in that plane. In addition, there is some evidence that attenuation curves may change as a function of stellar mass and/or SFR (Reddy et al., 2015). If the variations in attenuation curves are a function of stellar mass, this will not affect our results, as we have binned our data in narrow stellar mass ranges. However, if the attenuation curves change as a function of SFR, then this would change the relative attenuation of L_{UV} and $L_{H\alpha}$ *within a stellar mass bin*, which could change the slope of the distribution in the $\log(L_{H\alpha}/L_{UV})$ vs. $\Delta\log(L_{H\alpha})$ plane.

2.7 Summary

In this paper we studied the phenomenon of bursty star formation in low-redshift dwarf galaxies and attempted to determine the parameters (amplitudes and timescales) of the bursts. The parameters can be measured by comparing star formation rate indicators (e.g., $L_{H\alpha}$ and L_{UV}) that are sensitive to different timescales. For our analyses, we used the data from Weisz et al. (2012a), which includes extinction-corrected $L_{H\alpha}$ and L_{UV} measurements for local galaxies with a large range in stellar mass ($10^6 < M_* < 10^{10} M_\odot$).

First, we fit to the same top-hat periodic burst model of Weisz et al. (2012a) to determine the period, duration, and amplitude of the bursts. We improved the analysis by 1) using more appropriate sub-solar stellar metallicities, 2) expanding the probed parameter space and 3) using a likelihood analysis to better determine parameter uncertainties and degeneracies. We found that the results were broadly similar to those of Weisz et al. (2012a), but with significantly longer durations and periods. Moreover, we found that the parameters had significant uncertainties and degeneracies, with period and duration being highly degenerate. We therefore argued that it is not sufficient to use only a single $\log(L_{H\alpha}/L_{UV})$ distribution to constrain a three-parameter burst model.

We showed that a galaxy's location on the star-forming main sequence is correlated with the $\log(L_{H\alpha}/L_{UV})$ distribution, strongly suggesting that all of the galaxies are exhibiting similar star formation histories. Thus, we argue that the $\Delta\log(L_{H\alpha})$ distribution (i.e., the $\log(L_{H\alpha})$ deviation from the mean $\log(L_{H\alpha})$ should be used to estimate burst parameters, in addition to the $\log(L_{H\alpha}/L_{UV})$ distribution. Indeed, the two parameters are correlated, and the motion of galaxies in the 2-dimensional $\log(L_{H\alpha}/L_{UV})$-$\Delta\log(L_{H\alpha})$ plane

gives significant insight into the timescale for variations in the star formation rate.

In order to avoid highly parameterized star formation histories, we look for a model with the least numbers of parameters that informs us most about the physical characteristics of the bursts. So we instead compare to exponential bursts with two parameters: 1) the time scale of rising and falling of the SFR (e-folding time, τ) and the maximum amplitude of the bursts (A). We find that galaxies with stellar masses less than $10^{7.5} M_{\odot}$ undergo large and rapid changes in SFR with timescales of $\tau < 30$ Myr and maximum amplitudes of $A \sim 100$ while galaxies more massive than $10^{8.5}$ $M_{\odot}$ experience smaller, slower changes in SFR with $\tau > 300$ Myr and $A \sim 10$.

We also calculated the $\log(L_{H\alpha}/L_{UV})$-$\Delta\log(L_{H\alpha})$ relation for galaxies in the FIRE-2 hydrodynamical simulations and found that these galaxies exhibit short timescale ($\tau < 30 Myr$) changes in SF at all mass ranges. Though the amplitudes of these bursts agree well with the observed $\Delta\log(L_{H\alpha})$distributions, such short bursts are different from the long timescales of $\tau > 100 Myr$ that we inferred for galaxies above $10^8 M_{\odot}$. Future improvements to the simulations should look carefully at what is causing such short bursts in the more massive galaxies ($M_* 10^8 M_{\odot}$).

Furthermore, we examined the stochastic IMF sampling models using the SLUG code (da Silva et al., 2014) and found that the simulated $\log(L_{H\alpha}/L_{UV})$-$\Delta\log(L_{H\alpha})$distributions were significantly steeper than the observed distributions. Therefore, stochastic sampling of the IMF may help explain some of the scatter in $\log(L_{H\alpha}/L_{UV})$-$\Delta\log(L_{H\alpha})$, but the assumptions of the mass function of the clusters or stars may need to be revised.

Finally, we note that measurements of L_{UV} already exist for large samples of

galaxies from $z \sim 1$ up to the earliest epochs ($z \sim 8$). Soon, with the advent of JWST, WFIRST and the next generation of 30-meter-class ground-based telescopes, measurements of $L_{H\alpha}$ will be routine, even for dwarf galaxies at high redshift. As galaxies at early epochs will have very different conditions (smaller physical sizes, higher gas fractions, more metal-poor stars), it will be necessary to use a similar analysis to determine the properties of bursty star formation at high redshift. This will in turn allow us to better interpret these observables to more accurately determine physical properties.

2.8 Appendix

2.8.1 Details of determining SF model parameters based on $\log(L_{H\alpha}/L_{UV})$ distribution

We first describe the Weisz et al. (2012a) method of constraining burst parameters, and then explain our improvements to the method.

Weisz et al. (2012a) divided their observed sample into five stellar mass bins from 10^6 to $10^{11} M_\odot$ and assumed that all galaxies of similar stellar masses have star formation histories with the same parameters. They defined their SF models as top-hat, periodic bursts superimposed on a constant, baseline SFR and assumed stellar metallicity of $1 Z_\odot$. They then determined the $\log(L_{H\alpha}/L_{UV})$ distribution from models with different burst periods (P), durations (D), and amplitudes (A) and used a Kolmogorov-Smirnov test to identify the parameters that best reproduce the observed $\log(L_{H\alpha}/L_{UV})$ distribution in each mass bin. W12 finely sampled the parameter space, resulting in 1466 SFH models. The main conclusion of W12 is that galaxies with the lowest stellar masses have higher amplitude

bursts (A $\sim 30\times$ the baseline rate), relatively long durations (D $\sim 30 - 40$ Myr), and long periods ($P = 250$ Myr). The highest mass bins are characterized by almost constant SFRs with an occasional modest burst favoring SF models with short duration (D ~ 6 Myr) and modest amplitudes (A ~ 10).

We use the same periodic, top-hat burst model as Weisz et al. (2012a), with the same parameters (P, D, A). The duration is restricted to be less than the period. We note that the value of the baseline SFR is irrelevant, as the relevant factor affecting luminosity *ratios* is the ratio of the amplitude SFR to the baseline SFR. From observations, we have a sample of $\log(L_{H\alpha}/L_{UV})$ for 185 local galaxies ranging from $5 < log(M_*[M_\odot]) < 11$ in mass. The observed sample is classified into six mass bins.

For each individual set of model parameters, we build a sample of 10,000 $\log(L_{H\alpha}/L_{UV})$ values for that SFH, selected in $5Myr$ time intervals. This is a way of representing an ensemble of galaxies in the real world that are caught during different stages of the star formation history assuming that they all share the same SFH. We do not sample the first 200 Myrs of star formation, to ensure that the L_{UV} is not biased low as it would not have enough time to build up a full sample of A-stars. To do this, we first calculate the spectral energy distribution (SED) as a function of time for a single stellar population (Bruzual and Charlot, 2003) using a Chabrier IMF (Chabrier, 2003), Padova isochrones (Bertelli et al., 1994; Bressan et al., 1993; Fagotto et al., 1994), and a constant stellar metallicity. For each output SED, we calculate L_{UV} as the average of the continuum between 1460-1540 Å and $L_{H\alpha}$ by determining the Hydrogen-ionizing photon production rate and assuming case B recombination. We then convolve our $L_{UV}(t)$ and $L_{H\alpha}(t)$ curves with the $SFR(t)$ curves

to determine the *intrinsic* (unobscured by dust) $\log(L_{H\alpha}/L_{UV})$ as a function of time.

To take into account the observational uncertainties, we add 10-20% Gaussian errors to L_{UV} and $L_{H\alpha}$ due to statistical uncertainties arising from dust attenuation corrections (See section 2.5.1.)

Finally, we determine the probability of obtaining our measured distribution of $\log(L_{H\alpha}/L_{UV})$ given the modeled distribution for the set of parameters (D, P, A). We then determine the set of parameters that maximizes the probability space and marginalize them to determine the 1-D posteriors distributions for each individual parameter.

Stellar Mass $log(\frac{M}{M_\odot})$	Measured Z_a $[Z_\odot]$	Model Z_b $[Z_\odot]$
≤ 7	N/A	0.2
$7 - 7.5$	$N/A - 0.10$	0.2
$7.5 - 8$	$0.10 - 0.17$	0.4
$8 - 8.5$	$0.17 - 0.31$	0.4
$8.5 - 9$	$0.31 - 0.46$	0.4
$9 - 10$	$0.46 - 0.70$	0.4

Table 2.2: Stellar metallicities used in models. Z_a is the measured gas-phase metallicity for each stellar mass bin in Andrews and Martini (2013)and Z_b is the Closest stellar metallicity model in Bruzual and Charlot (2003). Note that we use $0.4Z_\odot$ for $\log(M_*) = 7.5-8$ (instead of 0.2 $Z_\odot$) in order to fit the observed $\log(L_{H\alpha}/L_{UV})$ distribution.

In order to select the appropriate metallicity for each stellar mass bin, we refer to the mass-metallicity relation from Andrews and Martini (2013), assuming solar Oxygen abundance to be 8.86. In Table 2.2, the approximate metallicity of each mass bin is determined except for the lowest mass bin due to lack of data points in this mass range. We choose to use the metallicities from the existing libraries in Bruzual and Charlot (2003)

that are closest to the values in column 2 of Table 2.2. The chosen metallicities are given in column 3. For $M \leq 10^7\ M_\odot$ we assumed 0.2 solar metallicity because the next smallest metallicity available in the BC03 is 0.02 $Z_\odot$, far lower than we expect for galaxies at those stellar masses. The results of this model is discussed in sec. 3.3.

2.8.2 Improvements On Fits To Periodic SF History

As discussed above, the W12 study made significant progress in fitting to the $log(\frac{L_{H\alpha}}{L_{UV}})$ distribution to determine SF burst model parameters. However, we have identified ways in which we can enhance the W12 analysis.

First, the stellar metallicity was assumed to be solar for all mass ranges. This can change the estimated SF model parameters because stellar metallicity affects the surface temperature of stars such that more metal-rich stars are cooler at a given mass. This therefore affects the amount of ionizing to non-ionizing photons. To address that, we explore the effects of using more realistic (lower) stellar metallicities on parameter estimation for different mass ranges based on the metallicities estimated in Andrews and Martini (2013) (see Table 2.2).

Second, in order to explore the model parameter space, W12 used a two-sided K-S (Kolmogrov-Schmirnov) test. However, we use likelihood approach that allows us to better determine parameter uncertainties and degeneracies.

Third, the best-fit parameters from W12 were at the edge of the explored parameter space, so it is possible that the actual best-fit parameters are out of the explored range. Therefore, we expanded the parameter space (by a factor of five in duration, period, and amplitude) in order to guarantee that we explore all parameter space far enough that

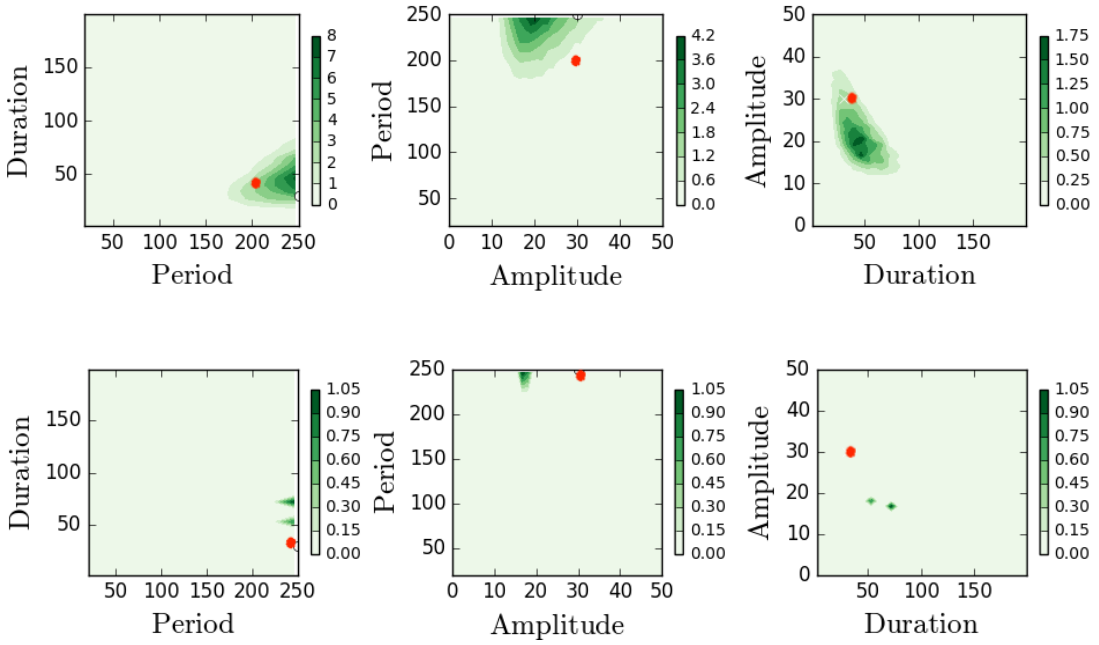

Figure 2.11: 2D contour plots of (D,P), (P,A) and (A, D) from left to right. Parameter space is limited to the W12 range, i.e. $D \leq 200$, $P \leq 250$, $A < 50$ and assuming stellar metallicity of $1Z_{\odot}$. Top and bottom subplots are contour plots of $M \leq 10^7\ M_{\odot}$ and $10^7 < M \leq 10^8\ M_{\odot}$ respectively. The maximum likelihood values are in good agreements with the W12 predictions, shown as red circles.

encompasses the best-fit parameter.

2.8.3 Results of Best Fit Burst Parameters

We first test our method by comparing our analysis with that of W12 to see whether we produce the same best-fit values. To do so, we make the same assumptions as W12 (assuming solar metallicity and identical parameter space). Figure 2.11 shows the contours of the burst parameters for the two lowest mass ranges in W12, i.e. $M \leq 10^7\ M_{\odot}$ and $10^7 < M \leq 10^8\ M_{\odot}$.

As can be seen in Figure 2.11, the best-fit parameters are in agreement with W12. They report (D, P, A) of (40, 200, 30) and (30, 250, 30) for $M \leq 10^7\ M_\odot$ and $10^7 < M \leq 10^8\ M_\odot$ respectively which is comparable to our results; (46, 250, 20) (Figure 2.11, top) and (53, 250, 18) (Figure 2.11, bottom). The slight discrepancy in the duration and amplitude between our method and W12 arises from the different sampling of the parameter space. This confirms the credibility of our maximum likelihood approach for determining the best-fit parameters of bursts. The results and the interpretations are discussed in section 2.4.

Chapter 3

The ionizing photon production efficiency (ξ_{ion}) of lensed dwarf galaxies at $1 \leq z \leq 3$

3.1 Abstract

We measure the ionizing photon production efficiency (ξ_{ion}) for a sample of faint low-mass galaxies ($10^{6.5}$-10^{10} $M_{\odot}$) at an intermediate redshift of $1< z <3$ by taking advantage of gravitational lensing from three foreground lensing clusters (Abell 1689, MACS J0717, and MACS J1149). This helps us constrain ξ_{ion} as one of the key components in determining the ionizing emissivity of these low mass galaxies and ultimately their role in the cosmic reionization. We utilize Keck/MOSFIRE rest-optical spectra to measure nebular emission fluxes and HST rest-UV and rest-optical imaging to measure the photometry.

We correct Hα fluxes for dust attenuation using the Balmer decrement. We present two ways of flux stacking. First, we take the average of the log(Hα/UV) luminosities in order to determine the typical Log(ξ_{ion}). Second, we take the log of total Hα over total UV_{1500} luminosities. We favor the latter as it provides the total ionizing UV luminosity density once it is multiplied by the total non-ionizing UV (UV_{1500}) luminosity density inferred from the UV luminosity function. Log(ξ_{ion}) inferred from the second method is $\sim$ 0.2 dex higher than the first method in our sample. We do not find any strong dependence between the log(ξ_{ion}) and M_{UV} or UV spectral slope (β) and report a value of log(ξ_{ion})= 25.5-25.6 for $-21 < M_{UV} < -18$. We also find a correlation between log(ξ_{ion}) and the equivalent widths of Hα and [OIII] that may suggest that these equivalent widths can be a proxy for the ξ_{ion} estimate when the direct measurements of non-ionizing UV flux is not available.

3.2 Introduction

Many studies have demonstrated that by $z \sim 6$ the neutral hydrogen in the intergalactic medium (IGM) was fully ionized. What is not well understood is what are the sources that ionized the universe and provided the intergalactic medium thereafter. In fact, it is not clear whether the galaxies that we have detected at high redshift are capable of ionizing the IGM. In order to determine this, we need to know the rate of ionizing photons emitted into the IGM as a function of redshift (often referred to as $\Gamma(z)$). In order to calculate $\Gamma(z)$, three quantities must be known.

$$\Gamma = \int L\Phi(L)\xi_{ion}(L)f_{esc}(L)dL \tag{3.1}$$

The first quantity is the luminosity function of galaxies ($\Phi(L)$), which is typically measured in the non-ionizing ultraviolet (UV), as it is relatively easy to detect galaxies at those wavelengths at high redshift. If the UV luminosity function is integrated, it gives the total UV luminosity density at a given redshift. The second quantity that is needed is a conversion from the non-ionizing UV luminosity density to ionizing UV luminosity density. This conversion is often referred to as ξ_{ion} and is defined as the rate of ionizing photon production normalized by the non-ionizing UV luminosity density (in f_ν). The third necessary quantity is the fraction of ionizing photons that escape into the intergalactic medium, referred to as the escape fraction, f_{esc}. Of course, all of these quantities, can vary with luminosity.

Many studies have constrained the luminosity functions of high redshift galaxies. Here we are interested in constraining the second quantity, ξ_{ion}. The primary way of determining ξ_{ion} is to directly measure the ionizing UV flux (blue-ward of 912 $\mathring{A}$). However achieving this is difficult due to the lack of deep rest-UV spectroscopy at high redshifts and is limited to either a few individual galaxies or the composite spectrum of a large number of galaxies (Reddy et al., 2016). The alternative way is to infer the ionizing UV flux from the Hydrogen recombination lines (e.g., $H\alpha$ or $H\beta$) assuming that the interstellar medium (ISM) is optically thick to ionizing photons and do not allow them to escape the galaxy. In this case, the rate of ionizations and, thus, the ionizing photon production rate, can be inferred from recombination lines assuming case-B recombination. As such, Bouwens et al. (2016a); Nakajima et al. (2016); Matthee et al. (2017); Shivaei et al. (2017) evaluated ξ_{ion} as the ratio of hydrogen recombination lines to 1500 $\mathring{A}$ UV (UV_{1500}) fluxes. Another

indirect way of inferring the ξ_{ion} is to implement metal nebular emission lines into the photoionization models and characterize the shape of the ionizing spectrum (Stark et al., 2015, 2017).

However, all these studies obtain ξ_{ion} for a selected sample of high-redshift galaxies which are exclusively luminous Hα or Lyman α emitters or have extreme emission lines. As such there aren't many measurements of ξ_{ion} in low-luminosity low-mass galaxies (Lam et al., 2019).

On the other hand, recent studies suggest that low-mass galaxies should have a greater contribution in the reionization owing to a steep faint end slope of 1500A UV luminosity function observed in high redshift galaxies (Reddy and Steidel, 2009; Bouwens et al., 2012; Alavi et al., 2014; Finkelstein et al., 2015; Kriek et al., 2015; Atek et al., 2015; Livermore et al., 2017). Additional supporting evidence is that at low mass systems, more ionizing photons are thought to escape from the galaxies into the IGM (Paardekooper et al., 2013; Wise et al., 2014; Erb, 2015; Anderson et al., 2017; Henry et al., 2015; Karman et al., 2017) at high redshifts. In order to claim that low mass galaxies are the primary reionizing agents, we still need to investigate the ionizing photon production efficiency (ξ_{ion}) of these low mass galaxies relative to their massive counterparts and see if there is any enhancement in the ξ_{ion} value towards lower masses. However, despite its great importance, little is known about ξ_{ion} in faint low mass systems.

In this paper we measure ξ_{ion} for low-mass ($6.5 \leq log(M_*) < 10$) low-luminosity galaxies at z between $1.0 - 3.35$, which has not been done before. These galaxies are highly magnified by gravitational lensing by foreground galaxy clusters. The magnification enables

us to detect low luminosity galaxies, up to an intrinsic UV magnitude of -15. We quantify ξ_{ion} using $H\alpha$ recombination emission and non-ionizing (1500 $\mathring{A}$) UV fluxes from deep MOSFIRE/Keck spectroscopy and HST imaging. We also have $H\beta$ detections for most of the galaxies in our sample in order to quantify dust extinction via the Balmer decrement.

However, due to the stochastic nature of the star formation rates in low mass galaxies, there is always an intrinsic scatter in the ratio of $H\alpha$ (or $H\beta$) to UV at low mass (Lee et al., 2009; Weisz et al., 2012b; Domínguez et al., 2015; Guo et al., 2016b; Emami et al., 2018). As a result, we expect to see the same scatter in the ξ_{ion} distribution which makes it crucial to come up with an appropriate way of combining the galaxies' fluxes and derive a single ξ_{ion} value that properly represents the entire sample. Here we also address this issue and introduce a new way of stacking $H\alpha$ and UV fluxes that deals with the ξ_{ion} scatter at low mass galaxies.

Furthermore, since ξ_{ion} is relevant to the ionizing radiation intensity of the galaxies, it can also be inferred from other physical quantities that are also dependent on the ionizing radiation intensity, such as UV spectral slope (Robertson et al., 2013; Bouwens et al., 2015b; Duncan and Conselice, 2015a) and equivalent widths of nebular UV and optical lines (Stark et al., 2015, 2017; Chevallard et al., 2018; Tang et al., 2018). We also investigate the relationship between ξ_{ion} and these physical quantities in our sample and see if those relations shown by previous works further extend to the lower mass low luminosity regimes or not.

The outline of the paper is as follows. We describe the sample selection and data acquisition in § 3.3. In § 3.4 we present flux measurements and discuss the sample com-

pleteness. In § 3.5 we describe two approaches of stacking fluxes and discuss the relevance of each for the ξ_{ion} determination. In § 3.6 we show our results and compare them with previous works. We discuss the relationship between ξ_{ion} and other physical quantities in § 3.7. Lastly, we conclude with a brief summary in § 3.9. We assume a Λ-dominated flat Universe with $\Omega_\Lambda = 0.7$, $\Omega_M = 0.3$ and $H_0 = 70$ km s^{-1} Mpc^{-1}. All magnitudes in this paper are in the AB system (Oke and Gunn, 1983) and all equivalent widths are quoted in the rest-frame.

3.3 data

3.3.1 HST Data

Our sample is drawn from *Hubble Space Telescope* (HST) survey (Alavi et al., 2016) that identifies faint star-forming galaxies at $1 < z < 3$ behind three lensing clusters – Abell 1689 and two Hubble Frontier Fields (HFF) clusters, MACS J0717 and MACS J1149. The data reduction and photometric measurements are discussed in detail in Alavi et al. (2016). For galaxies in Abell 1689, we measure flux in eight photometric bands spanning the observed near-UV and optical. For galaxies in MACS J0717 and MACS J1149 we measure flux in nine photometric bands spanning the observed near-UV, optical, and near-IR. The near-UV data (program IDs 12201, 12931, 13389) allow for efficient identification of the Lyman break, enabling accurate photometric redshifts at $1 < z < 3$.

We require a lens model for each cluster to correct for the lensing magnification and derive the intrinsic galaxy properties. As discussed in Alavi et al. (2016), for Abell 1689 we use the lens model of Limousin et al. (2007) and for the HFF clusters we use the

models from CATS[1] team with Jauzac et al. (2016) and Limousin et al. (2016) for MACS J1149 and MACS J0717, respectively.

3.3.2 Spectroscopic Sample and Data Reduction

We briefly summarize our spectroscopic selection and data reduction here, but for more details see Alavi et al., in prep. From the photometric survey discussed above, we select our spectroscopic sample such that the bright rest-frame optical nebular emission lines fall within the atmospheric windows at $1.37 < z < 1.70$, $2.09 < z < 2.61$ and $2.95 < z < 3.8$. When selecting targets, we prioritized galaxies with high magnification and brighter observed optical flux densities. The data were collected between January 2014 and March 2017. Masks were made for the $1.37 < z < 1.70$ and $2.09 < z < 2.61$ redshift ranges and all of the strong optical emission lines (Hα, [NII], [OIII], Hβ, and [OII]) were targeted. For the lower redshift mask, Y-, J-, and H-band spectroscopy was obtained. For the higher redshift mask, J-, H-, and K-band spectroscopy was obtained. The total exposure times for each mask and filter range from 48 to 120 minutes.

The MOSFIRE data were reduced using the MOSFIRE Data Reduction Pipeline[2](DRP). The DRP produces a 2D flat-fielded, sky-subtracted, wavelength-calibrated, and rectified spectrum for each slit. It also combines the spectra taken at each nod position (we used an ABBA dither pattern). The wavelength calibration for the J- and H-band spectra was performed using the skylines and for the Y- and K-band spectra a combination of skylines and Neon lines was used. We then utilize custom IDL software, BMEP [3], from Freeman

[1]https://archive.stsci.edu/prepds/frontier/lensmodels/
[2]https://keck-datareductionpipelines.github.io/MosfireDRP/
[3]https://github.com/billfreeman44/bmep

et al. (2017) for the 1D extraction of spectra. The flux calibration is done in two stages. First, we use a standard star with spectral type ranging from B9 V to A2 V, which has been observed at similar airmass as the mask. We then do an absolute flux calibration using a slit star included on each mask.

The spectrum in each filter was fit with the Markov Chain Monte Carlo (MCMC) Ensemble sampler, `emcee`[4] (Foreman-Mackey et al., 2013). Emission lines were fit with single-Gaussian profiles, and the continuum was fit with a straight line. The emission-line width and redshift were set as free parameters when fitting in a given filter, with the final spectroscopic redshift of a galaxy determined by the weighted average of the different best-fit redshifts, when necessary. In the instances where [O3]λ5007 fell outside our spectroscopic coverage, we determined its flux with the [O3]λ4959 line and the intrinsic flux ratio between the two lines of the doublet: [O3]λ5007/[O3]λ4959 = 2.98 (Storey and Zeippen, 2000). More details about the spectroscopic line measurements can be found in Gburek et al. (2019).

3.3.3 Sample Selections

There are 60 objects in our sample for which we have sufficient HST filter coverage spanning the observed near-UV to near-IR that enables a robust SED fit and, thus, reliable estimates of stellar properties (stellar mass, V band dust attenuation (A_V), UV spectral slope (β), etc.). We remove some of these objects from sample for the following reasons:

Non-covered Hα or large Hα errors: We remove 19 galaxies due to either the fact that their Hα are not covered by MOSFIRE filters or their Hα flux errors are greater than 10^{-17} erg s^{-1} cm^{-2}. We choose to impose a flux error cutoff rather than the signal-to-noise cutoff

[4]https://emcee.readthedocs.io/en/v2.2.1/

on our Hα measurement. This way we can discriminate against those whose Hα lines fall on the sky lines and happen to have moderate signal-to-noise with large Hα fluxes and large errors.

Galaxies with high magnification: If a galaxy has a high average magnification, it means it is sitting close to the caustic in the source plane. Thus, the gradient of magnification is large and the magnification varies considerably across the galaxy. This could result in a significant altering in the true ratio of $L_{H\alpha}$ to L_{UV}. Not only would this increase the scatter, but it can result in a bias, as the galaxies are selected via rest-frame UV continuum luminosity density. Hence, we remove seven galaxies whose magnifications (μ) are $\mu > 30$ in A1689 and $\mu > 15$ in HFF clusters

Multiply imaged galaxies We remove multiple images of two galaxies to avoid double counting. In these cases, we keep the most highly magnified image in the sample unless the magnification is very large (> 30 in A1689 and > 15 in HFF clusters). In which case, we use the next brightest image. These multiple images were identified using Lenstool (Limousin et al., 2016; Alavi et al., 2016).

High slit loss galaxies: For larger, extended galaxies, the slit loss correction can be large, and the MOSFIRE measurement will only be sampling a small, possibly unrepresentative portion of the whole galaxy. As such, we remove four galaxies with $H\alpha$ slit losses $> 70\%$ from the sample.

Low confidence spectroscopy measurements: We also take out one galaxy from the sample for which we are not confident about its line measurements.

Finally we are left with 31 galaxies in the sample that are free of the aforementioned

concerns.

3.4 Measurements

3.4.1 SED Fitting

Stellar masses, star formation rates and stellar dust attenuation for our galaxies are estimated with SED fits to the photometry (see Alavi et al., in prep, for full description). Specifically, for the Abell 1689 cluster, we use eight broad-band filters spanning the observed near-UV to optical in the F225W, F275W, F336W, F475W, F625W, F775W, F814W and F850LP filters. In addition, we used the photometry in two near-IR HST bands (F125W and F160W), though the imaging does not cover the full area covered by the near-UV and optical imaging.

For the two HFF clusters, we fit to nine broad-band filters spanning the observed near-UV to near-IR in the F275W, F336W, F435w, F606W, F814W, F105W, F125W, F1140 and F160W filters.

We use the stellar population fitting code FAST (Kriek et al., 2009), with the BC03 (Bruzual and Charlot, 2003) population synthesis models, and assume an exponentially increasing star formation history with a Chabrier IMF (Chabrier, 2003). As suggested by Reddy et al. (2018) for high-redshift low-mass galaxies, we use the SMC dust extinction curve with A_V values varying between $0.0 - 3.0$. We leave the metallicity as a free parameter between [0.4-0.8] $Z_\odot$. The age and star formation timescales can vary between $7.0 < \log(t)$ [yr] < 10 and $8.0 < \log(\tau)$ [yr] < 11.0, respectively. The redshifts are fixed to the values obtained spectroscopically. The 1σ confidence intervals are derived from a

Monte Carlo method of perturbing the broad-band photometry within the corresponding photometric uncertainties and refitting the SED 300 times. We note that we correct the broadband photometry for the contamination from the nebular emission lines using the line fluxes measured from the MOSFIRE spectra.

3.4.2 Slit Loss Correction

The emission line fluxes need to be corrected for slit losses. This procedure is more important for extended or stretched (highly magnified) objects as the slit may not fully cover the object. This needs to be done for each object in each MOSFIRE band and each mask. We adopt the following procedures: 1. We cut a $30'' \times 30''$ postage stamp centered on the galaxy from the F625w as this filter gives a high S/N image of the rest-frame ultraviolet light, and therefore the approximate morphology of the star-forming regions. 2. We identify the pixels corresponding to the object using the segmentation map output by SourceExtractor (Bertin and Arnouts, 1996b). 3. We mask out all pixels of the nearby objects and background from the postage stamp and replace them with zero flux. 4. The sum of the total flux of pixels belonging to the object gives us the actual flux that SourceExtractor measured. 5. We smooth the postage stamp applying a Gaussian Kernel with a FWHM that is given by

$$FWHM^2_{kernel} = FWHM^2_{seeing} - FWHM^2_{F625W} \tag{3.2}$$

$FWHM^2_{seeing}$ is the FWHM of the Gaussian fit to the profile of the slit star in the corresponding mask and filter. $FWHM^2_{F625W}$ is FWHM of the F625W PSF ($0.1''$). This

artificially degrades the resolution of the HST image to the same spatial resolution as the MOSFIRE observation. 6. We overlay the slit on the postage stamp of the smoothed image using its position angle, center, length and width and block out regions of the object that falls out of the slit. 7. The sum of the flux of the remaining pixels is the flux that one could measure from MOSFIRE if the F625w filter was used. 8. Now, the ratio of the in-slit flux from 7 to the total flux from 4 indicates how much flux of the galaxy remains after slit losses.

3.4.3 Non Dust-Corrected ξ_{ion}

The goal of this paper is to measure the ionizing photon production efficiency of galaxies (ξ_{ion}) for our sample which represents the rate of Lyman continuum photons per unit UV_{1500} luminosity (Robertson et al., 2013; Bouwens et al., 2016a) as:

$$\xi_{ion} = \frac{Q_{H^0}}{L_{UV}} \; [sec^{-1}/erg \; sec^{-1} \; Hz^{-1}] \tag{3.3}$$

where L_{UV} is the intrinsic UV-continuum luminosity density (per unit frequency) around 1500 Å. Based on the stellar synthesis models (Leitherer et al., 1995), the rate of production of ionizing photons (Q_{H^0}) can be determined from the hydrogen recombination lines, in this case, $H\alpha$ as

$$L_{H\alpha}[erg \; s^{-1}] = 1.36 \times 10^{-12} \; Q_{H^0}[s^{-1}] \tag{3.4}$$

where $L_{H\alpha}$ is the $H\alpha$ luminosity. Here we assume that all ionizing photons are converted into case B recombination emission and none are escaped into the intergalactic

medium. We also obtain the stellar mass estimates from the SED fits that was explained in 3.4.1.

Figure 3.1 shows the $\log(\xi_{ion})$ as a function of stellar mass for the observed $L_{H\alpha}$ and L_{UV}.

Considering that low-mass galaxies are less attenuated by the dust (Pannella et al., 2009; Reddy et al., 2010; Bouwens et al., 2016b), we assume that the overall position of these galaxies would mildly be different from when they are not dust attenuated. Based on this assumption and Figure 3.1, we find our galaxies lying roughly above the canonical value of 25.2 (Robertson et al., 2013).

We also examine to see to what flux limit $H\alpha$ can be faint in order to be still detectable via MOSFIRE for a galaxy with a typical magnification of our sample. If MOSFIRE detection limit is F_{lim} and galaxy's magnification is μ, galaxy can then be as faint as F_{lim}/μ to still be detectable in our experiment. Thus we can determine the corresponding ξ_{ion} of this critical $H\alpha$ flux as a function of mass if we divide this critical $H\alpha$ luminosity by UV luminosity at any given mass. The UV luminosity at any mass is estimated from the linear fit through the log (L_{UV})-log(mass) relation. Note that we only fit to masses above $10^{7.5}$ $M_{\odot}$ in order to ensure that we are not biased to only bright L_{UV} galaxies at $M_* < 10^{7.5}$ which . We demonstrate these log (ξ_{ion}) thresholds for three magnifications of 3,10 and 30 as dashed diagonal lines in Figure 3.1, indicating the detection limit below which galaxies are intrinsically too faint to be detected without the lensing effect. The typical magnification of galaxies in our sample is between 3 to 7 which corresponds to an area between the green and red diagonal lines. Based on this, as we move towards lower

masses we start missing more galaxies with low $\log(\xi_{ion})$ whose $H\alpha$ fluxes are fainter than MOSFIRE detection limit. This makes us to put a completeness limit at $M_* = 10^8$ $M_\odot$ to our sample above which we are confident that we are not missing a significant subsample of low $\log(\xi_{ion})$ galaxies.

Overall, we note that $\log(\xi_{ion})$ spans about 1.5 dex across the sample (24.8-26.3), as is evident in Figure 3.1.

3.4.4 Dust Extinction Correction

We use the SMC (Gordon et al., 2003) extinction curve to correct for dust attenuation of the UV luminosity density, as it has been shown to be more broadly consistent for low-mass galaxies at high-redshift (Bouwens et al., 2016a; Reddy et al., 2018). We use the Balmer decrement ($L_{H\alpha}/L_{H\beta}$) to determine the $L_{H\alpha}$ attenuation assuming a Cardelli extinction curve (Cardelli et al., 1989).

3.5 Two Approaches of flux Stacking for ξ_{ion} estimates

Here we attempt to evaluate the representative $\log(\xi_{ion})$ value of our sample. For this, we need to stack the dust-corrected $H\alpha$ and UV fluxes of individual galaxies. However, we note that the spread in $\log(\xi_{ion})$ is large ($\sim$ 1.5 dex) and real, as it is far larger than the error bars. Given such a large spread *in the logarithm* of ξ_{ion}, we need to be careful about how we stack, depending upon the question we are trying to answer.

There are two ξ_{ion} values that we are interested in obtaining. First, we are interested in the properties of the *typical* galaxy, which can simply be obtained via the median,

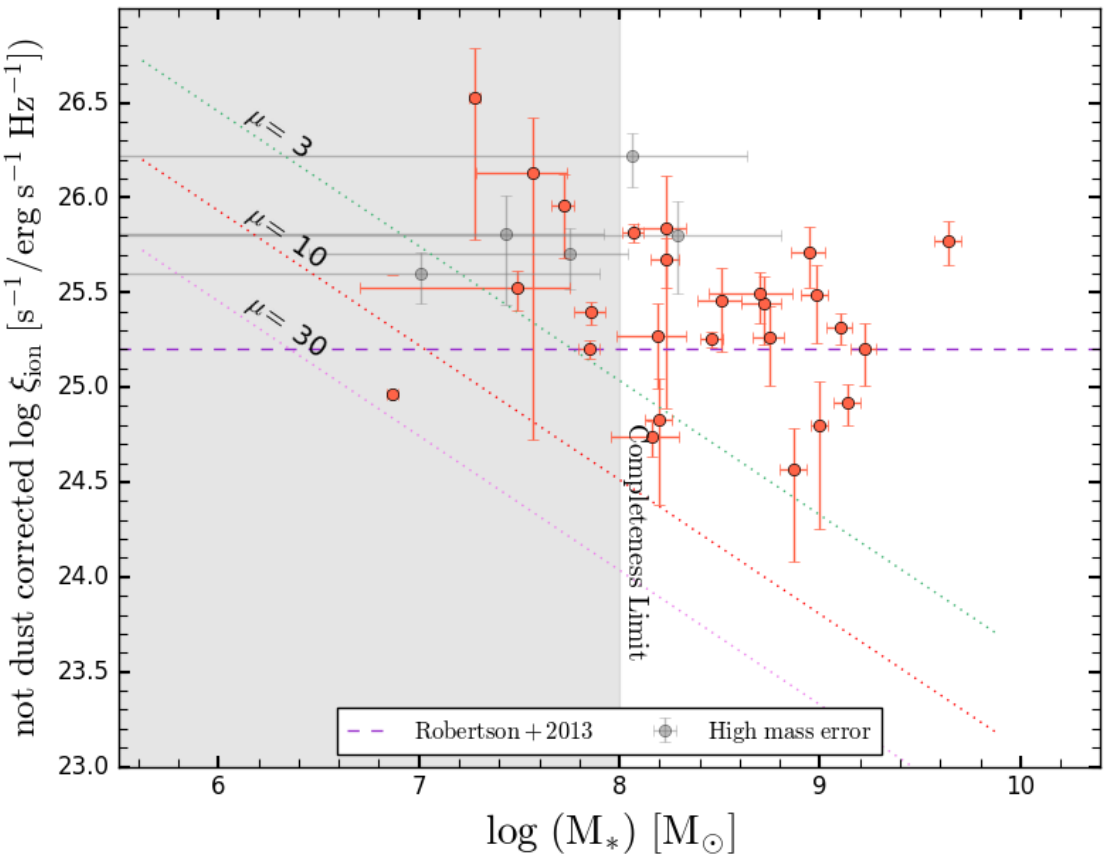

Figure 3.1: Not dust-corrected log(ξ_{ion}) as a function of log (stellar mass) derived from the observed $L_{H\alpha}$ and L_{UV}. The gray points show galaxies with high mass errors. The green, red and magenta diagonal dotted lines indicate the typical log(ξ_{ion}) detection limit for three magnification factors of 3,10 and 30 respectively, below which galaxies are intrinsically too faint to be detected through MOSFIRE. $10^8 M_\odot$ is the mass limit below which faint galaxies are being missing from the sample and sample becomes incomplete (gray region). Thus we only perform stacking on galaxies above this mass limit. The horizontal dashed line refers to the log(ξ_{ion}) canonical value of 25.2 from Robertson et al. (2013). The overall sample lies around and above this canonical value.

or the average of a symmetric distribution. Second, we are also interested in the total contribution of these galaxies to reionization, in which case we are interested in the *total* Hα luminosity of all galaxies divided by the total L_{UV} of all galaxies. Such a number allows a direct conversion from UV luminosity functions to ionizing photon production rate densities. The stack in this case is *not* the average of the $\log(\xi_{ion})$ values that many have calculated before, since the luminous objects will dominate the signal.

In the following we provide the details of our two stacking procedures. In the first method we determine the average (or mean) of $\log(\xi_{ion})$ or, specifically, the average of the dust-corrected log(Hα/UV) fluxes. In order to get the uncertainty in the average of $\log(\xi_{ion})$, we use bootstrap resampling method, in which case, for a data sample of size N, we draw N random values from the original sample and form a new sample of the same size and calculate its average. By repeating this 100000 times, we build the distribution of the averages and calculate the 68% confidence interval of this distribution as the uncertainty in the average of $\log(\xi_{ion})$. We also incorporate the errors in the $H\alpha$, $H\beta$, and UV fluxes, in this calculation. For that, in the bootstrap resampling, once a galaxy is drawn from the original sample, we perturb its $H\alpha$, $H\beta$, and UV fluxes within their 1σ errors on a normal distribution and draw a random value from the distribution for each flux. This way, we include the $H\alpha$ and $H\beta$ flux errors on the $A_{H\alpha}$ determination and the $H\alpha$ and UV flux errors on the $\log(\xi_{ion})$ determination.

Note that we are calculating the average of $\log(\xi_{ion})$ and not the log of the average ξ_{ion}, since the latter is biased toward larger ξ_{ion} values in the sample. For instance, consider an extreme case where the sample consists of only two objects with the $\log(\xi_{ion})$ values of

26.4 and 24.6. In this instance, the average of $\log(\xi_{ion})$ is 25.5; however, the log of the average ξ_{ion} would be log(average($10^{26.4}$, $10^{24.6}$)=26.1 which is much closer to the largest ξ_{ion}(26.4) rather than 24.6. Given that, we chose to use average (log (ξ_{ion})) as an appropriate way to evaluate the $\log(\xi_{ion})$ for the sample.

In column 2 of Table 3.1, we present the derived average ($\log(\xi_{ion})$) and its error for three bins of stellar masses of $log(M_*) < 8$, $8 < log(M_*) < 8.75$ and $log(M_*) > 8.75$. This method of stacking has also been used in Bouwens et al. (2016a); Shivaei et al. (2017).

2) *Ratio of the averages:* In the second method, we want to find the log of the ratio of total Hα fluxes to the total UV fluxes. For this, we need to take the average of all Hα fluxes and divide it by the average of all UV fluxes. Similar to the first method, we estimate the uncertainties of this method by constructing 100000 resamples of the original data with bootstrap resampling. Except that here we take the log of ratio of the average (Hα) to the average (UV) of each resampled data and evaluate the 68% uncertainty of this distribution as the error on the $\log(\xi_{ion})$ derived from this method. In addition, similar to the first method, for each randomly selected galaxy, we perturb its $H\alpha$, $H\beta$, and UV fluxes within their 1σ errors on a normal distribution and for each flux, we draw a random value from the corresponding distribution. This way we can include the flux errors into the $\log(\xi_{ion})$ uncertainties. The composite values of $\log(\xi_{ion})$ is reported in column 3 of Table 3.1.

This method of stacking has been used in Matthee et al. (2017) for the ξ_{ion} determination in a similar manner by taking the ratio of median $L_{H\alpha}$ to median L_{UV}.

(1) $log(M_*)$	(2) $log(\xi_{ion})$	(3) $log(\xi_{ion})$
≤ 8	$25.58^{+0.32}_{-0.49}$	$26.10^{+0.36}_{-0.59}$
$8 - 8.75$	$25.36^{+0.16}_{-0.15}$	$25.55^{+0.1}_{-0.1}$
$8.75 - 9.7$	$25.17^{+0.18}_{-0.22}$	$25.40^{+0.12}_{-0.21}$

Table 3.1: Col. (1): Log of stellar mass bins in units of $M_{\odot}/yr$. Col. (2): log(ξ_{ion}) inferred from "*Average of the Ratios*" approach . Col. (3): log(ξ_{ion}) inferred from "*Ratio of the Averages* " stacking method.

3.6 Results

We present the log(ξ_{ion}) derived from our two stacking methods as a function of log (mass) in Figure 3.2. When stacking galaxies' fluxes at specified stellar mass bins, it is important to ensure that their mass measurements do not suffer from high uncertainties. In fact there are only four galaxies that lack HST rest-frame near-IR filter coverage and ultimately end up having large mass errors. These are shown in gray points in Figure 3.1. So we make sure not to include them in our stack measurements.

We note that our sample is complete above $10^8 M_{\odot}$ which corresponds to the two right data points shown with red filled markers in Figure 3.2. Below this mass, it is likely that we have only detected the bright objects and missed the faint ones. As such, here we only discuss results from the stellar masses of $10^8 M_{\odot}$ and above. As it can be seen in Figure 3.2, the composite log(ξ_{ion}) is higher by at least 0.2 dex at all mass bins when using the *Ratio of the Averages* method compared to the *Average of the Ratios*. This means that the log(ξ_{ion}) inferred from our method of (*Ratio of the Averages*) gives rise to a higher ionizing photon production efficiency compared to the commonly-used method (*Average of the Ratios*).

3.6.1 Comparing to other works

Now we compare our results with other studies at different redshifts or different stellar masses. First we use a sample of local low-mass galaxies from Weisz et al. (2012b). We have determined the composite log (ξ_{ion}) of this sample in four mass bins, using the same two stacking methods we used for our sample. We show this in Figure 3.2 in green. Similar to our sample, we see that in the local sample, log (ξ_{ion}) measured from *Ratio of the Averages* are higher or at least the same as the one derived from the *Average of the Ratios*. In particular, the difference between the two methods start to increase at lower masses.

By comparing our results with Weisz et al. (2012b), we find that at a given mass, our sample has higher log (ξ_{ion}) relative to that of Weisz et al. (2012b) (compare red markers with green ones). This suggests that at higher redshifts, galaxies with typical masses less than $10^{9.5} M_{\odot}$ produce more ionizing photons compared to their low redshift counterparts.

There is a possible explanation for this controversy from the metallicity point of view: Recent studies by Steidel et al. (2016); Strom et al. (2017) predict that in high-mass ($9 \leq log(M_*/M_{\odot}) \leq 10.8$) high-redshift galaxies ($z = 2.4 \pm 0.11$), the [O/Fe] abundance is highly super-solar ($\simeq 4 - 5$ $[\mathrm{O/Fe}]_{\odot}$) which is referred to as "α element enhancement". This has been extensively tested on the composite UV spectrum of a representative sample of galaxies in KBSS-MOSFIRE spectroscopic survey. They found that stellar models with low stellar metallicities ($Z/Z_{\odot} \sim 0.1$), and subsequently low Iron abundance, best match to their composite UV continuum. The deficit of Iron can naturally be explained by the fact that these high-redshift galaxies are not old enough to develop type Ia supernovae and release an adequate amount of Iron into the interstellar medium (ISM). On the other

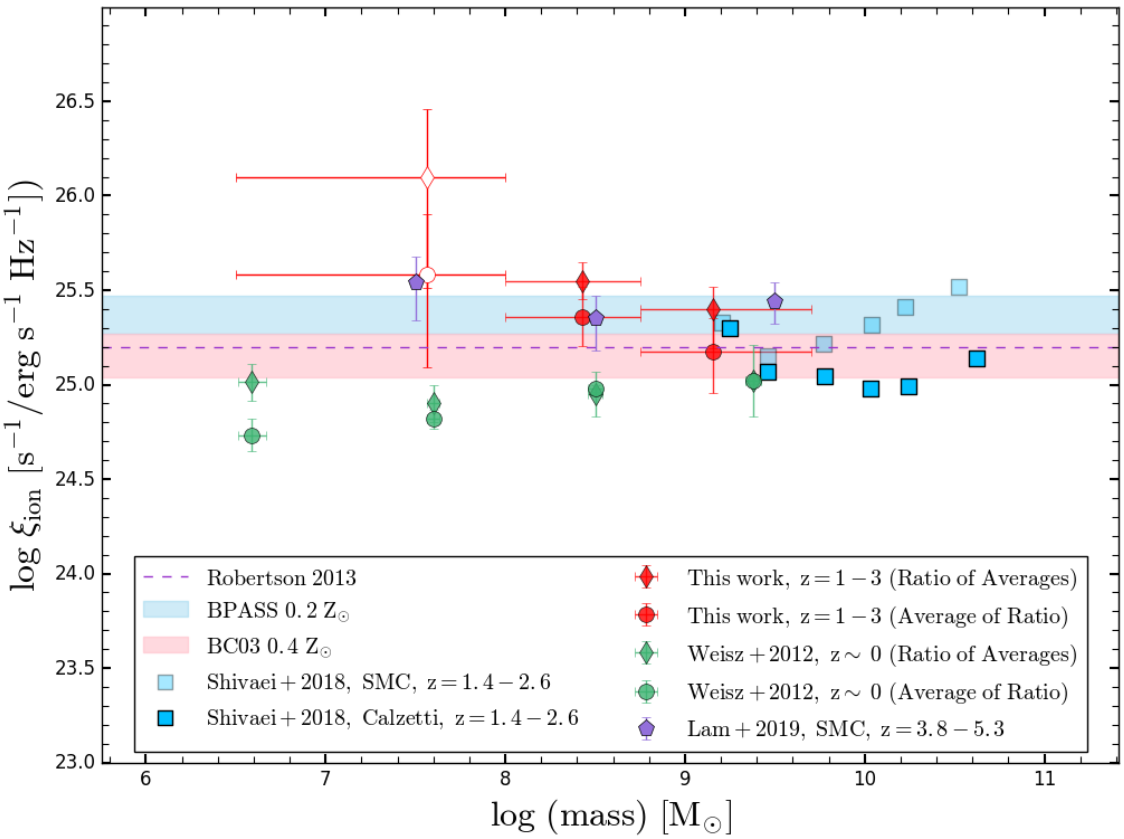

Figure 3.2: Log (ξ_{ion}) as a function of log (M_*). Log(ξ_{ion}) derived from *Average of the Ratios* stacking method are shown in red circles and *Ratio of the Averages* in red diamonds. We mark the lowest mass bin with the open circle and open diamond to emphasis that our sample is incomplete below $10^8 M_\odot$ and our calculation is biased towards bright objects at that mass bin. Log(ξ_{ion}) inferred from *Ratio of the Averages* is at least 0.2 dex larger than that of *Average of the Ratios*. Green circles and green diamonds denote the local sample of Weisz et al. (2012b) applying the *Average of the Ratios* and *Ratio of the Averages* stacking methods respectively. Bright and faded sky blue squares denote MOSDEF sample (Shivaei et al., 2017) of higher stellar mass galaxies using Calzetti et al. (2000) and SMC Gordon et al. (2003) UV dust corrections respectively. Purple pentagons show the Lam et al. (2019) sample of faint ($L_{UV} < 0.2\ L_*$) galaxies at higher redshifts ($z = 3.8 - 5.3$). The dashed line is the canonical value of 25.2 from Robertson et al. (2013). The local sample of Weisz et al. (2012b) indicates lower log(ξ_{ion}) compared to ours. High-redshift samples of Shivaei et al. (2017) and Lam et al. (2019) lie within 1σ error bars of our two stacking methods. Blue and pink bars predict the possible range of log (ξ_{ion}) derived from two different stellar models with different metallicities, (BPASS model $0.2Z_\odot$ (Eldridge et al., 2017), and BC03 $0.4Z_\odot$ (Bruzual and Charlot, 2003)), over 10-100 Myrs after a single burst of star formation.

hand, since Iron predominantly controls the opacity of extreme UV (EUV) and FUV, the deficit of it allows more EUV photons to escape from the stars. This in turn enhances the production of ionizing photons and successively causes stronger nebular emission lines at higher redshifts, leading to an increase in the ξ_{ion} compared to the local samples. We predict that this may be true for all high-redshift samples including ours. Yet the confirmation of this argument for our sample requires further investigation on the measurement of Iron abundance, incorporating the information from the UV spectrum. Thus we avoid making any strong conclusion based on that.

We also compare our sample with galaxies in MOSDEF (Shivaei et al., 2017), which are at higher stellar masses but similar redshift range as ours ($z = 1.4 - 2.6$). We show log (ξ_{ion}) values from MOSDEF assuming SMC (Gordon et al., 2003) and Calzetti et al. (2000) UV dust correction in Figure 3.2. We see that the log(ξ_{ion}) for our sample is in good agreement with that of Shivaei et al. (2017) at $10^{9.2} - 10^{9.4} M_{\odot}$, the mass range where the two sample overlap.

In addition to the low (Weisz et al., 2012b) and intermediate (Shivaei et al., 2017) redshift samples, we also looked at the high redshift sample of Lam et al. (2019), shown as purple pentagons in Figure 3.2. The sample is at redshift $z = 3.8 - 5.3$. Galaxies in this sample are primarily selected to have Lyα emission in the MUSE data. Log (ξ_{ion}) is inferred from the $H\alpha$ equivalent width which in turn is derived from the stacked Spitzer/IRAC [3.6]-[4.5] colors. The sample includes galaxies of faint UV luminosities $-20.5 < M_{UV} < -17.5$, which can be counted as the high-redshift analogues of our intermediate-redshift galaxies. The log (ξ_{ion}) from Lam et al. (2019) is within 1σ errors of either of the two stacking

methods for our sample (compare red and light purple markers).

3.7 Relation between log (ξ_{ion}) and other physical quantities

In this section we discuss the relationship between the log(ξ_{ion}) and other physical quantities such as UV magnitude, UV spectral slope (β), and the equivalent widths of nebular emission lines in our sample and compare it with other works.

In Figure 3.3 we present log (ξ_{ion}) as a function of UV magnitude (M_{UV}).

We determine the log(ξ_{ion}) for three bins of M_{UV} (-20.2 < M_{UV}, -20.2 ≤ M_{UV} < -19.2, and -19.2 ≤ M_{UV}) using the *Average of the Ratios* and *Ratio of the Averages* stacking methods as were explained in section 3.5. Log(ξ_{ion}) derived from the *Average of the Ratios* is quite constant across all three M_{UV} bins with a value of 25.3-25.4; while the *Ratio of the Averages* method indicates $\sim$ 0.2 dex larger log(ξ_{ion}) in all bins. We also show Shivaei et al. (2017); Bouwens et al. (2016a), and Lam et al. (2019) sample in Figure 3.3. Given that all these three studies have stacked their data using the average of log(ξ_{ion}), we find our *Average of the Ratios* values in a great agreement with these studies over a range of $-21 M_{UV} < -18$.

Nonetheless, we do not find any evidence of significant dependence between log(ξ_{ion}) and M_{UV} in our sample, which can also be seen in other samples.

We also search for any relation between log(ξ_{ion}) and UV spectral slope β in our sample. We split the sample into three bins of β (β <-2, -2≤ β <-1.5, -1.5≤ β) and apply the same two stacking methods at each bin as we used for log(M_*) and M_{UV}. We show our

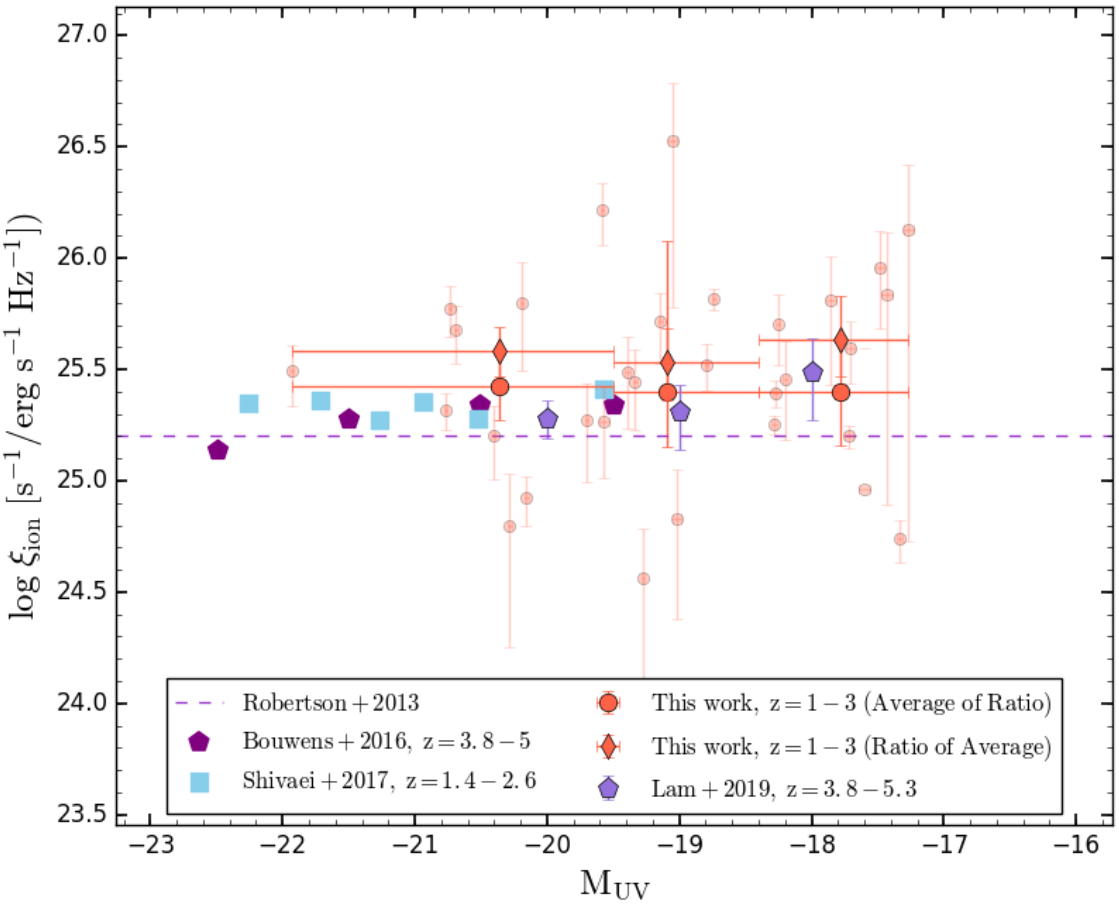

Figure 3.3: Log(ξ_{ion}) as a function of UV magnitude (M_{UV}). Small red points denote individual galaxies in our sample. The large red circles and red diamonds show the log(ξ_{ion}) derived from the *Average of the Ratios* and *Ratio of the Averages* stacking methods respectively. skyblue squares indicate Shivaei et al. (2017) for $z \sim 2$ and dark and light purple pentagons denote Bouwens et al. (2016a) and Lam et al. (2019) samples at $z \sim 4-5$ respectively. Our values derived from *Average of the Ratios* stacking are consistent with other works and also is extended to one order of magnitude fainter in UV, similar to Lam et al. (2019). No significant increase in the log(ξ_{ion}) with respect to M_{UV} is found.

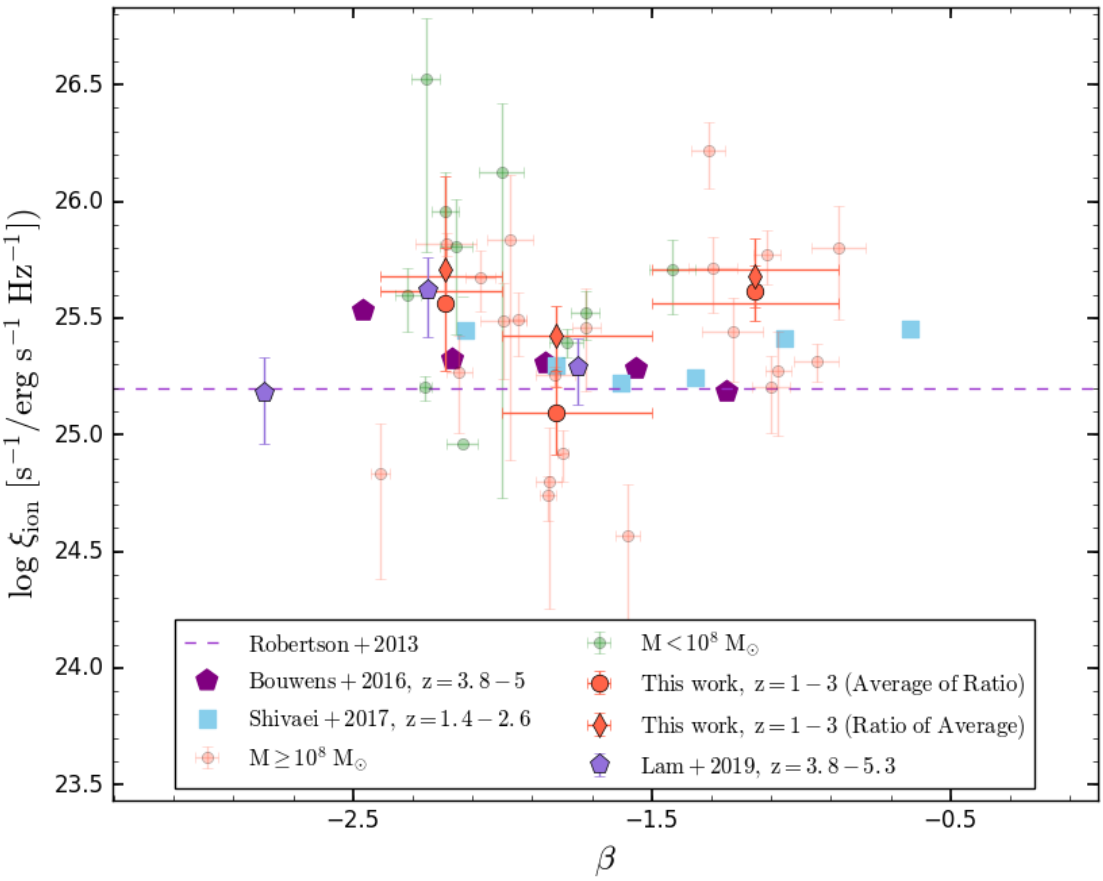

Figure 3.4: Log(ξ_{ion}) as a function of UV slope β. The symbols are the same as those presented in Figure 3.3. Except that we galaxies below $10^8 M_\odot$ in small green points in order to indicate their contribution to the lower β bins ($\beta < -1.5$). At $\beta < -1.5$, log(ξ_{ion}) decreases with increasing β (shallower UV slopes), whereas at $\beta > -1.5$, log(ξ_{ion}) starts to increase.

results in Figure 3.4. For the β slopes steeper than -1.5 ($\beta \leq -1.5$), we see that log(ξ_{ion}) increases towards steeper slopes (or bluer galaxies), which is consistent with that of Lam et al. (2019); Shivaei et al. (2017) sample. Whereas, at the β shallower than -1.5 ($\beta > -1.5$) which corresponds to redder galaxies, we see that our log (ξ_{ion}) is increased, meaning that even red galaxies with shallow UV slopes can have log(ξ_{ion}) as high as the blue and steep UV-slope galaxies. As such, β slope do not properly correlate with the log(ξ_{ion}) in our sample. We also note that most of our low-mass galaxies (below $10^8 M_{\odot}$) are populated in the steepest β slopes bin (β <-2) and have large log (ξ_{ion}) values (green circles).

Finally, we investigate the relationships between the log (ξ_{ion}) and the equivalent widths of optical nebular emission lines. The motivation for this comes from Chevallard et al. (2018), who suggested that log(ξ_{ion}) in galaxies with strong ionization emissivity are expected to scale with the equivalent width of combined [O$_{III}$] 4959,5007 lines. They showed this for a sample of local star-forming galaxies with $560 < EW_{[OIII]\lambda5007} < 2370\mathring{A}$. Tang et al. (2018) confirmed the existence of such scaling relation for a sample of 227 low-mass ($10^7 < M_*/M_{\odot} < 10^{10}$), [O$_{III}$] emitters with $225 < EW_{[OIII]\lambda5007} < 2500\mathring{A}$ at $z = 1.3-2.4$, suggesting that higher equivalent width systems are more efficient ionizing agents. Given that, we aim to test this for our galaxies which have lower equivalent widths compared to that of Chevallard et al. (2018) and Tang et al. (2018) and see if this relation further extends to lower equivalent width systems or not. We show the log(ξ_{ion}) vs. log [O$_{III}$]5007 equivalent width (EW$_{[OIII]\lambda5007}$) in Figure 3.5. Our galaxies span $20 < EW_{[OIII]\lambda5007} < 1500\mathring{A}$. There is an increasing trend between log(ξ_{ion}) and log([O$_{III}$]). To quantify this trend, we perform a linear fit to the sample using ordinary least squares along with the 68% credible region.

We see a correlation between $\log(\xi_{ion})$ and $\log(\mathrm{EW}_{[OIII]\lambda5007})$ with a slope of 0.48 ± 0.16 which lends support to what Chevallard et al. (2018) and Tang et al. (2018) claimed.

In addition we overlay the trend from Tang et al. (2018) in which $EW_{[OIII]\lambda5007}$ are larger than that of ours ($225 < EW_{[OIII]\lambda5007} < 2500$ $\mathring{A}$). Their trend is steeper, with smaller scatter. The discrepancy between the two trends might be due to our small sample size which has one-tenth fewer sources than Tang et al. (2018).

We also demonstrate the $\log(\xi_{ion})$ vs. Hα equivalent width ($EW_{H\alpha}$) relation in Figure 3.6. After fitting a line through the points, we find a slope of 0.63 ± 0.17 which indicates a remarkable correlation between the two indicators. This trend has a similar slope to that of Tang et al. (2018) but again with a larger scatter. This means that the $\log(\xi_{ion})$ is highly correlated with the $EW_{H\alpha}$ than the $EW_{[OIII]\lambda5007}$ as is predicted by Tang et al. (2018).

In Section 3.8 we attempt to explain the physical driver of such correlation between $\log(\xi_{ion})$ and either $EW_{H\alpha}$ or $EW_{[OIII]\lambda5007}$ for very low-mass systems.

This correlation between the $\log(\xi_{ion})$ and the equivalent widths of some ionization-sensitive nebular emission lines can be used as a proxy for ξ_{ion} at high-redshifts when the direct measurement of rest-frame UV_{1500} is not available.

3.8 What physically drives the spread in $\log(\xi_{ion})$?

Aside from the galaxy-to-galaxy dust variation, the scatter in $\log(\xi_{ion})$ or specifically $\log(L_{H\alpha}/L_{UV})$ can also be, in part, due to other factors such as star formation rate

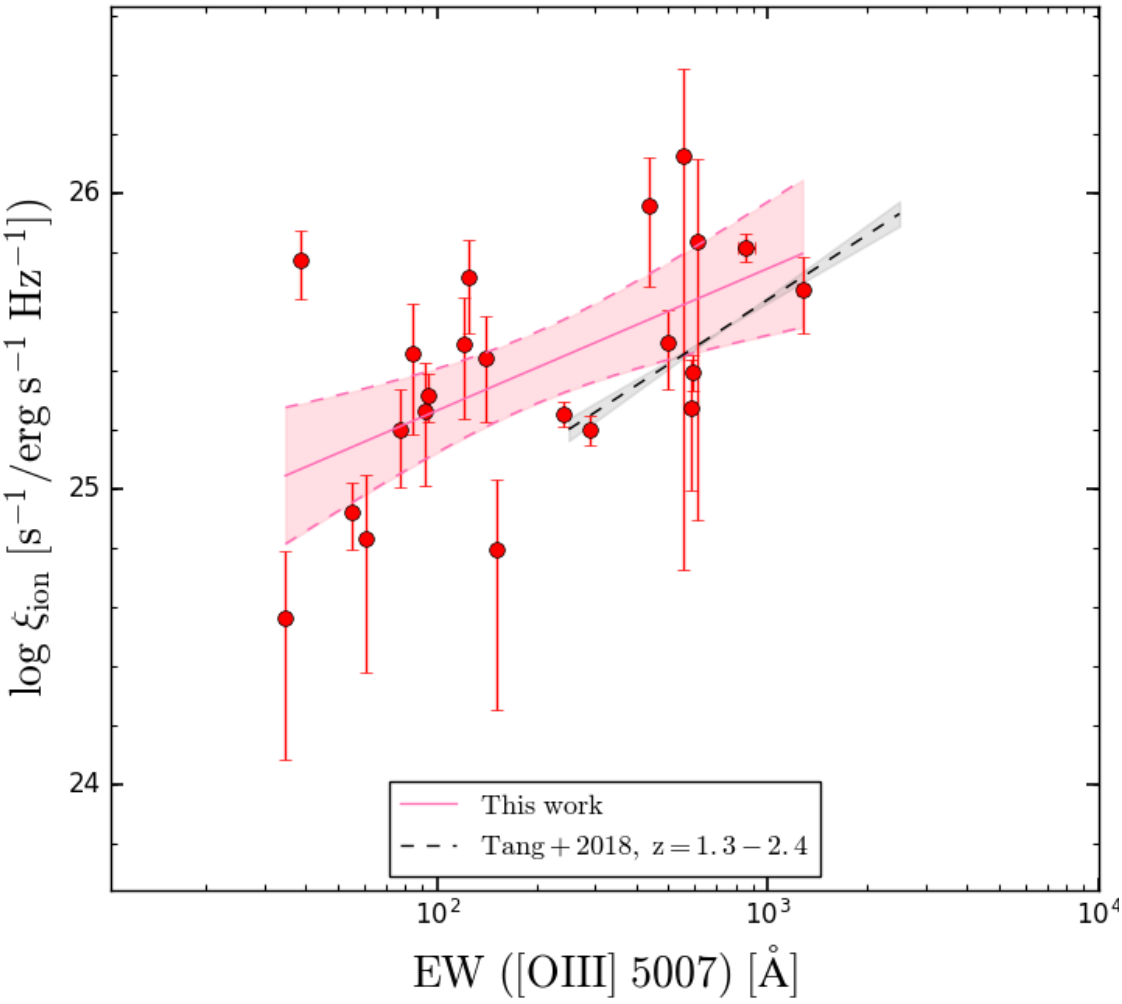

Figure 3.5: log (ξ_{ion}) vs. [O_{III}] 5007 equivalent width. The solid red line and the pink region denote the best-fit line and 1σ confidence level respectively. Gray dashed line is from Tang et al. (2018) for extreme [$OIII$] emitters at $z = 1.3 - 2.4$. Overall, a positive slope of 0.48 ± 0.16 is apparent between the two indicators, but less steep than Tang et al. (2018).

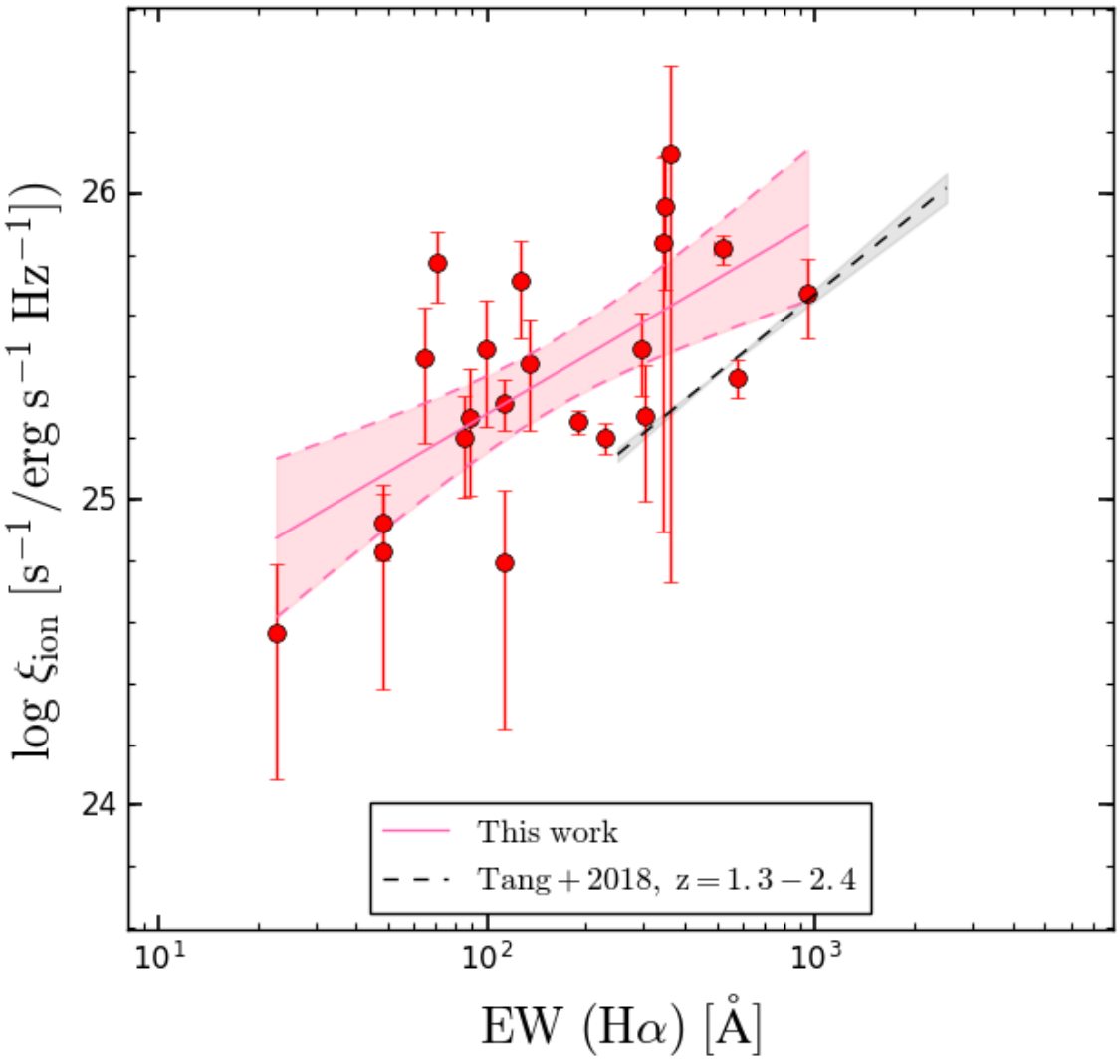

Figure 3.6: log (ξ_{ion}) vs. Hα equivalent width ($EW_{H\alpha}$). The solid red line and the pink region denote the best-fit line and 1σ confidence level respectively. Gray dashed line is from Tang et al. (2018) for extreme $[OIII]$ emitters at $z = 1.3 - 2.4$. There is a slope of 0.63 ± 0.17 between the two indicators, an evidence of log (ξ_{ion}) being highly correlated with the $EW_{H\alpha}$.

variation, metallicity difference, stellar populations difference, ionizing photon escape fraction, different initial stellar mass function, etc.

To account for the effect of some of these factors on the log (ξ_{ion}) variation, we determine the expected log (ξ_{ion}) range for two different stellar population synthesis models and different stellar metallicities: model i) BPASS (Eldridge et al., 2017) with 0.2 $Z_{\odot}$ metallicity and model ii) BC03 (Bruzual and Charlot, 2003) with 0.4 $Z_{\odot}$.

The BPASS model takes into account the effect of binary stars and mass transfer that increases the number of massive stars at later stages. This will increase the amount of ionizing photons. Also, low stellar metallicity increases the temperature of the stars and increases the amount of ionizing radiation in stars. The combination of binary stars and a low metallicity assumption gives rise to higher production of log (ξ_{ion}) in model (i) compared to model (ii). The predicted log (ξ_{ion}) range for models (i) and (ii) is presented as light blue and orange horizontal bands in Figure 3.2 respectively. There is about 0.2 dex difference in log(ξ_{ion}) between the two models.

We also convolve each stellar model with a single burst star formation history and calculate the associated log (ξ_{ion}) over the time period of 10 to 100 Myr after the burst. This results in $\sim$ 0.2 dex variation in log (ξ_{ion}) due to the star formation variation shown as the blue and pink bands in Figure 3.2.

Also when combining these two bands, we see that the stacked galaxies in our sample and those in Shivaei et al. (2017) and Lam et al. (2019) are placed roughly inside these two combined regions ($25 < \log(\xi_{ion}) < 25.5$), indicating that these samples might have metallicities and stellar populations similar to those predicted by these two models.

Nevertheless, given that star formation process is controlled by an interplay of different mechanisms, in reality galaxies have more complicated star formation histories than a simplistic single burst that we assumed above. More specifically, in low mass systems, it is the stellar feedback that predominantly changes the star formation rate in a stochastic way. This effect is also predicted in the high resolution hydrodynamical simulations and is referred to as *burstiness* (Governato et al., 2010; Hopkins et al., 2014; Domínguez et al., 2015; Hopkins et al., 2018). Recent studies attempted to characterize the burstiness based on the observed $\log(L_{H\alpha}/L_{UV})$ (Lee et al., 2009; Weisz et al., 2012b; Domínguez et al., 2015; Sparre et al., 2017; Guo et al., 2016b; Emami et al., 2018) arguing that the scatter in the $\log(L_{H\alpha}/L_{UV})$ is mainly driven by the star formation change rather than other factors such as metallicity, stellar population and so on. In an attempt to parametrize the star formation histories of local galaxies, they found that low-mass galaxies are featured with bursts of star formation which have larger amplitudes and shorter timescales compared to that of more massive galaxies.

As such, we think that perhaps it is burstiness that is mainly driving this large scatter in the $\log(\xi_{ion})$ distribution of our sample ($24.5 < \log(\xi_{ion}) < 26.5$) which can not be fully explained by other factors such as the metallicity or different stellar models.

We also think that the correlation between the $\log(\xi_{ion})$ and $EW_{H\alpha}$, $EW_{[OIII]\lambda5007}$ is evidence for the burstiness in our sample. Here we attempt to provide a physical intuition on how burstiness can drive such relations between these observables.

Given that the ionization-sensitive nebular emissions ($EW_{H\alpha}$ and $EW_{[OIII]\lambda5007}$) are linked to the amount of ionizing photons in the galaxies and the fact that ionizing

photons are predominantly produced by Massive hot O-type stars, we can place constraint on the strength of these emission lines via the abundance of O-type stars in a galaxy.

On the other hand, due to the short life-time (of about few Myrs) of O-type stars, the rate of their birth and death equilibrates very fast such that their abundance reaches to a constant amount quickly after few Myrs of any star formation change. This can also be reflected in the strength of the ionization-sensitive nebular emission lines. This means that the equivalent width of these nebular lines can vary with the star formation change very quickly. Furthermore, $\log(L_{H\alpha}/L_{UV})$ also traces the recent change in the star formation rate (See Emami et al. (2018), Figure 9). This means that $\log(L_{H\alpha}/L_{UV})$ and the equivalent width of ionization-sensitive nebular lines have to both increase and decrease with any increase and decrease of the star formation rate. This explains why we see a correlation between the $\log(\xi_{ion})$ - $\log(EW_{H\alpha})$ and $\log(\xi_{ion})$ - $\log(EW_{[OIII]\lambda5007})$ in Figures 3.5 and 3.6. Nevertheless, we believe that we need to increase the number of objects in our sample in order to see more clear correlations between these indicators in Figures 3.5 and 3.6.

3.9 Summary

In this paper we measured the ionizing photon production efficiency per unit 1500 $\mathring{A}$ UV luminosity (ξ_{ion}) of a sample of low-mass ($6 < log(M*/M_{\odot}) < 10$) lensed galaxies at an intermediate redshift range of $1-3$. Thanks to the lensing effect, we were able to identify these faint sources whose light is magnified by the foreground lensing clusters (Abell 1689, MACS J0717, and MACS J1149), enabling us to extend the ξ_{ion} measurement

to fainter UV magnitudes than was ever probed ($MUV < -18$). We took the ratio of $H\alpha$ over $1500\mathring{A}$ UV flux to measure ξ_{ion} via MOSFIRE/Keck spectroscopy and HST imaging. We estimated the stellar mass from the HST rest-frame UV, optical and near-IR multiband photometry. We cleared the sample from sources with large magnifications, high $H\alpha$ flux slit loss, multiple images, and high $H\alpha$ flux errors. We used Balmer decrement technique to correct $H\alpha$ luminosity for dust. We found that our sample is incomplete below mass of $10^8 M_{\odot}$ thus we decided not to include them in our log (ξ_{ion}) measurement.

We divided the sample into bins of different physical quantities such as mass, UV magnitude (M_{UV}) and UV spectral slope (β) and calculated the log(ξ_{ion}) of composite fluxes at each bin using two different stacking methods. The common method is to take the average of the log ($L_{H\alpha}/L_{UV}$) of galaxies in each subsample that implies the typical log(ξ_{ion}) value, referred to as "*Average of the Ratios*". The second method is to take the log of sum($L_{H\alpha}$)/sum(L_{UV}) or equivalently log of average($L_{H\alpha}$)/average(L_{UV}) which referred to as "*Ratio of the Averages*". This method is more favorable than the former as it gives the total ionizing UV luminosity density once it is multiplied by the total non-ionizing UV ($1500\mathring{A}$) luminosity density inferred from the UV luminosity function. Here we list our main results:

- In samples with larger spread in log(ξ_{ion}) distribution, the composite log(ξ_{ion}) from the two stacking methods diverge dramatically from one another. This is especially true for the low mass samples as in these systems, log(ξ_{ion}) vary largely due to the stochastic nature of star formation, called "burstiness", and the log(ξ_{ion}) sample has a larger scatter. This is evident in the low mass local sample of Weisz et al. (2012b)

in Figure 3.2.

- We found that the $\log(\xi_{ion})$ inferred from *Ratio of the Averages* is at least 0.2 dex higher than that of *Average of the Ratios*. This delivers an important message that low mass systems have indeed greater $\log(\xi_{ion})$ than what is commonly thought from *Average of the Ratios* stacking method.

- Our sample indicates higher $\log(\xi_{ion})$ than the low mass local sample of Weisz et al. (2012b). We argue that this is due to the [O/Fe] enhancement at higher redshifts in which there are fewer Type Ia supernovae occurrence and, thus, lower Iron abundance which leads to a larger ionizing UV photon radiation (Steidel et al., 2016).

- We found similar $\log(\xi_{ion})$ for our sample and Shivaei et al. (2017) and Lam et al. (2019). The log (ξ_{ion}) derived from these three samples are roughly consistent with the predictions of single and binary stellar models with an assumption of 0.2-0.4 $Z_{\odot}$ stellar metallicity.

- There is no strong dependence between $\log(\xi_{ion})$ and M_{UV} and β slope in our sample. Furthermore, our results are consistent with other studies at higher redshifts (Bouwens et al., 2016a; Shivaei et al., 2017; Lam et al., 2019)

- There is a positive relation between the $\log(\xi_{ion})$ and $H\alpha$ and $\log(\xi_{ion})$ and $[\mathrm{OIII}]_{5007}$ equivalent widths in our faint low-equivalent width systems. This poses a new proxy for the ξ_{ion} determination via measuring the optical nebular emission lines at higher redshifts when the direct measurement of rest-UV fluxes is not possible. However the relationship is less tight between $\log(\xi_{ion})$ and $[\mathrm{OIII}]_{5007}$ equivalent width in our

sample that can be alleviated if by increasing the number of objects in our sample.

Chapter 4

Testing the effects of burstiness on the stellar and gas dynamics of dwarf galaxies

4.1 Introduction

Predictions from hydrodynamical simulations that incorporate stellar feedback into the ΛCDM model suggest that bursty star formation can have impacts on the gas and stellar kinematics of galaxies (El-Badry et al., 2016). For example outflows driven by stellar feedback can drive stars away from the center of the galaxy. Once the outflows stop and stars are at their maximum displacement from initial position, the gravitational potential pulls stars back to the center. This process gets repeated after each burst event and results in a size fluctuation by more than a factor of 2 over $\sim$ 200 Myr in the galaxy (El-Badry

et al., 2016). Furthermore, these feedback-driven outflows can inject momentum radially to gas particles and kick them out of the center, resulting in destruction of any gas disc-like structures. Once the outflows are gone, the gravitational potential takes control of gas infall to the center in the form of gas streams and eventually resumes the star formation. Similar to the size fluctuation, this processes repeats during each burst of star formation and can cause a variation in the radial velocity of the gas inside the galaxy.

Here we aim to observationally test these two predictions of "size fluctuation" and "gas velocity variation" for a sample of low-mass local galaxies whose stellar masses range from $10^7 - 10^{9.6} M_{\odot}$, the same regime suggested by El-Badry et al. (2016). For the "size fluctuation", one can measure the fluctuation in the half-light radius at a fixed stellar mass (M_{star}). For that, we use the R-band images of the galaxies and measure their half-light radii. We specifically choose R-band as it reflects the light from all populations of young and old stars. In that case we can inclusively measure the size fluctuation due to the migration of all stars and not only those with a specific age range.

The "gas velocity variation" can also be observationally tested by quantifying the shape of the gas velocity profiles. For that, we make use of the spectra of neutral hydrogen (HI) 21 cm emission of these galaxies collected from different surveys. We measure the steepness in the line profile wings utilizing the definition in El-Badry et al. (2018a).

We also investigate whether the "size fluctuation" and "gas velocity variation" are truly driven by the bursty star formation (burstiness) or not. For that we investigate their relationship with the star formation rate (SFR) indicators. The two well-known SFR indicators are the Hα and UV_{1500} luminosities, which trace the SFR over the last ~ 5 and

20 Myrs (Flores-Velazquez et al. in prep.).

In the following we provide a brief description of this analysis and discuss the results.

4.2 Data

We use the sample of Weisz et al. (2012b) which is a subsample of the Local Volume Legacy (LVL) Survey. The parent sample is complete in including all nearby field galaxies within 11 Mpc and consists of spirals and irregulars that avoid the Galactic plane($|b| > 20^{\circ}$) and are brighter than $B = 15$ mag. The UV_{1500} and Hα photometry is obtained from 11 Mpc $H\alpha$ and UV Galaxy Survey (11HUGS, Kennicutt et al. (2008); Lee et al. (2011)). Stellar masses were determined by Weisz et al. (2012b) using optical photometry from the Sloan Digital Sky Survey and *Spitzer* mid-IR (IRAC) photometry from the Local Volume Legacy (LVL) Survey (Dale et al., 2009). R-band images with removed foreground stars and nearby contaminants are obtained from Cook et al. (2014).

The HI 21 m emission profiles were also obtained from the NASA/IPAC Extragalactic Database (NED) [1]. All these HI emission spectra Huchtmeier and Richter (1986); Tifft and Cocke (1988); Springob et al. (2005) have reliably high velocity resolutions of 5 km/s or less.

We note that we only keep galaxies whose stellar masses are within $10^7 - 10^{9.6} M_{\odot}$ where burstiness is predicted to be more important than other mass ranges (El-Badry et al., 2016).

[1]The NASA/IPAC Extragalactic Database (NED) is operated by the Jet Propulsion Laboratory, California Institute of Technology, under contract with the National Aeronautics and Space Administration.

4.3 Measurements

4.3.1 R-band Half-light radii

For the "size fluctuation", we determine the half-light radii from the R-band images of each galaxies in the sample. For that, we run the SourceExtractor (Bertin and Arnouts, 1996a) code on R-band images to identify the galaxies' regions and measure their half-light radii (R_e). Whenever the galaxy's structure is too resolved such that SourceExtractor confuses the galaxy as multiple objects, we decide to smooth the image by applying a Gaussian kernel with a minimum FWHM necessary for the SourceExtractor to recognize the galaxy as a single source. To be consistent with El-Badry et al. (2016) analysis, we only keep objects with axis ratios > 0.5 and stellar masses between $10^7 - 10^{9.6} M_\odot$.

4.3.2 HI line profiles corrections

Before measuring the steepness of the wings, we first need to apply some refinements to the HI velocity profiles. We first Hanning-smooth the line profiles to a resolution of 5 km/sec for each velocity profile. This helps eliminate any spurious noise feature within the HI emission that may drop below zero and cut the emission profile artificially. Denoting the peak flux density f_{peak}, second we fit a second-order polynomials to either sides of the wing between 0.5 f_{peak} and where the flux goes to zero. This procedure has been used by Bradford et al. (2015); El-Badry et al. (2018b) in order to minimize the noise in the wings. For consistency, we also use this in our analysis. In section 4.4.2 we describe our measurement of the steepness of the line profiles.

4.4 Results

4.4.1 Size Fluctuation

We present the log(R_e) - log(M_*) relation of our sample in Figure 4.1. As one might expect, there is a correlation between the two quantities such that more massive galaxies have larger effective radii. However, since we are only interested in finding the R_e fluctuation as a function of burstiness and not the mass, we choose to subtract the trend from our log R_e measurements. We find this trend by fitting a line through the log(R_e) - log(M_*), shown as red solid line. We then subtract off the log(R_e) from this trend and show it as log($R_e/\bar{R}$). log($R_e/\bar{R}$) is a measure of a galaxy's size relative to the average regardless of its mass. Positive log($R_e/\bar{R}$) indicates a galaxy whose half-light radius is larger than the average while negative log($R_e/\bar{R}$) indicates those with half-light radius smaller than the average.

We then sort galaxies based on their log($R_e/\bar{R}$) and display the postage stamp of each galaxy's image in Figure 4.2. For a fair comparison, we scale the images as if they are all at the same distance from us and have the same stellar mass.

Now we examine to see whether there is any relation between the size fluctuation and bursty star formation in the sample or not. As such we use Hα and UV_{1500} luminosities as the two known indicators that trace the star formation rate averaged over the last 5 and 20 Myrs. We then derive the SFRs inferred from both Hα and UV_{1500} luminosities using the Kennicutt (1998) conversion factors. We also divide the Hα- and UV_{1500}-inferred SFRs of each galaxies by their masses and refer to them as $sSFR_{H\alpha}$ and $sSFR_{UV}$ respectively.

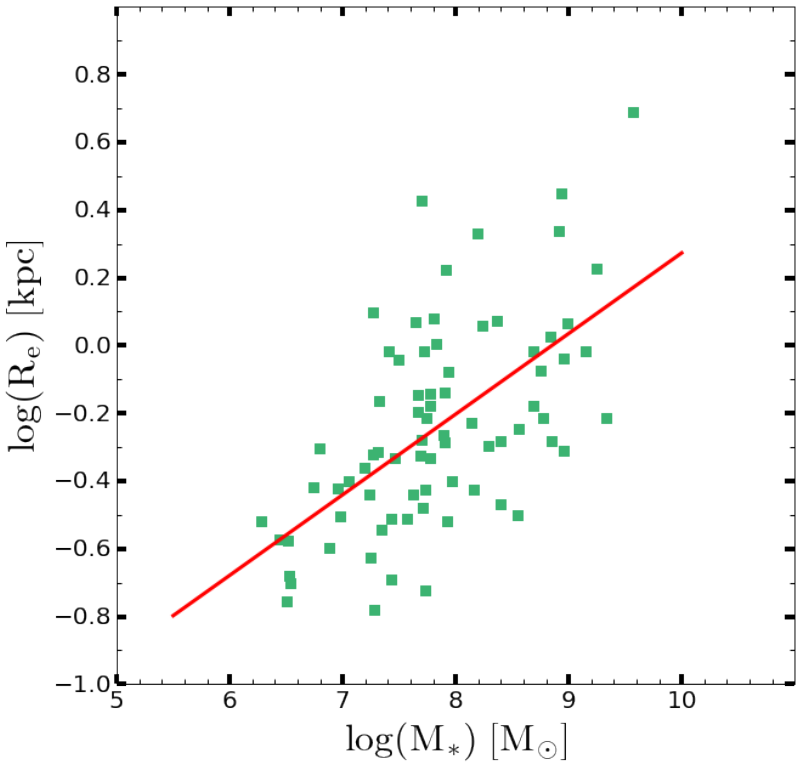

Figure 4.1: Log (half-light radius) vs. log(mass). Correlation between the two quantities is clearly present. The linear fit through log(R_e)-log(M_*) is shown as red curve.

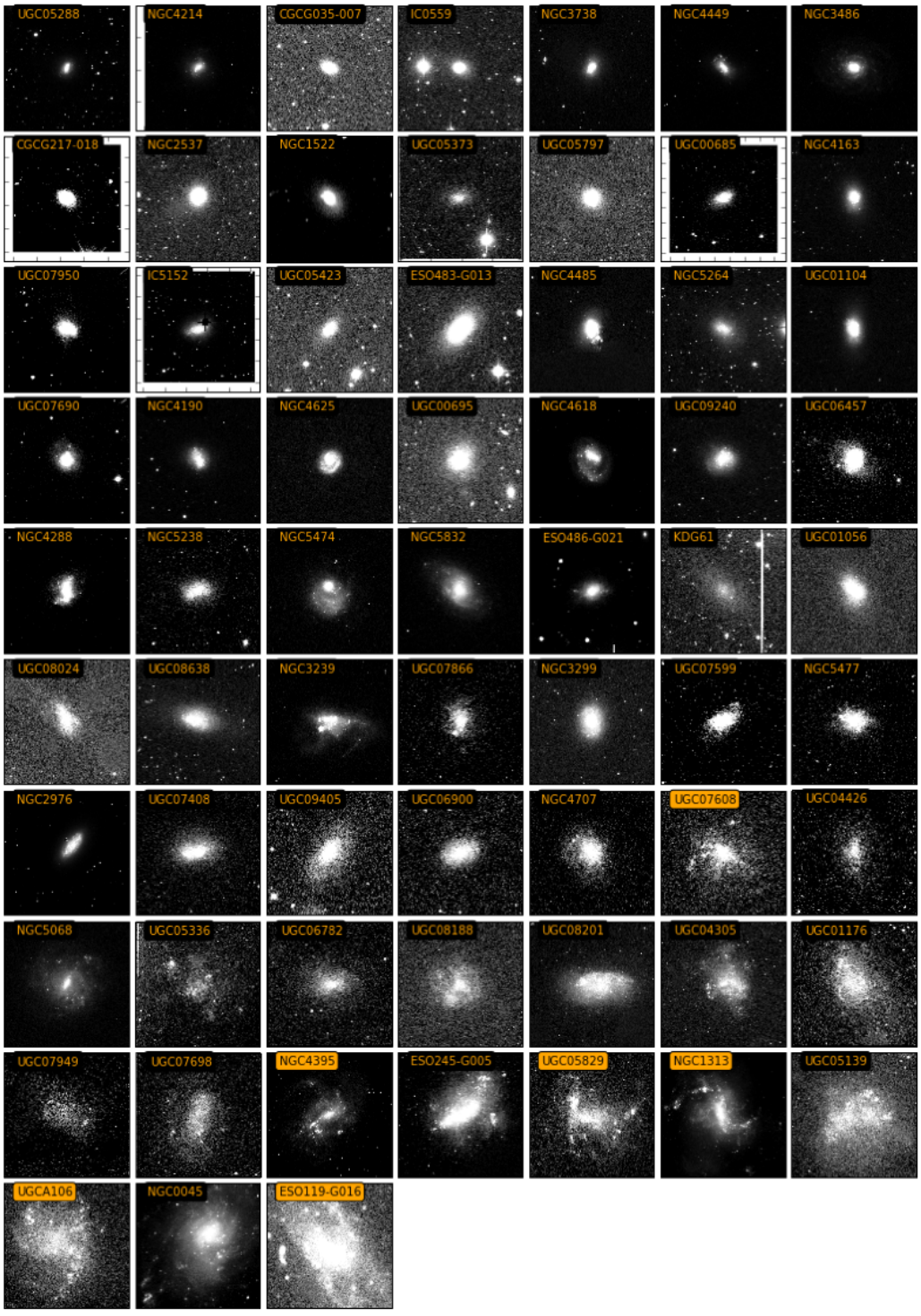

Figure 4.2: Postage stamps of galaxies sorted by their $\log(R_e/\bar{R})$ (half-light radius relative to the mean) and scaled as if they are all at the same distance and the same mass.

We then divide the sample into four mass bins since galaxies of similar mass range are expected to share common star formation properties. We show the $\log(\mathrm{sSFR}_{UV})$ and $\log(\mathrm{sSFR}_{H\alpha})$ vs. $\log(\log(R_e/\bar{R}))$ in Figure 4.3. The linear fit along with the 68% confidence regions are shown in black lines and blue areas respectively. It is clear that there is a correlation between sSFR_{UV} and $\log(R_e/\bar{R})$especially at masses below $10^{7.85}M_{\odot}$ with a small scatter. The trend is less significant in the $\mathrm{sSFR}_{H\alpha}$ with a larger scatter. This suggests that the size and UV luminosity both increase and decrease at the same time in response to the burstiness, while this is not the case or maybe less strong between the size and $H\alpha$ luminosity. We also see that there is a size fluctuation for masses greater than $10^{7.85}M_{\odot}$ evidenced as a large range of $\log(R_e/\bar{R})$ which can not be explained by the star formation variations. So based on our results there is some evidence that burstiness may drive size fluctuations only at mass ranges less than $10^{7.85}M_{\odot}$.

4.4.2 Gas velocity variation

Next we examine the effect of bursty star formation on the gas velocity variation using the HI 21 cm velocity profiles. This gas velocity variation can appear as changing the shape of the gas emission line by making it broader or narrower. However we note that broadening can also be different for different viewing angles especially for spiral disc-like galaxies. In this case, an edge-on viewed disc exhibits a broad double-horn emission profile while a face-on viewed disc exhibits a single-peak, less broad, Gaussian-like profile. Importantly, what is not affected by different viewing angles is the steepness of the wings of the line profile. Based on this argument, we choose to determine the wing steepness as

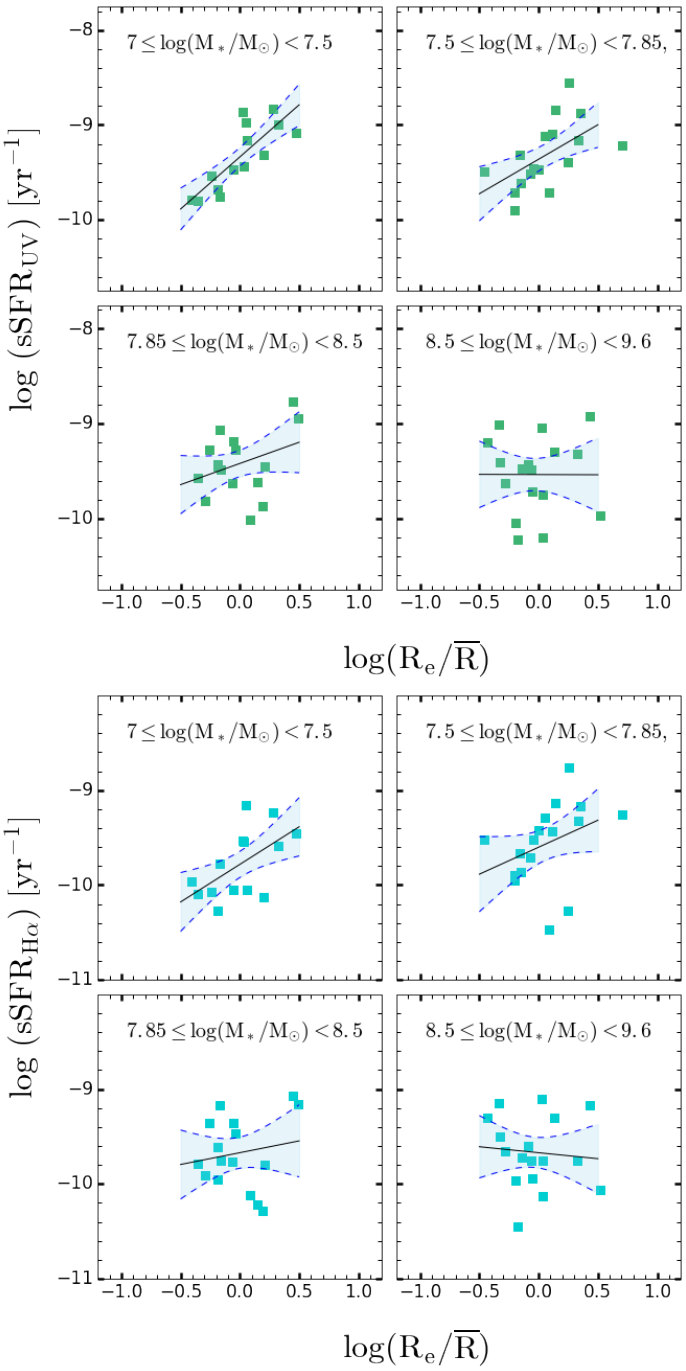

Figure 4.3: Top: Log(sSFR$_{UV}$) vs. log(log($R_e/\bar{R}$)). A linear fit and 68% confidence region are shown as black lines and blue areas. There is a clear correlation at $10^7 \leq \mathrm{M}_* < 10^{7.85}$ $\mathrm{M}_\odot$ which disappears at larger masses. This is evidence that bursty star formation can cause size fluctuations in low-mass galaxies. Bottom: Log(sSFR$_{H\alpha}$) vs. log(log($R_e/\bar{R}$)). Again we see that there is a steep slope at lower masses which becomes shallower towards larger masses. However, the scatter is larger compared to the sSFR$_{UV}$.

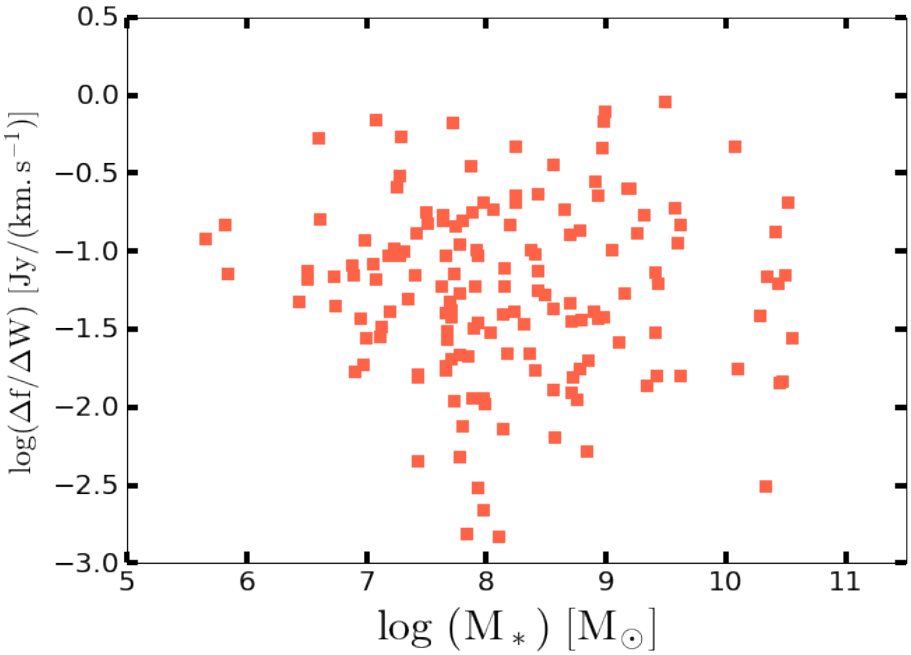

Figure 4.4: Log($\Delta f/\Delta W$) vs. log (mass). This demonstrates there is no relationship between the stellar mass and the wing steepness of the HI line profiles.

a measure for the gas velocity variation and analyse its relation with the burstiness effect. For that we define the wing steepness as $(f_{50} - f_{20})/(W_{20} - W_{50})$ where f_{50} and f_{20} are the 50% and 20% of the flux peak while W_{50} and W_{20} are the widths of the line at 50% and 20% of the flux peak. This way we take into account the steepness of both sides of the wing and refer to it as $\Delta f/\Delta W$. Steep wings will indicate smaller $\Delta f/\Delta W$whereas sloped wings indicate larger $\Delta f/\Delta W$. We note that this definition here is slightly different from that of El-Badry et al. (2018b) in which case we normalize the difference in the line widths $((W_{20} - W_{50}))$ by the flux while they normalized this difference by the line width (W_{50}). Figure 4.4 shows the log $(\Delta f/\Delta W)$ as a function of log (M_*). It is clear that $\Delta f/\Delta W$or equivalently, the wing steepness has no dependence on the galaxy's mass.

In Figure 4.5 we present a subsample of HI velocity profiles sorted by their wing steepness ($\Delta f/\Delta W$) in which case the top left subplot has the smallest log($\Delta f/\Delta W$) and, thus, has the steepest wings. The bottom right subplot has the largest log($\Delta f/\Delta W$) and, thus, has the most sloped wings among the sample.

Now we want to examine whether this wing steepness is dependent on the star formation rate or not. Given that, similar to Figure 4.3, we plot log (sSFR$_{UV}$) and log (sSFR$_{H\alpha}$) vs. log($\Delta f/\Delta W$) for four mass bins and present it in Figure 4.6. We again see a correlation between log(sSFR$_{UV}$) and log ($\Delta f/\Delta W$) more significantly for the mass bin of $10^{7.5} - 10^{8.5}$ $M_{\odot}$. Log(sSFR$_{H\alpha}$) vs. log ($\Delta f/\Delta W$) also shows this positive correlation but with larger scatter. This means that the sSFRs are correlated with the wing steepness such that the wings are steeper at higher sSFRs and become less steep at lower sSFRs.

4.5 Discussions

Based on Figures 4.3 and 4.6, we see that UV-inferred sSFR is positively correlated with both log($R_e/\bar{R}$) and $\Delta f/\Delta W$. This means that when the UV luminosity is high, the size of the galaxy is large and its gas radial velocity is low. On the other hand, once the UV luminosity is low, galaxy size is small and gas velocity is high. One way to explain this could be that once UV is at the highest, it has been 20 Myrs since a burst of star formation. During this time, SNe have blown out and have driven outflows which in turn have dissipated stars and expanded the galaxy. At this point the galaxy has reached to its maximum size possible and gradually becomes free from any outflowing winds. Based on

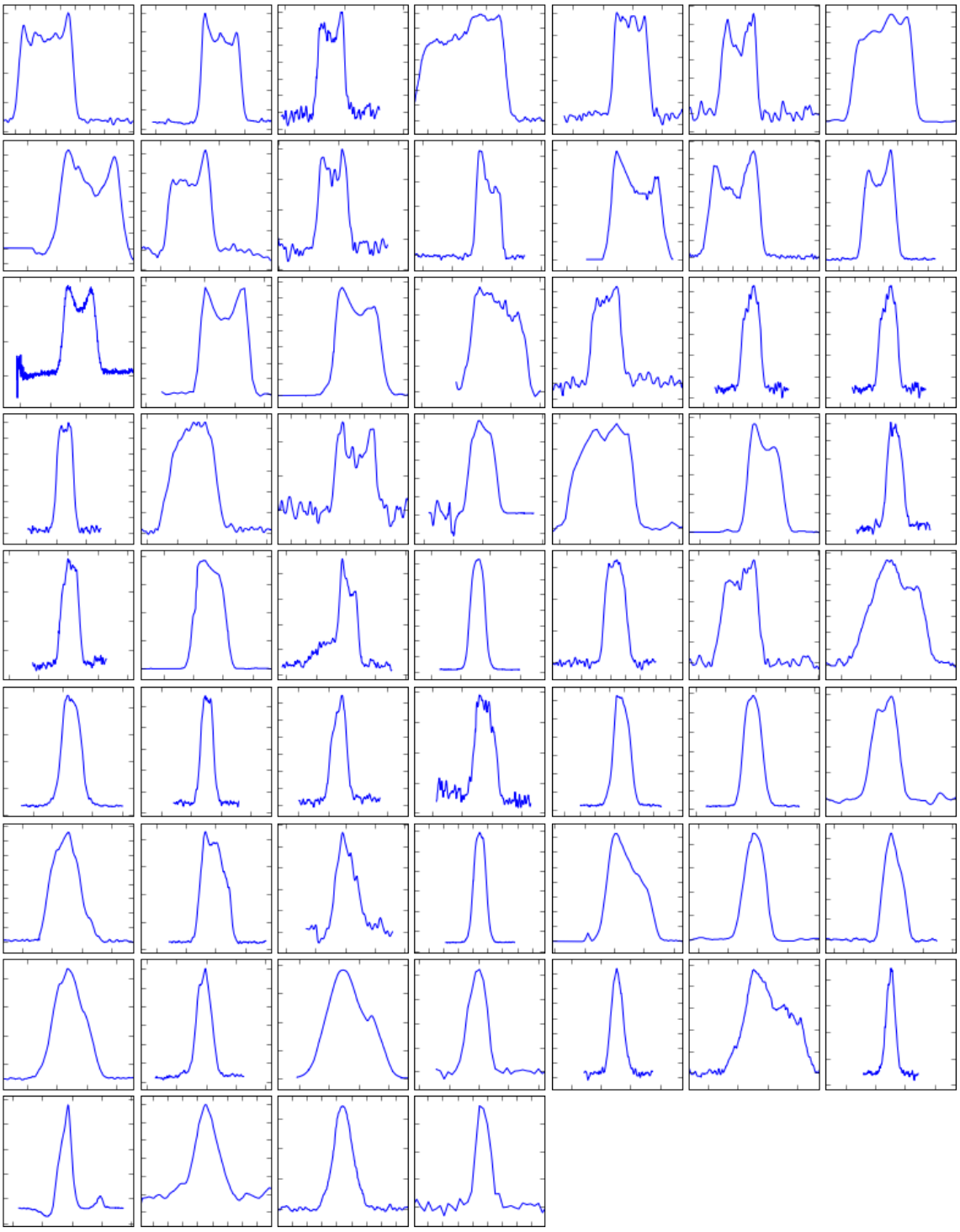

Figure 4.5: HI 21cm velocity profiles sorted by wing steepness relative to the average ($\Delta f/\Delta W$). The top left panel has the steepest wings relative to average, while the right bottom panel has the widest wings.

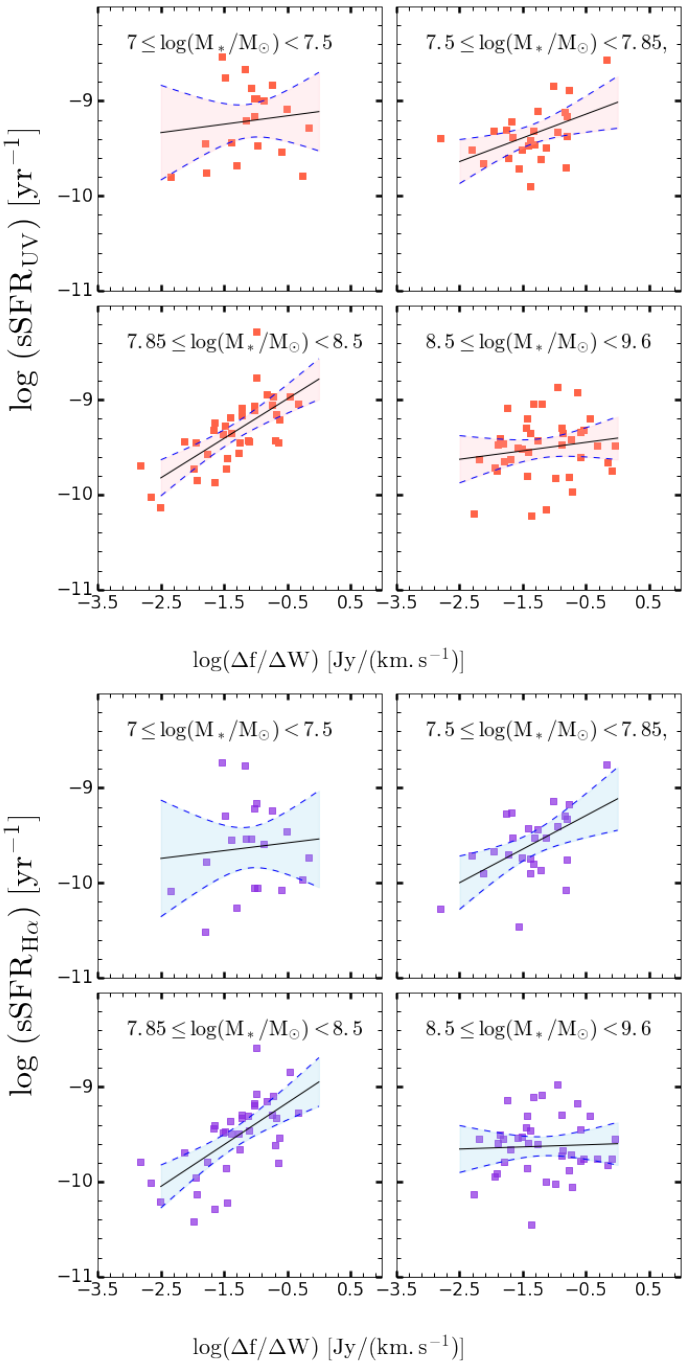

Figure 4.6: Top: Log(sSFR$_{UV}$) vs. log($\Delta f/\Delta W$). A linear fit and 68% confidence region are shown as black lines and pink shaded areas. There is a clear positive correlation at $10^{7.5} \leq \mathrm{M}_* < 10^{8.5}$ M$_\odot$ which disappears at larger masses. This is an evidence that bursty star formation can cause a line broadening (i.e. gas velocity variation) in low-mass galaxies. Bottom: Log(sSFR$_{H\alpha}$) vs. log($\Delta f/\Delta W$). Again we see that there is a steep slope at the two intermediate mass bins which becomes shallower towards larger masses. However, the scatter seen here is relatively larger compared to the top panel.

this scenario, the longevity of these outflows has to be shorter than the timescale which takes UV to rise since the star formation burst. McQuinn et al. (2018) have also found that the longevity of outflows for a few local starburst galaxies is at most 25 Myr which supports the assumption that perhaps the lifetime of outflows is shorter or at most the same as the UV response to the burstiness ($\sim$ 20 Myrs). On the other hand, when UV is low, the star formation has been turned off 20 Myrs ago and since then galaxy has started accreting gas and stars and resuming star formation resulting in a galaxy contraction. Right after the first Myrs of star formation, the first populations of SNe have blown out and kicked gas out of the galaxy, causing a large gas velocity dispersion.

It is also worth noting that both $H\alpha$ and UV luminosities indicate similar correlations despite that $H\alpha$ shows larger scatter than UV. We also plan to compare our results with the simulation and will investigate the similarities or discrepancies between observation and simulation for the rest of this project.

There are also few studies investigating the effect of bursty star formation on the gas velocity dispersion at higher redshifts. Hirtenstein et al. (2019) studied this effect for a sample of gravitationally lensed galaxies at z$\sim$2 using the Hα spatially resolved spectroscopy from OSIRIS/Keck. The stellar masses range from 10^8 to $10^{9.8} M_{\odot}$. They found a correlation between the sSFR and the Hα gas velocity dispersion at fixed mass, more specifically at mass ranges above $10^9 M_{\odot}$.

Even though we found correlations between the star formation rates and kinematics of stars and gas in our local dwarf sample, our findings indicate the opposite of what simulations predict. Based on El-Badry et al. (2016), the star formation rate is expected to

be negatively correlated with the galaxy size and positively correlated with the gas velocity dispersion. Such that at a star formation burst, galaxy should be at its minimum size and gas velocity should be largely dispersed. However what we found is the opposite of this, such that the star formation is positively correlated with the galaxy size and negatively correlated with the gas velocity dispersion. In order to find out the answer to this, we need to better understand the spatial scale and timescale at which the outflows start to impact the gas and star kinematics, more specifically for how long after a burst of star formation and how far from the center of the outflows they become important? Answers to these questions will allow us to disentangle the inconsistencies seen between the observations and simulations and to eventually determine the relevance of implementing baryonic feedback into the hydrodynamical simulations in order to address the challenges introduced to the current cosmological models.

Bibliography

Anahita Alavi, Brian Siana, Johan Richard, Daniel P. Stark, Claudia Scarlata, Harry I. Teplitz, William R. Freeman, Alberto Dominguez, Marc Rafelski, Brant Robertson, and Lisa Kewley. Ultra-faint Ultraviolet Galaxies at z ˜2 behind the Lensing Cluster A1689: The Luminosity Function, Dust Extinction, and Star Formation Rate Density. , 780:143, January 2014. doi: 10.1088/0004-637X/780/2/143.

Anahita Alavi, Brian Siana, Johan Richard, Marc Rafelski, Mathilde Jauzac, Marceau Limousin, William R. Freeman, Claudia Scarlata, Brant Robertson, Daniel P. Stark, Harry I. Teplitz, and Vandana Desai. The Evolution of the Faint End of the UV Luminosity Function during the Peak Epoch of Star Formation (1 < z < 3). , 832:56, November 2016. doi: 10.3847/0004-637X/832/1/56.

Lauren Anderson, F. Governato, M. Karcher, T. Quinn, and J. Wadsley. The little Galaxies that could (reionize the universe): predicting faint end slopes & escape fractions at z>4. , 468:4077–4092, July 2017. doi: 10.1093/mnras/stx709.

B. H. Andrews and P. Martini. The Mass-Metallicity Relation with the Direct Method on Stacked Spectra of SDSS Galaxies. , 765:140, March 2013. doi: 10.1088/0004-637X/765/2/140.

J. E. Andrews, D. Calzetti, R. Chandar, J. C. Lee, B. G. Elmegreen, R. C. Kennicutt, B. Whitmore, J. S. Kissel, Robert L. da Silva, Mark R. Krumholz, R. W. O'Connell, M. A. Dopita, Jay A. Frogel, and Hwihyun Kim. An Initial Mass Function Study of the Dwarf Starburst Galaxy NGC 4214. , 767:51, April 2013. doi: 10.1088/0004-637X/767/1/51.

J. E. Andrews, D. Calzetti, R. Chandar, B. G. Elmegreen, R. C. Kennicutt, Hwihyun Kim, Mark R. Krumholz, J. C. Lee, Sean McElwee, R. W. O'Connell, and B. Whitmore. Big Fish in Small Ponds: Massive Stars in the Low-mass Clusters of M83. , 793:4, September 2014. doi: 10.1088/0004-637X/793/1/4.

D. Anglés-Alcázar, C.-A. Faucher-Giguère, D. Kereš, P. F. Hopkins, E. Quataert, and N. Murray. The Cosmic Baryon Cycle and Galaxy Mass Assembly in the FIRE Simulations. *ArXiv e-prints*, October 2016.

Hakim Atek, Johan Richard, Jean-Paul Kneib, Mathilde Jauzac, Daniel Schaerer, Benjamin Clement, Marceau Limousin, Eric Jullo, Priyamvada Natarajan, Eiichi Egami, and Harald Ebeling. New Constraints on the Faint End of the UV Luminosity Function at z ~7-8 Using the Gravitational Lensing of the Hubble Frontier Fields Cluster A2744. , 800(1): 18, Feb 2015. doi: 10.1088/0004-637X/800/1/18.

P. S. Behroozi, R. H. Wechsler, and C. Conroy. The Average Star Formation Histories of Galaxies in Dark Matter Halos from z = 0-8. , 770:57, June 2013. doi: 10.1088/0004-637X/770/1/57.

Peter Behroozi, Risa Wechsler, Andrew Hearin, and Charlie Conroy. UniverseMachine: The Correlation between Galaxy Growth and Dark Matter Halo Assembly from z=0-10. *ArXiv e-prints*, art. arXiv:1806.07893, June 2018.

E. F. Bell and R. C. Kennicutt, Jr. A Comparison of Ultraviolet Imaging Telescope Far-Ultraviolet and Hα Star Formation Rates. , 548:681–693, February 2001. doi: 10.1086/319025.

Danielle A. Berg, Evan D. Skillman, Andrew R. Marble, Liese van Zee, Charles W. Engelbracht, Janice C. Lee, Jr. Kennicutt, Robert C., Daniela Calzetti, Daniel A. Dale, and Benjamin D. Johnson. Direct Oxygen Abundances for Low-luminosity LVL Galaxies. , 754:98, August 2012. doi: 10.1088/0004-637X/754/2/98.

G. Bertelli, A. Bressan, C. Chiosi, F. Fagotto, and E. Nasi. Theoretical isochrones from models with new radiative opacities. , 106:275–302, August 1994.

E. Bertin and S. Arnouts. SExtractor: Software for source extraction. , 117:393–404, June 1996a. doi: 10.1051/aas:1996164.

E. Bertin and S. Arnouts. SExtractor: Software for source extraction. , 117:393–404, June 1996b. doi: 10.1051/aas:1996164.

J. Bicker and U. Fritze-v. Alvensleben. Metallicity dependent calibrations of flux based SFR tracers. , 443:L19–L23, December 2005. doi: 10.1051/0004-6361:200500194.

A. Boselli, S. Boissier, L. Cortese, V. Buat, T. M. Hughes, and G. Gavazzi. High-mass Star Formation in Normal Late-type Galaxies: Observational Constraints to the Initial Mass Function. , 706:1527–1544, December 2009. doi: 10.1088/0004-637X/706/2/1527.

R. J. Bouwens, G. D. Illingworth, P. A. Oesch, M. Trenti, I. Labbé, M. Franx, M. Stiavelli, C. M. Carollo, P. van Dokkum, and D. Magee. Lower-luminosity Galaxies Could Reionize the Universe: Very Steep Faint-end Slopes to the UV Luminosity Functions at z >= 5-8 from the HUDF09 WFC3/IR Observations. , 752(1):L5, Jun 2012. doi: 10.1088/2041-8205/752/1/L5.

R. J. Bouwens, G. D. Illingworth, P. A. Oesch, J. Caruana, B. Holwerda, R. Smit, and S. Wilkins. Reionization After Planck: The Derived Growth of the Cosmic Ionizing Emissivity Now Matches the Growth of the Galaxy UV Luminosity Density. , 811:140, October 2015a. doi: 10.1088/0004-637X/811/2/140.

R. J. Bouwens, G. D. Illingworth, P. A. Oesch, J. Caruana, B. Holwerda, R. Smit, and S. Wilkins. Reionization After Planck: The Derived Growth of the Cosmic Ionizing Emissivity Now Matches the Growth of the Galaxy UV Luminosity Density. , 811:140, October 2015b. doi: 10.1088/0004-637X/811/2/140.

R. J. Bouwens, R. Smit, I. Labbé, M. Franx, J. Caruana, P. Oesch, M. Stefanon, and N. Rasappu. The Lyman-Continuum Photon Production Efficiency ξ_{ion} of z 4-5 Galaxies from IRAC-based Hα Measurements: Implications for the Escape Fraction and Cosmic Reionization. , 831:176, November 2016a. doi: 10.3847/0004-637X/831/2/176.

Rychard J. Bouwens, Manuel Aravena, Roberto Decarli, Fabian Walter, Elisabete da Cunha, Ivo Labbé, Franz E. Bauer, Frank Bertoldi, Chris Carilli, Scott Chapman, Emanuele Daddi, Jacqueline Hodge, Rob J. Ivison, Alex Karim, Olivier Le Fevre, Benjamin Magnelli, Kazuaki Ota, Dominik Riechers, Ian R. Smail, Paul van der Werf, Axel Weiss, Pierre Cox, David Elbaz, Jorge Gonzalez-Lopez, Leopoldo Infante, Pascal Oesch, Jeff Wagg, and Steve Wilkins. ALMA Spectroscopic Survey in the Hubble Ultra Deep Field: The Infrared Excess of UV-Selected z = 2-10 Galaxies as a Function of UV- Continuum Slope and Stellar Mass. , 833:72, December 2016b. doi: 10.3847/1538-4357/833/1/72.

Jeremy D. Bradford, Marla C. Geha, and Michael R. Blanton. A Study in Blue: The Baryon Content of Isolated Low-mass Galaxies. , 809(2):146, Aug 2015. doi: 10.1088/0004-637X/809/2/146.

A. Bressan, F. Fagotto, G. Bertelli, and C. Chiosi. Evolutionary sequences of stellar models with new radiative opacities. II - Z = 0.02. , 100:647–664, September 1993.

G. Bruzual and S. Charlot. Stellar population synthesis at the resolution of 2003. , 344: 1000–1028, October 2003. doi: 10.1046/j.1365-8711.2003.06897.x.

G. Bruzual and S. Charlot. Stellar population synthesis at the resolution of 2003. *Monthly Notices of the Royal Astronomical Society*, 344(4):1000, 2003. doi: 10.1046/j.1365-8711.2003.06897.x. URL + http://dx.doi.org/10.1046/j.1365-8711.2003.06897.x.

Daniela Calzetti, Lee Armus, Ralph C. Bohlin, Anne L. Kinney, Jan Koornneef, and Thaisa Storchi-Bergmann. The Dust Content and Opacity of Actively Star-forming Galaxies. , 533:682–695, April 2000. doi: 10.1086/308692.

P. L. Capak, C. Carilli, G. Jones, C. M. Casey, D. Riechers, K. Sheth, C. M. Carollo, O. Ilbert, A. Karim, O. Lefevre, S. Lilly, N. Scoville, V. Smolcic, and L. Yan. Galaxies at redshifts 5 to 6 with systematically low dust content and high [C II] emission. , 522: 455–458, June 2015. doi: 10.1038/nature14500.

J. A. Cardelli, G. C. Clayton, and J. S. Mathis. The relationship between infrared, optical, and ultraviolet extinction. , 345:245–256, October 1989. doi: 10.1086/167900.

G. Chabrier. Galactic Stellar and Substellar Initial Mass Function. , 115:763–795, July 2003. doi: 10.1086/376392.

Jacopo Chevallard, Stéphane Charlot, Peter Senchyna, Daniel P. Stark, Alba Vidal-García, Anna Feltre, Julia Gutkin, Tucker Jones, Ramesh Mainali, and Aida Wofford. Physical properties and H-ionizing-photon production rates of extreme nearby star-forming regions. , 479:3264–3273, Sep 2018. doi: 10.1093/mnras/sty1461.

Jieun Choi, Charlie Conroy, and Nell Byler. The Evolution and Properties of Rotating Massive Star Populations. , 838:159, April 2017. doi: 10.3847/1538-4357/aa679f.

Charlie Conroy. Modeling the Panchromatic Spectral Energy Distributions of Galaxies. *Annual Review of Astronomy and Astrophysics*, 51:393–455, August 2013. doi: 10.1146/annurev-astro-082812-141017.

David O. Cook, Daniel A. Dale, Benjamin D. Johnson, Liese Van Zee, Janice C. Lee, Robert C. Kennicutt, Daniela Calzetti, Shawn M. Staudaher, and Charles W. Engelbracht. The Spitzer Local Volume Legacy (LVL) global optical photometry. , 445(1): 881–889, Nov 2014. doi: 10.1093/mnras/stu1580.

R. L. da Silva, M. Fumagalli, and M. Krumholz. SLUGStochastically Lighting Up Galaxies. I. Methods and Validating Tests. , 745:145, February 2012. doi: 10.1088/0004-637X/745/2/145.

R. L. da Silva, M. Fumagalli, and M. R. Krumholz. SLUG - Stochastically Lighting Up Galaxies - II. Quantifying the effects of stochasticity on star formation rate indicators. , 444:3275–3287, November 2014. doi: 10.1093/mnras/stu1688.

D. A. Dale, S. A. Cohen, L. C. Johnson, M. D. Schuster, D. Calzetti, C. W. Engelbracht, A. Gil de Paz, R. C. Kennicutt, J. C. Lee, A. Begum, M. Block, J. J. Dalcanton, J. G. Funes, K. D. Gordon, B. D. Johnson, A. R. Marble, S. Sakai, E. D. Skillman, L. van Zee, F. Walter, D. R. Weisz, B. Williams, S. Y. Wu, and Y. Wu. The Spitzer Local Volume Legacy: Survey Description and Infrared Photometry. , 703(1):517–556, Sep 2009. doi: 10.1088/0004-637X/703/1/517.

Roelof S. de Jong and Cedric Lacey. The Local Space Density of SB-SDM Galaxies as Function of Their Scale Size, Surface Brightness, and Luminosity. , 545:781–797, December 2000. doi: 10.1086/317840.

A. Domínguez, B. Siana, A. M. Brooks, C. R. Christensen, G. Bruzual, D. P. Stark, and A. Alavi. Consequences of bursty star formation on galaxy observables at high redshifts. , 451:839–848, July 2015. doi: 10.1093/mnras/stv1001.

K. Duncan and C. J. Conselice. Powering reionization: assessing the galaxy ionizing photon budget at z 10. , 451:2030–2049, August 2015a. doi: 10.1093/mnras/stv1049.

Kenneth Duncan and Christopher J. Conselice. Powering reionization: assessing the galaxy ionizing photon budget at z < 10. , 451:2030–2049, August 2015b. doi: 10.1093/mnras/stv1049.

K. El-Badry, E. Quataert, A. Wetzel, P. F. Hopkins, D. R. Weisz, T. K. Chan, A. Fitts, M. Boylan-Kolchin, D. Kereš, C.-A. Faucher-Giguère, and S. Garrison-Kimmel. Gas kinematics, morphology and angular momentum in the FIRE simulations. , 473:1930–1955, January 2018a. doi: 10.1093/mnras/stx2482.

Kareem El-Badry, Andrew Wetzel, Marla Geha, Philip F. Hopkins, Dusan Kereš, T. K. Chan, and Claude-André Faucher-Giguère. Breathing FIRE: How Stellar Feedback Drives Radial Migration, Rapid Size Fluctuations, and Population Gradients in Low-mass Galaxies. , 820(2):131, Apr 2016. doi: 10.3847/0004-637X/820/2/131.

Kareem El-Badry, Andrew R. Wetzel, Marla Geha, Eliot Quataert, Philip F. Hopkins, Dusan Kereš, T. K. Chan, and Claude-André Faucher-Giguère. When the Jeans Do Not Fit: How Stellar Feedback Drives Stellar Kinematics and Complicates Dynamical Modeling in Low-mass Galaxies. , 835(2):193, Feb 2017. doi: 10.3847/1538-4357/835/2/193.

Kareem El-Badry, Jeremy Bradford, Eliot Quataert, Marla Geha, Michael Boylan-Kolchin, Daniel R. Weisz, Andrew Wetzel, Philip F. Hopkins, T. K. Chan, Alex Fitts, Dušan Kereš, and Claude-André Faucher-Giguère. Gas kinematics in FIRE simulated galaxies compared to spatially unresolved H I observations. , 477(2):1536–1548, Jun 2018b. doi: 10.1093/mnras/sty730.

J. J. Eldridge. Stochasticity, a variable stellar upper mass limit, binaries and star formation rate indicators. , 422:794–803, May 2012. doi: 10.1111/j.1365-2966.2012.20662.x.

J. J. Eldridge, E. R. Stanway, L. Xiao, L. A. S. McClelland, G. Taylor, M. Ng, S. M. L. Greis, and J. C. Bray. Binary Population and Spectral Synthesis Version 2.1: Construction, Observational Verification, and New Results. *Publications of the Astronomical Society of Australia*, 34:e058, November 2017. doi: 10.1017/pasa.2017.51.

Najmeh Emami, Brian Siana, Daniel R. Weisz, and Benjamin D. Johnson. A Closer look at Bursty Star Formation with L_{H} and L_{UV} Distributions. *ArXiv e-prints*, art. arXiv:1809.06380, September 2018.

D. K. Erb, A. E. Shapley, M. Pettini, C. C. Steidel, N. A. Reddy, and K. L. Adelberger. The Mass-Metallicity Relation at z˜2. , 644:813–828, June 2006. doi: 10.1086/503623.

Dawn K. Erb. Feedback in low-mass galaxies in the early Universe. , 523:169–176, July 2015. doi: 10.1038/nature14454.

F. Fagotto, A. Bressan, G. Bertelli, and C. Chiosi. Evolutionary sequences of stellar models with new radiative opacities. IV. Z=0.004 and Z=0.008. , 105:29–38, May 1994.

S. M. Fall, R. Chandar, and B. C. Whitmore. New Tests for Disruption Mechanisms of Star Clusters: Methods and Application to the Antennae Galaxies. , 704:453–468, October 2009. doi: 10.1088/0004-637X/704/1/453.

Steven L. Finkelstein, Jr. Ryan, Russell E., Casey Papovich, Mark Dickinson, Mimi Song, Rachel S. Somerville, Henry C. Ferguson, Brett Salmon, Mauro Giavalisco, Anton M. Koekemoer, Matthew L. N. Ashby, Peter Behroozi, Marco Castellano, James S. Dunlop, Sandy M. Faber, Giovanni G. Fazio, Adriano Fontana, Norman A. Grogin, Nimish Hathi, Jason Jaacks, Dale D. Kocevski, Rachael Livermore, Ross J. McLure, Emiliano Merlin, Bahram Mobasher, Jeffrey A. Newman, Marc Rafelski, Vithal Tilvi, and S. P. Willner. The Evolution of the Galaxy Rest-frame Ultraviolet Luminosity Function over the First Two Billion Years. , 810(1):71, Sep 2015. doi: 10.1088/0004-637X/810/1/71.

Alex Fitts, Michael Boylan-Kolchin, James S. Bullock, Daniel R. Weisz, Kareem El-Badry, Coral Wheeler, Claude-André Faucher-Giguère, Eliot Quataert, Philip F. Hopkins, Dušan Kereš, Andrew Wetzel, and Christopher C. Hayward. No assembly required: mergers are mostly irrelevant for the growth of low-mass dwarf galaxies. , 479:319–331, Sep 2018. doi: 10.1093/mnras/sty1488.

Daniel Foreman-Mackey, David W. Hogg, Dustin Lang, and Jonathan Goodman. emcee: The MCMC Hammer. , 125(925):306, Mar 2013. doi: 10.1086/670067.

William R. Freeman, Brian Siana, Mariska Kriek, Alice E. Shapley, Naveen Reddy, Alison L. Coil, Bahram Mobasher, Alexander L. Muratov, Mojegan Azadi, Gene Leung, Ryan Sanders, Irene Shivaei, Sedona H. Price, Laura DeGroot, and Dušan Kereš. The MOSDEF Survey: Broad Emission Lines at z=1.4-3.8. *ArXiv e-prints*, art. arXiv:1710.03230, October 2017.

M. Fumagalli, R. L. da Silva, and M. R. Krumholz. Stochastic Star Formation and a (Nearly) Uniform Stellar Initial Mass Function. , 741:L26, November 2011. doi: 10.1088/2041-8205/741/2/L26.

Timothy Gburek, Brian Siana, Anahita Alavi, Najmeh Emami, Johan Richard, William R. Freeman, Daniel P. Stark, Christopher Snapp-Kolas, and Breanna Lucero. The Detection of [O III]λ4363 in a Lensed, Dwarf Galaxy at z=2.59: Testing Metallicity Indicators and Scaling Relations at High Redshift and Low Mass. *arXiv e-prints*, art. arXiv:1906.11849, Jun 2019.

K. Glazebrook, C. Blake, F. Economou, S. Lilly, and M. Colless. Measurement of the star formation rate from Hα in field galaxies at z=1. , 306:843–856, July 1999. doi: 10.1046/j.1365-8711.1999.02576.x.

Karl D. Gordon, Geoffrey C. Clayton, K. A. Misselt, Arlo U. Landolt, and Michael J. Wolff. A Quantitative Comparison of the Small Magellanic Cloud, Large Magellanic Cloud, and Milky Way Ultraviolet to Near-Infrared Extinction Curves. , 594:279–293, September

2003. doi: 10.1086/376774.

F. Governato, C. Brook, L. Mayer, A. Brooks, G. Rhee, J. Wadsley, P. Jonsson, B. Willman, G. Stinson, T. Quinn, and P. Madau. Bulgeless dwarf galaxies and dark matter cores from supernova-driven outflows. , 463:203–206, January 2010. doi: 10.1038/nature08640.

F. Governato, A. Zolotov, A. Pontzen, C. Christensen, S. H. Oh, A. M. Brooks, T. Quinn, S. Shen, and J. Wadsley. Cuspy no more: how outflows affect the central dark matter and baryon distribution in Λ cold dark matter galaxies. , 422:1231–1240, May 2012. doi: 10.1111/j.1365-2966.2012.20696.x.

Y. Guo, M. Rafelski, S. M. Faber, D. C. Koo, M. R. Krumholz, J. R. Trump, S. P. Willner, R. Amorín, G. Barro, E. F. Bell, J. P. Gardner, E. Gawiser, N. P. Hathi, A. M. Koekemoer, C. Pacifici, P. G. Pérez-González, S. Ravindranath, N. Reddy, H. I. Teplitz, and H. Yesuf. The Bursty Star Formation Histories of Low-mass Galaxies at 0.4 z 1 Revealed by Star Formation Rates Measured From Hβ and FUV. , 833:37, December 2016a. doi: 10.3847/1538-4357/833/1/37.

Y. Guo, M. Rafelski, S. M. Faber, D. C. Koo, M. R. Krumholz, J. R. Trump, S. P. Willner, R. Amorín, G. Barro, E. F. Bell, J. P. Gardner, E. Gawiser, N. P. Hathi, A. M. Koekemoer, C. Pacifici, P. G. Pérez-González, S. Ravindranath, N. Reddy, H. I. Teplitz, and H. Yesuf. The Bursty Star Formation Histories of Low-mass Galaxies at 0.4 z 1 Revealed by Star Formation Rates Measured From Hβ and FUV. , 833:37, December 2016b. doi: 10.3847/1538-4357/833/1/37.

C.-N. Hao, R. C. Kennicutt, B. D. Johnson, D. Calzetti, D. A. Dale, and J. Moustakas. Dust-corrected Star Formation Rates of Galaxies. II. Combinations of Ultraviolet and Infrared Tracers. , 741:124, November 2011. doi: 10.1088/0004-637X/741/2/124.

A. Henry, C. Scarlata, A. Domínguez, M. Malkan, C. L. Martin, B. Siana, H. Atek, A. G. Bedregal, J. W. Colbert, M. Rafelski, N. Ross, H. Teplitz, A. J. Bunker, A. Dressler, N. Hathi, D. Masters, P. McCarthy, and A. Straughn. Low Masses and High Redshifts: The Evolution of the Mass-Metallicity Relation. , 776:L27, October 2013. doi: 10.1088/2041-8205/776/2/L27.

Alaina Henry, Claudia Scarlata, Crystal L. Martin, and Dawn Erb. Lyα Emission from Green Peas: The Role of Circumgalactic Gas Density, Covering, and Kinematics. , 809: 19, August 2015. doi: 10.1088/0004-637X/809/1/19.

Jessie Hirtenstein, Tucker Jones, Xin Wang, Andrew Wetzel, Kareem El-Badry, Austin Hoag, Tommaso Treu, Maruša Bradač, and Takahiro Morishita. The OSIRIS Lens-amplified Survey (OLAS). I. Dynamical Effects of Stellar Feedback in Low-mass Galaxies at z$\sim$2. , 880(1):54, Jul 2019. doi: 10.3847/1538-4357/ab113e.

P. F. Hopkins, D. Kereš, J. Oñorbe, C.-A. Faucher-Giguère, E. Quataert, N. Murray, and J. S. Bullock. Galaxies on FIRE (Feedback In Realistic Environments): stellar feedback explains cosmologically inefficient star formation. , 445:581–603, November 2014. doi:

10.1093/mnras/stu1738.

Philip F. Hopkins, Andrew Wetzel, Dušan Kereš, Claude-André Faucher-Giguère, Eliot Quataert, Michael Boylan-Kolchin, Norman Murray, Christopher C. Hayward, Shea Garrison-Kimmel, Cameron Hummels, Robert Feldmann, Paul Torrey, Xiangcheng Ma, Daniel Anglés-Alcázar, Kung-Yi Su, Matthew Orr, Denise Schmitz, Ivanna Escala, Robyn Sanderson, Michael Y. Grudić, Zachary Hafen, Ji-Hoon Kim, Alex Fitts, James S. Bullock, Coral Wheeler, T. K. Chan, Oliver D. Elbert, and Desika Narayanan. FIRE-2 simulations: physics versus numerics in galaxy formation. , 480:800–863, October 2018. doi: 10.1093/mnras/sty1690.

Erik A. Hoversten and Karl Glazebrook. Evidence for a Nonuniversal Stellar Initial Mass Function from the Integrated Properties of SDSS Galaxies. , 675:163–187, March 2008. doi: 10.1086/524095.

W. K. Huchtmeier and O. G. Richter. HI-observations of galaxies in the Kraan-Korteweg - Tammann catalogue of nearby galaxies. I - The data. *Astronomy and Astrophysics Supplement Series*, 63:323, Feb 1986.

J. Iglesias-Páramo, A. Boselli, G. Gavazzi, and A. Zaccardo. Tracing the star formation history of cluster galaxies using the Hα/UV flux ratio. , 421:887–897, July 2004. doi: 10.1051/0004-6361:20034572.

Y. I. Izotov, G. Worseck, D. Schaerer, N. G. Guseva, T. X. Thuan, A. Fricke, Verhamme, and I. Orlitová. Low-redshift Lyman continuum leaking galaxies with high [O III]/[O II] ratios. , 478:4851–4865, August 2018. doi: 10.1093/mnras/sty1378.

M. Jauzac, J. Richard, M. Limousin, K. Knowles, G. Mahler, G. P. Smith, J. P. Kneib, E. Jullo, P. Natarajan, H. Ebeling, H. Atek, B. Clément, D. Eckert, E. Egami, R. Massey, and M. Rexroth. Hubble Frontier Fields: predictions for the return of SN Refsdal with the MUSE and GMOS spectrographs. , 457:2029–2042, April 2016. doi: 10.1093/mnras/stw069.

W. Karman, K. I. Caputi, G. B. Caminha, M. Gronke, C. Grillo, I. Balestra, P. Rosati, E. Vanzella, D. Coe, M. Dijkstra, A. M. Koekemoer, D. McLeod, A. Mercurio, and M. Nonino. MUSE integral-field spectroscopy towards the Frontier Fields cluster Abell S1063. II. Properties of low luminosity Lyman α emitters at z > 3. , 599:A28, March 2017. doi: 10.1051/0004-6361/201629055.

G. Kauffmann. Quantitative constraints on starburst cycles in galaxies with stellar masses in the range 10^8-10^{10} M. , 441:2717–2724, July 2014. doi: 10.1093/mnras/stu752.

Jr. Kennicutt, Robert C., Janice C. Lee, José G. Funes, S. J., Shoko Sakai, and Sanae Akiyama. An Hα Imaging Survey of Galaxies in the Local 11 Mpc Volume. *The Astrophysical Journal Supplement Series*, 178:247–279, October 2008. doi: 10.1086/590058.

R. C. Kennicutt, Jr. Star Formation in Galaxies Along the Hubble Sequence. , 36:189–232, 1998. doi: 10.1146/annurev.astro.36.1.189.

R. C. Kennicutt, Jr., P. Tamblyn, and C. E. Congdon. Past and future star formation in disk galaxies. , 435:22–36, November 1994. doi: 10.1086/174790.

R. C. Kennicutt, Jr., C.-N. Hao, D. Calzetti, J. Moustakas, D. A. Dale, G. Bendo, C. W. Engelbracht, B. D. Johnson, and J. C. Lee. Dust-corrected Star Formation Rates of Galaxies. I. Combinations of Hα and Infrared Tracers. , 703:1672-1695, October 2009. doi: 10.1088/0004-637X/703/2/1672.

Robert C. Kennicutt and Neal J. Evans. Star Formation in the Milky Way and Nearby Galaxies. *Annual Review of Astronomy and Astrophysics*, 50:531–608, September 2012. doi: 10.1146/annurev-astro-081811-125610.

Dušan Kereš, Neal Katz, Romeel Davé, Mark Fardal, and David H. Weinberg. Galaxies in a simulated ΛCDM universe - II. Observable properties and constraints on feedback. , 396:2332–2344, July 2009. doi: 10.1111/j.1365-2966.2009.14924.x.

L. J. Kewley and S. L. Ellison. Metallicity Calibrations and the Mass-Metallicity Relation for Star-forming Galaxies. , 681:1183–1204, July 2008. doi: 10.1086/587500.

Lisa J. Kewley, Margaret J. Geller, Rolf A. Jansen, and Michael A. Dopita. The Hα and Infrared Star Formation Rates for the Nearby Field Galaxy Survey. , 124:3135–3143, December 2002. doi: 10.1086/344487.

Evan N. Kirby, Judith. G. Cohen, Graeme H. Smith, Steven R. Majewski, Sangmo Tony Sohn, and Puragra Guhathakurta. Multi-element Abundance Measurements from Medium-resolution Spectra. IV. Alpha Element Distributions in Milky Way Satellite Galaxies. , 727:79, February 2011. doi: 10.1088/0004-637X/727/2/79.

Mariska Kriek, Pieter G. van Dokkum, Ivo Labbé, Marijn Franx, Garth D. Illingworth, Danilo Marchesini, and Ryan F. Quadri. An Ultra-Deep Near-Infrared Spectrum of a Compact Quiescent Galaxy at z = 2.2. , 700:221–231, July 2009. doi: 10.1088/0004-637X/700/1/221.

Mariska Kriek, Alice E. Shapley, Naveen A. Reddy, Brian Siana, Alison L. Coil, Bahram Mobasher, William R. Freeman, Laura de Groot, Sedona H. Price, Ryan Sanders, Irene Shivaei, Gabriel B. Brammer, Ivelina G. Momcheva, Rosalind E. Skelton, Pieter G. van Dokkum, Katherine E. Whitaker, James Aird, Mojegan Azadi, Marc Kassis, James S. Bullock, Charlie Conroy, Romeel Dav, Duan Kere, and Mark Krumholz. The mosfire deep evolution field (mosdef) survey: Rest-frame optical spectroscopy for 1500 h-selected galaxies at 1.37 z 3.8. *The Astrophysical Journal Supplement Series*, 218(2):15, 2015. URL `http://stacks.iop.org/0067-0049/218/i=2/a=15`.

P. Kroupa and C. Weidner. Galactic-Field Initial Mass Functions of Massive Stars. , 598:

1076–1078, December 2003. doi: 10.1086/379105.

H. Krueger, U. Fritze-v. Alvensleben, and H.-H. Loose. Optical and near infrared spectral energy distributions. of blue compact galaxies from evolutionary synthesis. , 303:41, November 1995.

C. J. Lada and E. A. Lada. Embedded Clusters in Molecular Clouds. , 41:57–115, 2003. doi: 10.1146/annurev.astro.41.011802.094844.

Daniel Lam, Rychard J. Bouwens, Ivo Labbe, Joop Schaye, Kasper B. Schmidt, Michael V. Maseda, Roland Bacon, Leindert A. Boogaard, Themiya Nanayakkara, Johan Richard, Guillaume Mahler, and Tanya Urrutia. The mean H$$ EW and Lyman-continuum photon production efficiency for faint $z4-5$ galaxies. *arXiv e-prints*, art. arXiv:1902.02786, Feb 2019.

J. B. Lamb, M. S. Oey, J. K. Werk, and L. D. Ingleby. The Sparsest Clusters with O Stars. , 725:1886–1902, December 2010. doi: 10.1088/0004-637X/725/2/1886.

G. A. Lanfranchi and F. Matteucci. The predicted metallicity distribution of stars in dwarf spheroidal galaxies. , 351:1338–1348, July 2004. doi: 10.1111/j.1365-2966.2004.07877.x.

Janice C. Lee, Armando Gil de Paz, Christy Tremonti, Jr. Kennicutt, Robert C., Samir Salim, Matthew Bothwell, Daniela Calzetti, Julianne Dalcanton, Daniel Dale, Chad Engelbracht, S. J. José G. Funes, Benjamin Johnson, Shoko Sakai, Evan Skillman, Liese van Zee, Fabian Walter, and Daniel Weisz. Comparison of Hα and UV Star Formation Rates in the Local Volume: Systematic Discrepancies for Dwarf Galaxies. , 706:599–613, November 2009. doi: 10.1088/0004-637X/706/1/599.

Janice C. Lee, Armando Gil de Paz, Robert C. Kennicutt Jr, Matthew Bothwell, Julianne Dalcanton, Jos G. Funes S. J., Benjamin D. Johnson, Shoko Sakai, Evan Skillman, Christy Tremonti, and Liese van Zee. A galex ultraviolet imaging survey of galaxies in the local volume. *The Astrophysical Journal Supplement Series*, 192(1):6, 2011. URL `http://stacks.iop.org/0067-0049/192/i=1/a=6`.

Janice C. Lee, Sylvain Veilleux, Michael McDonald, and Bryan Hilbert. A Deeper Look at Faint Hα Emission in Nearby Dwarf Galaxies. , 817:177, February 2016. doi: 10.3847/0004-637X/817/2/177.

Claus Leitherer, Henry C. Ferguson, Timothy M. Heckman, and James D. Lowenthal. The Lyman Continuum in Starburst Galaxies Observed with the Hopkins Ultraviolet Telescope. , 454:L19, November 1995. doi: 10.1086/309760.

M. Limousin, J. Richard, E. Jullo, M. Jauzac, H. Ebeling, M. Bonamigo, A. Alavi, B. Clément, C. Giocoli, J.-P. Kneib, T. Verdugo, P. Natarajan, B. Siana, H. Atek, and M. Rexroth. Strong-lensing analysis of MACS J0717.5+3745 from Hubble Frontier Fields observations: How well can the mass distribution be constrained? , 588:A99, April 2016. doi: 10.1051/0004-6361/201527638.

Marceau Limousin, Johan Richard, Eric Jullo, Jean-Paul Kneib, Bernard Fort, Geneviève Soucail, Árdís Elíasdóttir, Priyamvada Natarajan, Richard S. Ellis, Ian Smail, Oliver Czoske, Graham P. Smith, Patrick Hudelot, Sébastien Bardeau, Harald Ebeling, Eiichi Egami, and Kirsten K. Knudsen. Combining Strong and Weak Gravitational Lensing in Abell 1689. , 668:643–666, October 2007. doi: 10.1086/521293.

Xin Liu, Alice E. Shapley, Alison L. Coil, Jarle Brinchmann, and Chung-Pei Ma. Metallicities and Physical Conditions in Star-forming Galaxies at z ˜1.0-1.5. , 678:758–779, May 2008. doi: 10.1086/529030.

R. C. Livermore, S. L. Finkelstein, and J. M. Lotz. Directly Observing the Galaxies Likely Responsible for Reionization. , 835(2):113, Feb 2017. doi: 10.3847/1538-4357/835/2/113.

P. Madau and F. Haardt. Cosmic Reionization after Planck: Could Quasars Do It All? , 813:L8, November 2015. doi: 10.1088/2041-8205/813/1/L8.

R. Maiolino, T. Nagao, A. Grazian, F. Cocchia, A. Marconi, F. Mannucci, A. Cimatti, A. Pipino, S. Ballero, F. Calura, C. Chiappini, A. Fontana, G. L. Granato, F. Matteucci, G. Pastorini, L. Pentericci, G. Risaliti, M. Salvati, and L. Silva. AMAZE. I. The evolution of the mass-metallicity relation at z 3. , 488:463–479, September 2008. doi: 10.1051/0004-6361:200809678.

Jorryt Matthee, David Sobral, Philip Best, Ali Ahmad Khostovan, Iván Oteo, Rychard Bouwens, and Huub Röttgering. The production and escape of Lyman-Continuum radiation from star-forming galaxies at z $\sim$ 2 and their redshift evolution. , 465:3637–3655, March 2017. doi: 10.1093/mnras/stw2973.

Kristen B. W. McQuinn, Evan D. Skillman, Taryn N. Heilman, Noah P. Mitchell, and Tyler Kelley. Galactic outflows, star formation histories, and time-scales in starburst dwarf galaxies from STARBIRDS. *Monthly Notices of the Royal Astronomical Society*, 477(3):3164–3177, Jul 2018. doi: 10.1093/mnras/sty839.

V. Mehta, C. Scarlata, M. Rafelski, T. Gburek, H. I. Teplitz, A. Alavi, M. Boylan-Kolchin, S. Finkelstein, J. P. Gardner, N. Grogin, A. Koekemoer, P. Kurczynski, B. Siana, A. Codoreanu, D. F. de Mello, K.-S. Lee, and E. Soto. UVUDF: UV Luminosity Functions at the Cosmic High Noon. , 838:29, March 2017. doi: 10.3847/1538-4357/aa6259.

G. R. Meurer, O. I. Wong, J. H. Kim, D. J. Hanish, T. M. Heckman, J. Werk, J. Bland-Hawthorn, M. A. Dopita, M. A. Zwaan, B. Koribalski, M. Seibert, D. A. Thilker, H. C. Ferguson, R. L. Webster, M. E. Putman, P. M. Knezek, M. T. Doyle, M. J. Drinkwater, C. G. Hoopes, V. A. Kilborn, M. Meyer, E. V. Ryan-Weber, R. C. Smith, and L. Staveley-Smith. Evidence for a Nonuniform Initial Mass Function in the Local Universe. , 695: 765–780, April 2009. doi: 10.1088/0004-637X/695/1/765.

Gerhardt R. Meurer, Timothy M. Heckman, and Daniela Calzetti. Dust Absorption and the Ultraviolet Luminosity Density at z ˜3 as Calibrated by Local Starburst Galaxies. , 521:64–80, August 1999. doi: 10.1086/307523.

B. P. Moster, R. S. Somerville, C. Maulbetsch, F. C. van den Bosch, A. V. Macciò, T. Naab, and L. Oser. Constraints on the Relationship between Stellar Mass and Halo Mass at Low and High Redshift. , 710:903–923, February 2010. doi: 10.1088/0004-637X/710/2/903.

A. L. Muratov, D. Kereš, C.-A. Faucher-Giguère, P. F. Hopkins, E. Quataert, and N. Murray. Gusty, gaseous flows of FIRE: galactic winds in cosmological simulations with explicit stellar feedback. , 454:2691–2713, December 2015. doi: 10.1093/mnras/stv2126.

Kimihiko Nakajima, Richard S. Ellis, Ikuru Iwata, Akio K. Inoue, Haruka Kusakabe, Masami Ouchi, and Brant E. Robertson. A Hard Ionizing Spectrum in z = 3-4 Lyα Emitters with Intense [O III] Emission: Analogs of Galaxies in the Reionization Era? , 831:L9, November 2016. doi: 10.3847/2041-8205/831/1/L9.

J. B. Oke and J. E. Gunn. Secondary standard stars for absolute spectrophotometry. , 266: 713–717, Mar 1983. doi: 10.1086/160817.

D. E. Osterbrock and G. J. Ferland. Astrophysics of gaseous nebulae and active galactic nuclei. 2006.

J. P. Paardekooper, S. Khochfar, and C. V. Dalla. The first billion years project: protogalaxies reionizing the universe. , 429:L94–L98, Feb 2013. doi: 10.1093/mnrasl/sls032.

Jan-Pieter Paardekooper, Sadegh Khochfar, and Claudio Dalla Vecchia. The First Billion Years project: the escape fraction of ionizing photons in the epoch of reionization. , 451: 2544–2563, August 2015. doi: 10.1093/mnras/stv1114.

M. Pannella, C. L. Carilli, E. Daddi, H. J. McCracken, F. N. Owen, A. Renzini, V. Strazzullo, F. Civano, A. M. Koekemoer, E. Schinnerer, N. Scoville, V. Smolčić, Y. Taniguchi, H. Aussel, J. P. Kneib, O. Ilbert, Y. Mellier, M. Salvato, D. Thompson, and C. J. Willott. Star Formation and Dust Obscuration at z 2: Galaxies at the Dawn of Downsizing. , 698:L116–L120, June 2009. doi: 10.1088/0004-637X/698/2/L116.

J. Pflamm-Altenburg, C. Weidner, and P. Kroupa. Diverging UV and Hα fluxes of star-forming galaxies predicted by the IGIMF theory. , 395:394–400, May 2009. doi: 10.1111/j.1365-2966.2009.14522.x.

Jan Pflamm-Altenburg, Carsten Weidner, and Pavel Kroupa. Converting h luminosities into star formation rates. *The Astrophysical Journal*, 671(2):1550, 2007. URL `http://stacks.iop.org/0004-637X/671/i=2/a=1550`.

N. A. Reddy, D. K. Erb, M. Pettini, C. C. Steidel, and A. E. Shapley. Dust Obscuration and Metallicity at High Redshift: New Inferences from UV, Hα, and 8 μm Observations of z ˜ 2 Star-forming Galaxies. , 712:1070–1091, April 2010. doi: 10.1088/0004-637X/712/2/1070.

N. A. Reddy, C. C. Steidel, M. Pettini, M. Bogosavljević, and A. E. Shapley. The Connec-

tion Between Reddening, Gas Covering Fraction, and the Escape of Ionizing Radiation at High Redshift. , 828:108, September 2016. doi: 10.3847/0004-637X/828/2/108.

Naveen A. Reddy and Charles C. Steidel. A Steep Faint-End Slope of the UV Luminosity Function at z ˜2-3: Implications for the Global Stellar Mass Density and Star Formation in Low-Mass Halos. , 692:778–803, February 2009. doi: 10.1088/0004-637X/692/1/778.

Naveen A. Reddy, Mariska Kriek, Alice E. Shapley, William R. Freeman, Brian Siana, Alison L. Coil, Bahram Mobasher, Sedona H. Price, Ryan L. Sanders, and Irene Shivaei. The MOSDEF Survey: Measurements of Balmer Decrements and the Dust Attenuation Curve at Redshifts z ˜1.4-2.6. , 806:259, June 2015. doi: 10.1088/0004-637X/806/2/259.

Naveen A. Reddy, Pascal A. Oesch, Rychard J. Bouwens, Mireia Montes, Garth D. Illingworth, Charles C. Steidel, Pieter G. van Dokkum, Hakim Atek, Marcella C. Carollo, Anna Cibinel, Brad Holden, Ivo Labbé, Dan Magee, Laura Morselli, Erica J. Nelson, and Steve Wilkins. The HDUV Survey: A Revised Assessment of the Relationship between UV Slope and Dust Attenuation for High-redshift Galaxies. , 853:56, January 2018. doi: 10.3847/1538-4357/aaa3e7.

Y. Revaz, P. Jablonka, T. Sawala, V. Hill, B. Letarte, M. Irwin, G. Battaglia, A. Helmi, M. D. Shetrone, E. Tolstoy, and K. A. Venn. The dynamical and chemical evolution of dwarf spheroidal galaxies. , 501:189–206, July 2009. doi: 10.1051/0004-6361/200911734.

B. E. Robertson, R. S. Ellis, S. R. Furlanetto, and J. S. Dunlop. Cosmic Reionization and Early Star-forming Galaxies: A Joint Analysis of New Constraints from Planck and the Hubble Space Telescope. , 802:L19, April 2015. doi: 10.1088/2041-8205/802/2/L19.

Brant E. Robertson, Steven R. Furlanetto, Evan Schneider, Stephane Charlot, Richard S. Ellis, Daniel P. Stark, Ross J. McLure, James S. Dunlop, Anton Koekemoer, Matthew A. Schenker, Masami Ouchi, Yoshiaki Ono, Emma Curtis-Lake, Alexander B. Rogers, Rebecca A. A. Bowler, and Michele Cirasuolo. New Constraints on Cosmic Reionization from the 2012 Hubble Ultra Deep Field Campaign. , 768:71, May 2013. doi: 10.1088/0004-637X/768/1/71.

Arpita Roy, Biman B. Nath, and Prateek Sharma. Narrow escape: how ionizing photons escape from disc galaxies. , 451:1939–1954, August 2015. doi: 10.1093/mnras/stv1006.

Ryan L. Sanders, Alice E. Shapley, Mariska Kriek, Naveen A. Reddy, William R. Freeman, Alison L. Coil, Brian Siana, Bahram Mobasher, Irene Shivaei, Sedona H. Price, and Laura de Groot. The MOSDEF Survey: Mass, Metallicity, and Star-formation Rate at z ˜2.3. , 799:138, February 2015. doi: 10.1088/0004-637X/799/2/138.

D. J. Schlegel, D. P. Finkbeiner, and M. Davis. Maps of Dust Infrared Emission for Use in Estimation of Reddening and Cosmic Microwave Background Radiation Foregrounds. , 500:525–553, June 1998. doi: 10.1086/305772.

A. E. Shapley, A. L. Coil, C.-P. Ma, and K. Bundy. Chemical Abundances of DEEP2 Star-forming Galaxies at z˜1.0-1.5. , 635:1006–1021, December 2005. doi: 10.1086/497630.

Alice E. Shapley, Charles C. Steidel, Max Pettini, Kurt L. Adelberger, and Dawn K. Erb. The Direct Detection of Lyman Continuum Emission from Star-forming Galaxies at z 3. , 651:688–703, November 2006. doi: 10.1086/507511.

M. D. Shetrone, M. H. Siegel, D. O. Cook, and T. Bosler. Chemical Abundances of the Leo II Dwarf Galaxy. , 137:62–71, January 2009. doi: 10.1088/0004-6256/137/1/62.

R. Shimakawa, Y. Koyama, J. X. Prochaska, Y. Guo, K.-i. Tadaki, and T. Kodama. Identification of variability in recent star formation histories of local galaxies based on Hα/UV ratio. *ArXiv e-prints*, May 2017.

I. Shivaei, N. A. Reddy, A. E. Shapley, M. Kriek, B. Siana, B. Mobasher, A. L. Coil, W. R. Freeman, R. Sanders, S. H. Price, L. de Groot, and M. Azadi. The MOSDEF Survey: Dissecting the Star Formation Rate versus Stellar Mass Relation Using Hα and Hβ Emission Lines at z $\sim 2., 815 : 98, December2015. doi : 10.1088/0004 - 637X/815/2/98$.

Irene Shivaei, Naveen A. Reddy, Alice E. Shapley, Brian Siana, Mariska Kriek, Bahram Mobasher, Alison L. Coil, William R. Freeman, Ryan L. Sanders, Sedona H. Price, Mojegan Azadi, and Tom Zick. The MOSDEF Survey: Metallicity Dependence of PAH Emission at High Redshift and Implications for 24 μm Inferred IR Luminosities and Star Formation Rates at z 2. , 837:157, March 2017. doi: 10.3847/1538-4357/aa619c.

Brian Siana, Harry I. Teplitz, James Colbert, Henry C. Ferguson, Mark Dickinson, Thomas M. Brown, Christopher J. Conselice, Duilia F. de Mello, Jonathan P. Gardner, Mauro Giavalisco, and Felipe Menanteau. New Constraints on the Lyman Continuum Escape Fraction at z˜1.3. , 668:62–73, October 2007. doi: 10.1086/521185.

Rachel S. Somerville and Joel R. Primack. Semi-analytic modelling of galaxy formation: the local Universe. , 310:1087–1110, December 1999. doi: 10.1046/j.1365-8711.1999.03032.x.

M. Sparre, C. C. Hayward, R. Feldmann, C.-A. Faucher-Giguère, A. L. Muratov, D. Kereš, and P. F. Hopkins. (Star)bursts of FIRE: observational signatures of bursty star formation in galaxies. , 466:88–104, April 2017. doi: 10.1093/mnras/stw3011.

J. S. Speagle, C. L. Steinhardt, P. L. Capak, and J. D. Silverman. A Highly Consistent Framework for the Evolution of the Star-Forming "Main Sequence" from z ˜ 0-6. , 214: 15, October 2014. doi: 10.1088/0067-0049/214/2/15.

Volker Springel and Lars Hernquist. The history of star formation in a Λ cold dark matter universe. , 339:312–334, February 2003. doi: 10.1046/j.1365-8711.2003.06207.x.

Volker Springel, Tiziana Di Matteo, and Lars Hernquist. Modelling feedback from stars

and black holes in galaxy mergers. , 361:776–794, August 2005. doi: 10.1111/j.1365-2966.2005.09238.x.

Christopher M. Springob, Martha P. Haynes, Riccardo Giovanelli, and Brian R. Kent. A Digital Archive of H I 21 Centimeter Line Spectra of Optically Targeted Galaxies. *The Astrophysical Journal Supplement Series*, 160(1):149–162, Sep 2005. doi: 10.1086/431550.

D. P. Stark, G. Walth, S. Charlot, B. Clément, A. Feltre, J. Gutkin, J. Richard, R. Mainali, B. Robertson, B. Siana, M. Tang, and M. Schenker. Spectroscopic detection of C IV λ1548 in a galaxy at z = 7.045: implications for the ionizing spectra of reionization-era galaxies. , 454:1393–1403, December 2015. doi: 10.1093/mnras/stv1907.

D. P. Stark, R. S. Ellis, S. Charlot, J. Chevallard, M. Tang, S. Belli, A. Zitrin, R. Mainali, J. Gutkin, A. Vidal-García, R. Bouwens, and P. Oesch. Lyα and C III] emission in z = 7-9 Galaxies: accelerated reionization around luminous star-forming systems? , 464: 469–479, January 2017. doi: 10.1093/mnras/stw2233.

C. C. Steidel, G. C. Rudie, A. L. Strom, M. Pettini, N. A. Reddy, A. E. Shapley, R. F. Trainor, D. K. Erb, M. L. Turner, N. P. Konidaris, K. R. Kulas, G. Mace, K. Matthews, and I. S. McLean. Strong Nebular Line Ratios in the Spectra of z ˜ 2-3 Star Forming Galaxies: First Results from KBSS-MOSFIRE. , 795:165, November 2014. doi: 10.1088/0004-637X/795/2/165.

Charles C. Steidel, Max Pettini, and Kurt L. Adelberger. Lyman-Continuum Emission from Galaxies at Z = 3.4. , 546:665–671, January 2001. doi: 10.1086/318323.

Charles C. Steidel, Allison L. Strom, Max Pettini, Gwen C. Rudie, Naveen A. Reddy, and Ryan F. Trainor. Reconciling the Stellar and Nebular Spectra of High-redshift Galaxies. , 826:159, August 2016. doi: 10.3847/0004-637X/826/2/159.

P. J. Storey and C. J. Zeippen. Theoretical values for the [OIII] 5007/4959 line-intensity ratio and homologous cases. , 312(4):813–816, Mar 2000. doi: 10.1046/j.1365-8711.2000.03184.x.

Allison L. Strom, Charles C. Steidel, Gwen C. Rudie, Ryan F. Trainor, and Max Pettini. Measuring the Physical Conditions in High-Redshift Star-Forming Galaxies: Insights from KBSS-MOSFIRE. *ArXiv e-prints*, art. arXiv:1711.08820, November 2017.

M. Sullivan, M. A. Treyer, R. S. Ellis, T. J. Bridges, B. Milliard, and J. Donas. An ultraviolet-selected galaxy redshift survey - II. The physical nature of star formation in an enlarged sample. , 312:442–464, February 2000. doi: 10.1046/j.1365-8711.2000.03140.x.

M. Sullivan, M. A. Treyer, R. S. Ellis, and B. Mobasher. An ultraviolet-selected galaxy redshift survey - III. Multicolour imaging and non-uniform star formation histories. , 350:21–34, May 2004. doi: 10.1111/j.1365-2966.2004.07649.x.

Mengtao Tang, Daniel Stark, Jacopo Chevallard, and Stéphane Charlot. MMT/MMIRS spectroscopy of $z=1.3-2.4$ extreme [OIII] emitters: Implications for galaxies in the reionization-era. *arXiv e-prints*, art. arXiv:1809.09637, Sep 2018.

W. G. Tifft and W. J. Cocke. Uncertainties in 21 centimeter Redshifts. I. Data. , 67:1, May 1988. doi: 10.1086/191265.

E. Vanzella, S. de Barros, K. Vasei, A. Alavi, M. Giavalisco, B. Siana, A. Grazian, G. Hasinger, H. Suh, N. Cappelluti, F. Vito, R. Amorin, I. Balestra, M. Brusa, F. Calura, M. Castellano, A. Comastri, A. Fontana, R. Gilli, M. Mignoli, L. Pentericci, C. Vignali, and G. Zamorani. Hubble Imaging of the Ionizing Radiation from a Star-forming Galaxy at Z=3.2 with fesc>50%. , 825:41, July 2016. doi: 10.3847/0004-637X/825/1/41.

E. Vanzella, M. Nonino, G. Cupani, M. Castellano, E. Sani, M. Mignoli, F. Calura, M. Meneghetti, R. Gilli, A. Comastri, A. Mercurio, G. B. Caminha, K. Caputi, P. Rosati, C. Grillo, S. Cristiani, I. Balestra, A. Fontana, and M. Giavalisco. Direct Lyman continuum and Ly α escape observed at redshift 4. , 476:L15–L19, May 2018. doi: 10.1093/mnrasl/sly023.

D. R. Weisz, B. D. Johnson, L. C. Johnson, E. D. Skillman, J. C. Lee, R. C. Kennicutt, D. Calzetti, L. van Zee, M. S. Bothwell, J. J. Dalcanton, D. A. Dale, and B. F. Williams. Modeling the Effects of Star Formation Histories on Hα and Ultraviolet Fluxes in nearby Dwarf Galaxies. , 744:44, January 2012a. doi: 10.1088/0004-637X/744/1/44.

Daniel R. Weisz, Benjamin D. Johnson, L. Clifton Johnson, Evan D. Skillman, Janice C. Lee, Robert C. Kennicutt, Daniela Calzetti, Liese van Zee, Matthew S. Bothwell, Julianne J. Dalcanton, Daniel A. Dale, and Benjamin F. Williams. Modeling the Effects of Star Formation Histories on Hα and Ultraviolet Fluxes in nearby Dwarf Galaxies. , 744:44, January 2012b. doi: 10.1088/0004-637X/744/1/44.

K. E. Whitaker, P. G. van Dokkum, G. Brammer, and M. Franx. The Star Formation Mass Sequence Out to z = 2.5. , 754:L29, August 2012. doi: 10.1088/2041-8205/754/2/L29.

J. H. Wise, V. G. Demchenko, M. T. Halicek, M. L. Norman, M. J. Turk, T. Abel, and B. D. Smith. The birth of a galaxy - III. Propelling reionization with the faintest galaxies. , 442:2560–2579, August 2014. doi: 10.1093/mnras/stu979.

Y. Yoshii and N. Arimoto. Spheroidal systems as a one-parameter family of mass at their birth. , 188:13–23, December 1987.

Q. Zhang and S. M. Fall. The Mass Function of Young Star Clusters in the "Antennae" Galaxies. , 527:L81–L84, December 1999. doi: 10.1086/312412.